Title
Self-consistent Modeling of the Intergalactic Ionizing Radiation Field Across Cosmic Time

Author
Davies, Frederick Byron

Publication Date
2015

Peer reviewed|Thesis/dissertation

University of California
Los Angeles

Self-consistent Modeling of the Intergalactic Ionizing Radiation Field Across Cosmic Time

A dissertation submitted in partial satisfaction
of the requirements for the degree
Doctor of Philosophy in Astronomy

by

Frederick Byron Davies

2015

Abstract of the Dissertation

Self-consistent Modeling of the Intergalactic Ionizing Radiation Field Across Cosmic Time

by

Frederick Byron Davies

Doctor of Philosophy in Astronomy

University of California, Los Angeles, 2015

Professor Steven R. Furlanetto, Chair

Understanding the ionizing radiation field in intergalactic space is crucial for studying the intergalactic medium (IGM). The ionizing background naturally fluctuates in space due to the discrete nature of ionizing sources (i.e. individual galaxies and quasars) and their clustering due to the cosmic growth of structure. These fluctuations are typically ignored in cosmological simulations, but they may be required to explain recent observations of the hydrogen and helium Lyα forests. For my thesis, I have developed novel physically-motivated models of the large-scale fluctuations in the ionizing background and the mean free path of ionizing photons which compare favorably to the latest observations. I have also re-investigated a once promising idea to directly observe the ionization of the IGM by quasars during the epoch of reionization through Lyα emission from the ionization front.

The dissertation of Frederick Byron Davies is approved.

Roberto H. Schonmann

Edward L. Wright

Alice E. Shapley

Steven R. Furlanetto, Committee Chair

University of California, Los Angeles

2015

Table of Contents

List of Figures

List of Tables

Acknowledgments

I would first like to thank my advisor, Steven Furlanetto, for making all of this possible. My experience working with Steve as an undergraduate researcher in the summer of 2009 was critical to my decision to come to UCLA for graduate school, and despite his claims to the contrary, I would not have made it through without his constant guidance and support. I would also like to thank Alice Shapley for believing in me despite my struggles early on in graduate school, Ned Wright for teaching me how to be critical in my interpretation of scientific papers and for being the most regular participant in astro-ph coffee, and Jean Turner for indulging my side interests in radio and sub-millimeter astronomy.

I would like to thank the UCLA Astronomy graduate students for providing constant moral support throughout my time in graduate school; I could not have made it without their help through difficult times. I would especially like to thank Shane Frewen and Nathaniel Ross for acting as my "older brothers" in spirit both academically and socially (for better or worse), and Breann Sitarski for her invaluable support and advice (despite always glaring at me in the hallway).

Finally, I would not be able to finish without thanking my family for their constant support. Without my parents' enthusiasm towards my education starting from an early age, I could not have possibly made it this far. My sister Juliana deserves special thanks for taking the time to visit me several times when I needed help the most.

Vita

2008	NSF REU Researcher, National Radio Astronomy Observatory, Socorro, NM.
2009	NSF REU Researcher, Department of Physics & Astronomy, UCLA, Los Angeles, California.
2010	B.S. in Physics with Astrophysics option, New Mexico Tech, Socorro, NM.
2010–present	Graduate Student Researcher, Department of Physics & Astronomy, UCLA, Los Angeles, California.
2012	M.S. in Astronomy, UCLA, Los Angeles, California.
2013–2014	Teaching Assistant, Department of Physics & Astronomy, UCLA. Taught discussion sections of Astronomy 82 (stellar evolution, galaxies, and cosmology for majors; Spring 2013) and Astronomy 6 (cosmology for non-majors; Winter 2014).

CHAPTER 1

Introduction

The current paradigm of modern cosmology is the Λ cold dark matter (ΛCDM) model. In ΛCDM, the Universe is composed of "normal" matter (primarily baryonic: hydrogen, helium, etc.), collisionless "dark" matter that does not appear to interact with normal matter, and a vacuum energy Λ (the so-called "cosmological constant"). The intergalactic medium (IGM) is the network of sheets and filaments of gas that fills the vast majority of the volume of the Universe, and the evolution of this material across cosmic time reflects the growth of structure on large-scales predicted by ΛCDM. At the present day, the normal matter in the IGM (overwhelmingly hydrogen and helium) is fully ionized, in equilibrium with photoionization by distant sources. However, immediately following the release of the cosmic microwave background (CMB) at the surface of last scattering after the Big Bang, the Universe was almost completely neutral. The subsequent growth of structure and formation of stars, galaxies, and supermassive black holes eventually resulted in the "reionization"[1] of hydrogen and helium in the IGM.

The ionization of hydrogen and the first ionization of helium require photons with at least 13.6 eV and 24.6 eV of energy, respectively. Such photons are produced in large quantities by young massive stars, so the epoch of hydrogen reionization began as soon as the first stars and galaxies formed in the early Universe. Hydrogen reionization is believed to have finished approximately one billion years after the Big Bang (or equivalently, redshift[2] $z \sim 6$),

[1]Before the last scattering of the CMB, the hydrogen and helium in the Universe were highly ionized due to the high density and temperature at very early times soon after the Big Bang. Hence, the later ionization by galaxies and quasars is a "re"-ionization.

[2]The "redshift" z of light emitted by distant objects is defined by a shift in wavelength $1+z = \lambda_{\rm obs}/\lambda_{\rm true}$, and is due to the expansion of the Universe since the time the photon was emitted. It is often used by astronomers as a proxy for time, with higher redshift corresponding to earlier cosmic epochs and $z = 0$ corresponding to the present day.

coincident with the first ionization of helium. The second ionization of helium requires 54.4 eV of energy, and such highly energetic photons are produced only in modest quantities by stars. The epoch of helium reionization had to await the formation of quasars, accretion disks surrounding supermassive black holes, and thus helium remained singly-ionized until the epoch of helium reionization one billion years later ($z \sim 3$).

The epoch of reionization was a critical milestone of early structure formation, representing the point at which the number of high-energy photons emitted by stars in the first galaxies is comparable to the total number of atoms in the Universe. Because reionization involves almost every atom in the Universe during a relatively short[3] period of time, it should in principle be "easy" to observe. Constraints on the progress and topology of reionization are currently the subject of intense observational and theoretical efforts. Promising probes include the measurement of the 21 cm hyperfine structure line of neutral hydrogen from the IGM (e.g. Furlanetto et al. 2006) and evolution in the fraction of galaxies exhibiting bright Lyα emission (e.g. McQuinn et al. 2007a), but observations with current instruments are only modestly constraining and highly model-dependent (e.g. Parsons et al. 2014 and Tilvi et al. 2014, respectively). The ionization process itself greatly heats the IGM, influencing the future accretion of gas (i.e. fuel for star formation) onto galaxies. This radiative feedback is predicted to suppress the formation of stars in small galaxies, an effect which may have been recently detected in the star formation history of satellite galaxies of our own Milky Way galaxy (e.g. Brown et al. 2014). Ionizing photons have continued to be produced since these epochs, leaving the IGM in a highly ionized state.

The most prominent feature of neutral gas is the strong absorption of photons by resonant atomic line transitions – transitions from the ground state $n = 1$ level to higher n states. For hydrogen, these transitions are known as the Lyman series: Lyα , Lyβ, Lyγ, etc. corresponding to $n = 1$–2, $n = 1$–3, $n = 1$–4, etc., respectively[4]. The highly ionized nature of the IGM is well known from studies of the so-called "Lyα forest", the vast number

[3]Current estimates (e.g. Robertson et al. 2015) suggest that the bulk of reionization occurred within a roughly 200 million year period, only $\sim 1/5$th of the age of the Universe at the time it was finished, and only $\sim 1/70$th of its current age.

[4]Singly-ionized helium behaves very similar to atomic hydrogen and has its own "Lyman series" but with four times the energy in each transition.

of absorption lines seen in the spectra of high-redshift quasars (e.g. Rauch 1998). These absorption lines come about due to the resonant absorption of Lyα photons by the residual amount of neutral gas in the IGM – a fully neutral medium would be entirely opaque, with an optical depth greater than 10^5 (i.e. fewer than one in $e^{-100,000}$ photons would pass through unabsorbed) (Gunn & Peterson, 1965). The Lyα forest represents a window into the structure of the IGM, but with an important caveat: interpreting the physical density of a Lyα absorption line requires knowledge of the ionization balance. The ionization state of the IGM is set by the ionizing radiation field from stars and quasars known as the "ionizing background."

The ionizing background is the sum of ionizing radiation from sources, typically parameterized by an emissivity ϵ, filtered by neutral absorbing clouds in the IGM over a characteristic scale λ, the mean free path. The strength of the ionizing background is typically parameterized by two closely related quantities: J_ν, the specific intensity of radiation at frequency ν, and Γ, the total ionization rate due to the entire ionizing spectrum. In general, the ionization rate is related to the emissivity and mean free path by $\Gamma \propto \epsilon\lambda$. Early 1D models for the ionizing background allowed key tests of structure formation in ΛCDM cosmology almost two decades ago (Miralda-Escudé et al., 1996), and similar models (e.g. Faucher-Giguère et al. 2009) are still used today in state-of-the-art cosmological simulations (e.g. Vogelsberger et al. 2014) to provide ionization heating and cooling in the IGM.

The success of 1D ionizing background models is limited, however, to the regime where the mean free path is very large. By coincidence this is indeed the case at $z \sim 2$–5 where the Lyα forest is redshifted to optical wavelengths and can be easily observed by ground-based instruments. If the mean free path is short compared to either the distance between sources, or if the sources are strongly clustered at the mean free path scale, the strength of the ionizing background will vary considerably in space. The former condition is met by the helium-ionizing background at $z \sim 3$, while the latter is met by the hydrogen-ionizing background at $z \sim 6$, both immediately following their respective reionization epochs. Ionizing background fluctuations manifest as variations in transmission through both the hydrogen and helium Lyα forests, which have recently been observed at those epochs. Fluctuations in the ionizing

background may also lead to fluctuations in the mean free path due to the regulation of neutral absorber sizes by the external radiation field. Theoretical modeling of these effects is difficult for several reasons, but the dominant factors are the required dynamic range to both resolve the absorbing clouds which set the mean free path and the considerable computational expense of 3D radiative transfer modeling.

For my thesis, I have developed novel models of the ionizing background that "bridge the gap" between the standard 1D models and expensive radiative transfer models in order to model fluctuations in the ionizing background and, for the first time, the mean free path of ionizing photons. My new models act as extensions to the original 1D models, making many of the same simplifying assumptions but including the effects of realistic source distributions and variations in the mean free path of ionizing photons. I have also re-investigated a potentially promising observational probe of the reionization epoch with a combination of numerical and analytic approaches that improve the predictive power relative to past work.

My thesis is organized as follows. In Chapter 2, I modify the standard 1D cosmological radiative transfer model to include fluctuations in the mean free path of ionizing photons in an attempt to interpret observations of the mean opacity of the helium Lyα forest at $z \sim 2.5$–3 (published in MNRAS, Davies & Furlanetto 2014). In Chapter 3, I extend the fluctuating ionizing background and mean free path model from Chapter 2 to a time-dependent 3D model to make predictions for the evolution of variations in helium Lyα forest opacity on large-scales at $z \sim 2.5$–3.5. In Chapter 4, I construct a similar 3D model of the fluctuating hydrogen-ionizing background for comparison to observations of the hydrogen Lyα forest at $z \sim 5.6$. In Chapter 5, I investigate the Lyα emission from the ionization fronts of luminous quasars during the epoch of reionization (submitted to MNRAS). Finally, in Chapter 6 I conclude with a summary and final discussion of key results.

CHAPTER 2

The effect of fluctuations on the helium-ionizing background

2.1 Introduction

The ionizing background is crucial for understanding many aspects of large-scale structure and galaxy formation at high redshifts. For example, unraveling the physical density structure of the Lyα forest (which contains most of the the intergalactic medium, or IGM, at $z \gtrsim 2$) requires knowledge of the ionization state of the intervening material (Rauch, 1998; Meiksin, 2009). It is also crucial for understanding the abundance and distribution of heavy elements in the IGM, whose ionization states depend sensitively on the local metagalactic radiation field (e.g., Songaila 1998, 2005; Kim et al. 2002b; Aguirre et al. 2004; Bolton & Viel 2011). Additionally, the ionizing background is an important input parameter for cosmological simulations because it regulates the dominant heating and cooling in the IGM (Davé et al., 1999; Springel & Hernquist, 2003), which forms the fuel supply for later galaxy formation. Finally, the ionizing background holds important clues about galaxies and quasars, because they are the dominant sources behind it. Precise measurements can constrain the star formation rate, the escape fraction of ionizing photons from galaxies, and the importance of luminous quasars (Madau et al., 1999; Faucher-Giguère et al., 2008a, 2009; Haardt & Madau, 2012).

Perhaps most importantly, the ionizing background is tied inextricably to the reionization process, when the global ionization state of intergalactic atoms changes rapidly. For example, measurements of the H I ionizing background at $z \sim 5$–6 show that hydrogen reionization appears to proceed relatively slowly (Bolton & Haehnelt, 2007b). Its properties will also be

crucial for understanding He II reionization, which is due to bright quasars (Sokasian et al., 2003; Furlanetto & Oh, 2008a; McQuinn et al., 2009). Based on studies of the effective optical depth of the He II Lyα forest, the reionization of He II in the universe seems to have completed at $z \sim 3$ (Reimers et al., 1997; Kriss et al., 2001; Zheng et al., 2004; Shull et al., 2004). The evolution of the ionizing background during and after He II reionization is critical to interpreting new and upcoming He II Lyα forest results from *HST/COS* (Shull et al., 2010; Worseck et al., 2011; Syphers et al., 2012). Theoretical calculations have attempted to address this evolution by semi-analytic modelling (Dixon & Furlanetto, 2009; Furlanetto & Dixon, 2010) and hydrodynamic simulations of the IGM (Sokasian et al., 2003; Bolton et al., 2006; Paschos et al., 2007; McQuinn et al., 2009).

There is a long history of calculations to estimate the properties of the metagalactic ionizing radiation field. Haardt & Madau (1996) made a landmark study of the ionizing background using a cosmological radiative transfer model for ionizing photons traveling through a clumpy IGM. By combining state-of-the-art constraints on the distribution of ionizing sources and the absorber distribution of the IGM, Haardt & Madau (1996) were able to compute the evolving ionizing background of H I and He II. Further studies (Fardal et al., 1998; Faucher-Giguère et al., 2009; Haardt & Madau, 2012) have updated this framework with new constraints on the population of ionizing sources and the distribution and properties of IGM absorbers. However, all of these studies treated the ionizing background (and its sources and sinks) as *uniform* components, which is a reasonable approximation for the H I background (at least at low and moderate redshifts; Meiksin & White 2004) but is a poor approximation when bright, rare sources dominate the emissivity (as is the case for quasars and the He II ionizing background).

Fardal et al. (1998) showed how the relatively large mean separation of He II ionizing sources could contribute to the significant observed fluctuations in the ionizing background and hence in the observable He II Lyα effective optical depth. An analytic description of variations in the metagalactic radiation field was introduced by Zuo (1992), expanded by Meiksin & White (2003), and later used by Furlanetto (2009) to study fluctuations in the He II ionizing background. Despite this theoretical interest, there has been no effort to include

the effect of these fluctuations on the ionizing continuum opacity within a cosmological radiative transfer model. In this work, we attempt to show the self-consistent effect of these fluctuations on the mean ionizing background.

We begin in Section 2 with a description of our implementation of a cosmological radiative transfer model to calculate self-consistently the He II ionization rate. Then, in Section 3, we present the results of our model. In Section 4, we use the results from that model to calculate the evolution of the He II effective optical depth and compare it to observations. We discuss our model assumptions and compare to previous work in Section 5. We conclude in Section 6.

In our calculations, we assume the following cosmology: $\Omega_m = 0.26$, $\Omega_\Lambda = 0.74$, $\Omega_b = 0.044$, and $h = 0.74$ (Dunkley et al., 2009). All distances are given in comoving units unless otherwise specified.

2.2 Inputs/Methods

2.2.1 Cosmological Radiative Transfer

To calculate the He II ionizing background, we employ a cosmological radiative transfer model (Haardt & Madau, 1996). By considering photon conservation in a comoving volume element, the specific intensity of ionizing radiation J_ν behaves as

$$\left(\frac{\partial}{\partial t} - \nu H \frac{\partial}{\partial \nu}\right) J_\nu = -3HJ_\nu - c\alpha_\nu J_\nu + \frac{c}{4\pi}\epsilon_\nu, \tag{2.1}$$

where $H(t)$ is the Hubble parameter, c is the speed of light, α_ν is the absorption coefficient (with $d\tau_\nu = \alpha_\nu dl$ and dl the proper line element), and ϵ_ν is the proper emissivity. This approach assumes that each volume element can be described as an isotropic source and sink of radiation through ϵ_ν and α_ν, respectively: we will revisit this assumption later on. The solution to the cosmological radiative transfer equation is

$$J_{\nu_0}(z_0) = \frac{1}{4\pi}\int_{z_0}^{\infty} dz \frac{dl}{dz}\frac{(1+z_0)^3}{(1+z)^3}\epsilon_\nu(z)\exp[-\bar{\tau}(\nu_0, z_0, z)]. \tag{2.2}$$

where $dl/dz = c/((1+z)H(z))$ is the proper line element, $\nu = \nu_0(1+z)/(1+z_0)$, and $\bar{\tau}$ is the effective optical depth experienced by a photon at frequency ν_0 and redshift z_0 since its emission at redshift z. $\bar{\tau}$ is calculated using $e^{-\bar{\tau}} = \langle e^{-\tau} \rangle$ averaging over all lines of sight. For Poisson-distributed absorbers with H I column density $N_{\rm H\,I}$ this opacity is (Paresce et al., 1980)

$$\bar{\tau}(\nu_0, z_0, z) = \int_{z_0}^{z} dz' \int_0^{\infty} dN_{\rm H\,I} \frac{\partial^2 N}{\partial N_{\rm H\,I} \partial z'} (1 - e^{-\tau_\nu}), \tag{2.3}$$

where $\partial^2 N/\partial N_{\rm H\,I} \partial z \equiv f(N_{\rm H\,I}, z)$ is the column density distribution function (CDDF) of neutral hydrogen absorbers. The most common simple form of the CDDF is a power law in column density and redshift: $f(N_{\rm H\,I}, z) \propto N_{\rm H\,I}^{-\beta}(1+z)^{\gamma}$, but we will allow more sophisticated models as well (see § 2.2.5.3).

The optical depth of an absorber to ionizing photons of frequency ν is given by

$$\tau_\nu = N_{\rm H\,I}\sigma_{\rm H\,I}(\nu) + N_{\rm He\,I}\sigma_{\rm He\,I}(\nu) + N_{\rm He\,II}\sigma_{\rm He\,II}(\nu), \tag{2.4}$$

where N_i are the column densities and σ_i are the photoionization cross-sections of ion i. Because only the column density distribution of $N_{\rm H\,I}$ has been measured, we use a model for the relationship between $N_{\rm H\,I}$ and $N_{\rm He\,II}$ to calculate the He II ionizing opacity (see § 2.2.1.1). In the frequency range contributing to the He II ionizing background ($\nu > \nu_{\rm He\,II} = 4\,\nu_{\rm H\,I}$) we assume the contribution to the optical depth from He I is negligible following Faucher-Giguère et al. (2009). Finally, the ionization rate for He II is given by

$$\Gamma_{\rm He\,II}(z) = 4\pi \int_{\nu_{\rm He\,II}}^{\infty} \frac{J_\nu(z)}{h\nu} \sigma_{\rm He\,II}(\nu) d\nu, \tag{2.5}$$

where $\nu_{\rm He\,II}$ is the ionization threshold of He II.

In our model, we do not explicitly calculate the H I ionization rate, as that calculation depends strongly on poorly constrained models of the escape fraction of ionizing photons from star-forming galaxies (see e.g. Haardt & Madau 2012). Because the detailed evolution of $\Gamma_{\rm H\,I}$ is not the focus of this work, we instead adopt an empirical estimate of the H I ionization rate from measurements of the Lyα forest (Faucher-Giguère et al., 2008a), which appears to be fairly constant over our redshift range of interest ($z \sim 2$–4). We have ensured that our fiducial value for $\Gamma_{\rm H\,I}$ is consistent with our fiducial quasar emissivity and CDDF;

that is, the value of $\Gamma_{\rm H\,I}$ calculated in our fiducial model with quasars only is less than the value we assume in the fiducial $\Gamma_{\rm He\,II}$ calculation.

Because the ionizing background and the continuum opacity are interrelated through the conversion of $N_{\rm H\,I}$ to $N_{\rm He\,II}$ described in the next section, the procedure must be iterated over the entire redshift range until convergence. The result of this cosmological radiative transfer model as presented in this section will be referred to as the "uniform" background model in the rest of the paper.

2.2.1.1 Absorber Ionization Structure: $\mathbf{N_{H\,I}}$ to $\mathbf{N_{He\,II}}$

The relationship between $N_{\rm H\,I}$ and $N_{\rm He\,II}$ is usually parameterized by the quantity $\eta = N_{\rm He\,II}/N_{\rm H\,I}$ (Miralda-Escude, 1993). In the optically thin case, η is given by

$$\eta_{\rm thin} = \frac{\Gamma_{\rm H\,I}}{\Gamma_{\rm He\,II}} \frac{\alpha^A_{\rm He\,II}}{\alpha^A_{\rm H\,I}} \frac{Y}{4X}, \tag{2.6}$$

where $\alpha^A_{\rm H\,I}$ and $\alpha^A_{\rm He\,II}$ are the case-A recombination coefficients of H I and He II, and $X = 0.75$ and $Y = 0.25$ are the hydrogen and helium mass fractions, respectively. In an optically thin environment, photons produced by recombinations to the ground state of He II will escape from the local medium, hence our choice of case-A recombination coefficients. Note, however, that these coefficients enter only in the ratio, so this choice does not have any significant effect.

To more generally translate H I column densities into He II, we adopt a fit to numerical simulations that accounts for self-shielding in neutral hydrogen systems (Fardal et al., 1998; Faucher-Giguère et al., 2009),

$$\frac{Y}{16X} \frac{\tau_{\rm H\,I}}{1 + A\tau_{\rm H\,I}} I_{\rm H\,I} = \tau_{\rm He\,II} + \frac{\tau_{\rm He\,II}}{1 + B\tau_{\rm He\,II}} I_{\rm He\,II}, \tag{2.7}$$

where $\tau_i = \sigma_i N_i$, $A = 0.15$ and $B = 0.2$ are fitting coefficients used by Faucher-Giguère et al. (2009), and $I_i = \Gamma_i / n_e \alpha^A_i$ with $n_e = 1.4 \times 10^{-3}$ cm^{-3}($N_{\rm H\,I}/10^{17.2}$ cm^{-2})$^{2/3}$($\Gamma_{\rm H\,I}/10^{-12}$ s^{-1})$^{2/3}$ (Schaye, 2001). At small H I column densities ($N_{\rm H\,I} \lesssim 10^{15}$ cm^{-2}), $N_{\rm He\,II} = \eta_{\rm thin} N_{\rm H\,I}$ as expected. He II becomes optically thick to ionizing radiation for larger column densities ($N_{\rm H\,I} \sim 10^{15}$–$10^{17}$ cm^{-2}), so η increases by a factor of a few as more He II forms while

hydrogen remains highly ionized. Then, for $N_{\rm H\,I} \gtrsim 10^{17}$ cm^{-2}, η steeply drops as the systems become optically thick to H I ionizing photons.

For systems with $N_{\rm H\,I} > 10^{18}$ cm^{-2}, the numerical fit systematically under-predicts the amount of He II from the original model (see Figure 1 of Faucher-Giguère et al. 2009). For frequencies near $\nu_{\rm He\,II}$, the opacity is unaffected because these high $N_{\rm H\,I}$ systems are still optically thick due to H I absorption. However, for $\nu \gtrsim 2.5\,\nu_{\rm He\,II}$, absorbers with $N_{\rm H\,I} \sim 10^{19}$–$10^{20}$ cm^{-2} start to become optically thin due to their relative lack of He II. Fortunately, the total ionization rate only changes slightly because the range of affected column densities is small and the vast majority of ionizations occur at lower frequencies ($\sigma_{\rm He\,II} \propto \nu^{-3}$).

Haardt & Madau (2012) applied a similar method to fit the absorber structure that considers the average Γ within absorbers instead of the external "optically-thin" Γ. While their method provides a better fit to the numerical models at $N_{\rm H\,I} > 10^{18}$ cm^{-2}, it differs from the Faucher-Giguère et al. (2009) model only in the details for the more important $\tau_{\rm He\,II} \sim 1$ ($N_{\rm H\,I} \sim 10^{16}$ cm^{-2}) absorbers. This is an example of one of the systematic uncertainties in our procedure: these models for η must assume physical characteristics for the absorbers (densities, temperatures, and geometry, for example) that are both uncertain and simplifications of the true IGM physics. For concreteness, the numerical absorber model from Faucher-Giguère et al. (2009) assumes uniform density semi-infinite slabs with a thickness determined by the local Jeans length (at $T = 20,000$ K) in photoionization equilibrium with both an external radiation background and internal recombination processes.

2.2.1.2 Recombination Emissivity

Recombinations of He III to the ground state of He II will produce ionizing continuum radiation. Although the recombination rate in a uniform density medium can easily be estimated from ionization equilibrium, the real universe requires a more detailed approach for two reasons. First, density inhomogeneities in the IGM substantially boost the recombination rate. We can model this by integrating over the H I column density distribution of the Lyα forest. Second, recombination photons produced inside optically thick absorbers will not

escape to affect the IGM.

We model the recombination emissivity of IGM absorbers with a numerical fit to the radiative transfer models of Faucher-Giguère et al. (2009). The emergent specific intensity from an absorber with He II column density $N_{\rm He\,II}$ can be approximated by

$$\begin{aligned} I_\nu^{\rm rec}(N_{\rm He\,II}) &= \frac{h\nu}{4\pi}\left(1-\frac{\alpha^B_{\rm He\,II}}{\alpha^A_{\rm He\,II}}\right)\Gamma_{\rm He\,II}\phi_{\nu,\rm rec} \\ &\quad \times N_T\left(1-e^{N_{\rm He\,II}/N_T}\right), \end{aligned} \tag{2.8}$$

where the second factor is the fraction of ionizations to the ground state and the local ionization rate is $\Gamma_{\rm He\,II}$. $N_T = 10^{17.3}$ cm^{-2} is the approximate threshold He II column density above which the emission becomes saturated by absorption within the absorber itself (the decline at larger columns is approximated by the last factor). $\phi_{\nu,\rm rec}$ is the normalized recombination emission profile:

$$\phi_{\nu,\rm rec} \propto \nu^{-1} e^{-h\nu/k_B T}\theta(\nu-\nu_{\rm He\,II}), \tag{2.9}$$

where $\theta(x)$ is the Heaviside step function. The effective frequency width of this emission is $\Delta\nu/\nu \sim k_B T/h\nu_{\rm He\,II} \sim 0.03$, which limits the distance these photons can travel to $\lesssim 30$ Mpc before redshifting below the He II ionizing edge.

The total proper emissivity from recombinations is then

$$\epsilon_{\nu,\rm rec}(z) = \frac{dz}{dl}\int_0^\infty dN_{\rm H\,I}\, f(N_{\rm H\,I}, z)\, 4\pi I_\nu^{\rm rec}(N_{\rm He\,II}), \tag{2.10}$$

where the intensity depends implicitly on $N_{\rm H\,I}$ through the conversion factor η. We include the recombination emissivity in the cosmological radiative transfer calculation by simply adding it to the emissivity from quasars, ignoring the difference in spatial distribution.

We note here that the recombination photons can have a much larger effect on the ionizing background than one might naively expect from their emissivity. As we shall see later, increasing the emissivity also increases the mean free path of ionizing photons, which amplifies the effect of the additional ionizing photons. We will explore this issue further in § 2.3.1.5.

2.2.2 Mean Free Path

The opacity per unit redshift, $d\bar{\tau}/dz$, was integrated in equation (2.3) to calculate the total opacity between two redshifts:

$$\frac{d\bar{\tau}}{dz} = \int_0^\infty dN_{\rm H\,I} f(N_{\rm H\,I}, z)(1 - e^{-\tau_\nu(\Gamma_{\rm He\,II})}), \tag{2.11}$$

where the absorber opacity as a function of $N_{\rm H\,I}$, τ_ν, depends on $\Gamma_{\rm He\,II}$ through the absorber model in Section 2.2.1.1. At a given redshift, $d\bar{\tau}/dz$ describes the local opacity due to the forest of individual absorbers in the IGM. By inverting this quantity and converting from redshift difference to a comoving distance, we find the distance per unit optical depth, which is simply the mean free path:

$$\lambda_{\rm mfp}(\nu, z) = \frac{dl}{dz}\left(\frac{d\bar{\tau}}{dz}\right)^{-1}. \tag{2.12}$$

If $f(N_i, z) = N_0 N_i^{-\beta}(1+z)^\gamma$ and $\sigma_i = \sigma_0(\nu/\nu_i)^{-3}$, the comoving mean free path reduces to

$$\begin{aligned}\lambda_{\rm mfp}(\nu, z) \;\approx\; & \frac{(\beta-1)c}{\Gamma_G(2-\beta)N_0\sigma_0^{\beta-1}}\left(\frac{\nu}{\nu_i}\right)^{3(\beta-1)} \\ & \times\frac{1}{(1+z)^\gamma H(z)},\end{aligned} \tag{2.13}$$

where Γ_G is the Gamma function. The redshift dependence of the mean free path in this simplified model is then $\lambda_{\rm mfp} \propto (1+z)^{-(\gamma+1.5)}$. This power law dependence is a good approximation to describe the evolution of the mean free path of H I ionizing photons ($\lambda_{\rm H\,I}$) in our model because the H I CDDF is fixed, but we find that it fails to capture the more complicated $\Gamma_{\rm He\,II}$-dependent evolution of the mean free path of He II ionizing photons ($\lambda_{\rm He\,II}$; see § 2.3.1.4).

Recent efforts by Prochaska et al. (2009) and O'Meara et al. (2013) have directly measured the H I ionizing mean free path of the IGM near $z \sim 4$ and $z \sim 2$ respectively. For an identical distribution of absorbers, they would report different values than obtained by our approach because they define the mean free path as the distance traveled by a photon through the *evolving* IGM while it redshifts with the cosmic expansion, rather than the path that could be traveled if the IGM and photon retained their original properties (as is the usual definition for theoretical work). We follow the latter definition here.

2.2.3 Fluctuations

In a smooth, fully-ionized IGM, the intensity of ionizing radiation from an individual quasar falls as $\exp[-r/\lambda_{\rm mfp}]/r^2$. Given a distribution of quasar luminosities and a mean free path, a probability distribution of intensities can be computed assuming random placement of quasars following Poisson statistics (Zuo, 1992; Meiksin & White, 2003). The effects of this distribution on the *mean* ionizing background have not previously been considered. The next stage in our model is therefore to incorporate the distribution (in a somewhat ad hoc manner) in order to understand better the implications of this fluctuating background.

We use the Hopkins et al. (2007) B-band quasar luminosity function (QLF) to describe the distribution of relative quasar luminosities, assuming an average quasar spectral energy distribution such that the specific luminosity at the H I ionizing edge is proportional to the B-band specific luminosity (L_B), then extrapolating to the He II ionizing edge by a spectral index α. Additionally, while the effect is relatively minor (Furlanetto, 2009), we convolve the quasar luminosity function with a distribution of far-ultraviolet spectral indices that roughly matches observations by Telfer et al. (2002): a Gaussian distribution over $0.5 < \alpha < 3.5$ with central value $\bar{\alpha} = 1.5$ and $\sigma_\alpha = 0.7$. Note that the asymmetric bounds on α lead to an average spectral index of $\alpha \simeq 1.6$ consistent with our fiducial value (described later in § 2.2.5.1). In detail, the average ratio between the emissivity at 1 and 4 Ryd will be somewhat higher than the ratio for a $\alpha = 1.6$ spectrum, but we fold this uncertainty into the ionizing background normalization uncertainty described in § 2.3.

We use the method of characteristic functions from Meiksin & White (2003) to determine the probability distribution of intensity, $f(J)$, then scale linearly to Γ by $\Gamma = J \times \langle\Gamma\rangle/\langle J\rangle$ (Furlanetto, 2009). The last assumption of proportionality between the intensity of radiation and the ionization rate is not strictly true; the intensity at higher frequencies should be more uniform because the mean free path is much larger, although the effect is modest in practice (Dixon et al., 2014). In our calculation of $f(\Gamma)$ we use the mean free path of the "average" He II ionizing photon, $\bar{\lambda}_{\rm HeII} = \lambda_{\rm mfp}(\bar{\nu})$, where $\bar{\nu}$ is defined by

$$\bar{\nu}\Gamma_{\rm He\,II} = 4\pi \int_{\nu_{\rm He\,II}}^{\infty} \nu \times \frac{J_\nu(z)}{h\nu}\sigma_{\rm He\,II}(\nu)d\nu, \tag{2.14}$$

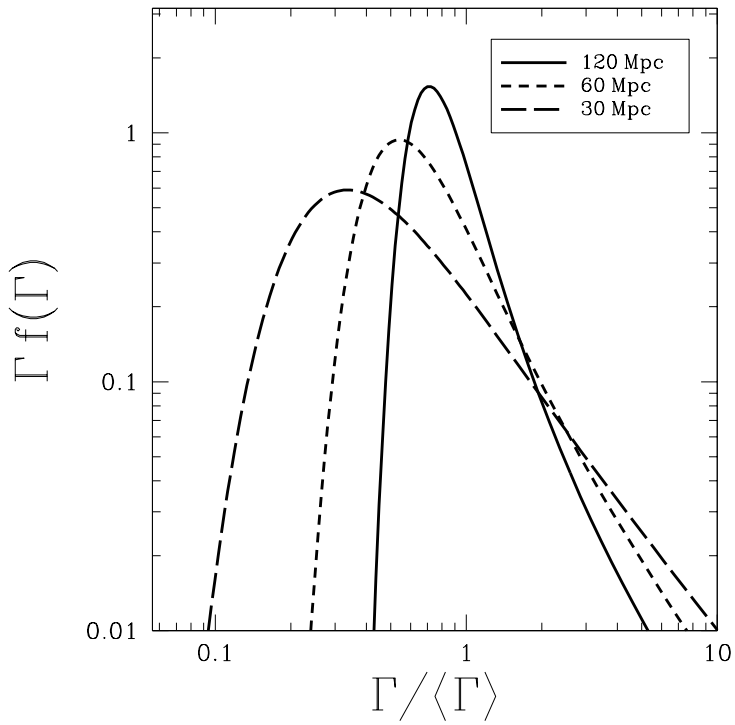

Figure 2.1: Distribution of ionization rates at $z = 3.0$ for $\lambda_{\rm mfp} = 30, 60, 120$ Mpc (long-dashed, dashed, and solid, respectively).

in an attempt to average over the frequency dependence of the background fluctuations. In general, $\bar{\lambda}_{\rm He\,II}$ is substantially larger than $\lambda_{\rm He\,II}$, so our approach provides a conservative estimate when used to calculate the amplitude of ionizing background fluctuations.

Figure 2.1 shows how the $f(\Gamma)$ distribution varies with mean free path. When the mean free path decreases, the peak of the distribution skews towards smaller Γ relative to the mean. For Γ below the mean, we find that the He II opacity of each absorber will increase, with the total opacity increasing as, roughly, $d\bar{\tau}/dz \propto \Gamma^{-2/3}$ using the He II absorber model of Section 2.2.1.1. Because this relationship between the ionization rate and opacity is more gentle than linear, the skewness of the $f(\Gamma)$ distribution results in an average opacity that is *higher* than the opacity at the mean Γ. That is, the lower opacity in rare high Γ regions does not counteract the higher opacity in common low Γ regions. We explore this effect in the following discussion.

We incorporate these fluctuations into our ionizing background model by averaging the opacity $d\bar{\tau}/dz$ (equations 2.3, 2.11) over the distribution $f(\Gamma)$:

$$\left\langle \frac{d\bar{\tau}}{dz} \right\rangle = \int_0^\infty \frac{d\bar{\tau}}{dz}(\Gamma) f(\Gamma) d\Gamma, \tag{2.15}$$

where $d\bar{\tau}/dz$ depends on Γ through the absorber prescription in Section 2.2.1.1 and $f(\Gamma)$ is initialized with the mean free path calculated in the uniform model. This process is repeated using the same $f(\Gamma)$ for each frequency in equations (2.2) and (2.5) to modify the ionizing continuum opacity at each redshift. The fractional increase in the opacity due to the integral over $f(\Gamma)$ is larger for smaller $\lambda_{\rm mfp}$, reaching $\sim 40\%$ in our fiducial model if $\lambda_{\rm mfp}$ is equal to the average distance between bright sources at $z = 3$ (~ 45 Mpc; see §2.3.2). Because the modified opacity leads to new values for $\Gamma_{\rm He\,II}(z)$ and $\lambda_{\rm mfp}(z)$, we iterate this process using the new $\lambda_{\rm mfp}(z)$ to generate $f(\Gamma)$ and using the new $\Gamma_{\rm He\,II}(z)$ to calculate $d\bar{\tau}/dz(\Gamma, z)$.

Unfortunately, as presented above, the $\Gamma_{\rm He\,II}$ calculation does not converge to a non-zero value; the added opacity from the $f(\Gamma)$ prescription causes the iterative procedure to drive $\Gamma_{\rm He\,II}$ down to zero. At relatively high redshifts ($z \gtrsim 3.5$) the mean free path is short enough ($\lambda_{\rm mfp} \lesssim 50$ Mpc) that integrating over $f(\Gamma)$ greatly increases the opacity. In practice, this increased opacity at high redshift propagates small values of $\Gamma_{\rm He\,II}$ to lower redshifts, and the iterative effect pulls Γ down to zero at *all* redshifts. Even when the ionizing background is calculated assuming local emission and absorption of photons (i.e. without an integral over redshift as in equation 2.2) via the absorption-limited approximation $J_\nu(z) = \epsilon_\nu(z)\lambda_{\rm mfp}(\nu, z)/(4\pi)$ (Meiksin & White, 2003), the divergence to zero remains at $z \gtrsim 3.2$.

The reason our procedure breaks down is actually obvious: our cosmological radiative transfer model assumes that ionizing photons are emitted uniformly throughout the universe (with a constant ϵ_ν in equation 2.1), but the real quasar sources are of course point-like. Since the ionizing background near a source is much stronger than the average, the local IGM will be less opaque to ionizing photons, and the quasar photons will penetrate farther into the IGM – increasing the ionizing background. Additionally, our model assumes that the path traversed by an ionizing photon fully samples the distribution of ionization rates

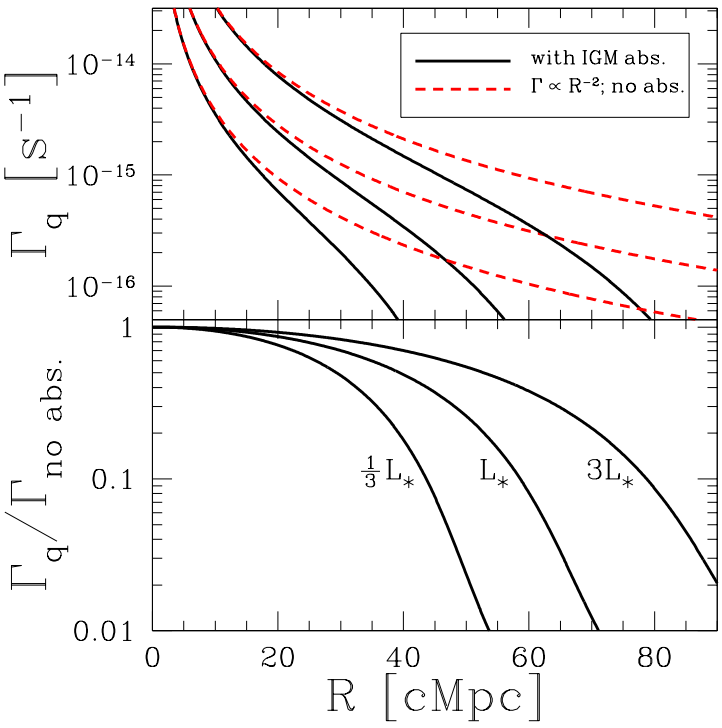

Figure 2.2: Line-of-sight equilibrium ionization rate profile for $L = 1/3\ L_*, L_*, 3L_*$ (from bottom to top) quasars at $z = 3$ with IGM continuum absorption (solid black) and without (dashed red). In all cases, the quasars are assumed to be isolated (i.e., with no contribution from a metagalactic background).

given by $f(\Gamma)$, but within a quasar proximity region this is not accurate, as the radiation profile is smoothly decreasing. To quantify the minimum effect these transparent proximity regions must have on the mean background, we consider a simple model where the ionizing background is calculated as the sum of isolated source ionization rate profiles.[1]

2.2.4 Minimum Background Model

In the absence of an external ionizing background and ignoring the cosmological redshift of ionizing photons, the equilibrium ionization rate profile along a sightline from a single

[1]For simplicity, we will ignore the finite lifetimes of quasars in our calculation. In reality, these finite lifetimes limit the extent of an individual quasar's radiation field. However, the radiation field will continue to propagate outward even after the quasar shuts off, following the profile that we describe here. The statistical results we describe here are therefore unaffected by a finite lifetime.

quasar, $\Gamma_q(R)$, is given by

$$\Gamma_q(R) = \int_{\nu_{\rm He\,II}}^{\infty} \frac{L_\nu}{4\pi R^2 h\nu} \sigma_\nu \exp[-\tau_\nu(R)] d\nu, \tag{2.16}$$

where $\tau_\nu(R)$ is the optical depth at frequency ν from the IGM at $r < R$,

$$\tau_\nu(R) = \int_0^R \frac{d\tau}{dz}(\nu, \Gamma_q(r))(\frac{dl}{dz})^{-1} dr, \tag{2.17}$$

and assuming $L_\nu \propto \nu^{-1.6}$ as the mean quasar spectrum for simplicity.

Figure 2.2 shows the ionization rate profiles for $L = 1/3\ L_*, L_*, 3L_*$ quasars (from bottom to top) at $z = 3$. At small radii, the effective mean free path is very large, so $\Gamma_q \sim R^{-2}$. However, once Γ_q is small enough such that $R \sim \lambda_{\rm mfp}(\Gamma_q)$, the ionization rate drops sharply. Thus, each quasar has a characteristic radius beyond which it generates very few ionizations, effectively a recombination-limited "proximity zone."

This ionization rate profile, integrated from small to large radius, can be calculated without detailed radiative transfer because all of the ionization state and absorption properties are contained in our prescription for the clumpy IGM through the CDDF and absorber structure from Section 2.2.1.1. In a physical sightline, the attenuation in the IGM will be dominated by random encounters with absorbing clouds, so a more accurate description could be obtained by radiative transfer through a realistic IGM density field. We assume ionization equilibrium in the average IGM for simplicity.

The sum of these isolated quasar profiles should provide a *minimal* estimate of the mean background consistent with the CDDF and the QLF, because they ignore collective effects from the overlap of the proximity zones. Armed with the Γ_q profiles as a function of quasar luminosity, we can calculate this minimum mean background by integrating over the QLF and averaging over position,

$$\Gamma_{\rm min} = \int_0^\infty \left(\int_{L_{\rm min}}^\infty \Gamma_q(R, L) \Phi(L) dL \right) 4\pi R^2 dR, \tag{2.18}$$

where $\Phi(L)$ is the Hopkins et al. (2007) QLF and $L_{\rm min}$ is the smallest luminosity quasar that we consider ($L_{\rm min} = 10^{43}$erg s^{-1} in the B-band, but the overall results do not depend strongly on this choice). The majority of $\Gamma_{\rm min}$ comes from cosmologically local sources

(within $\sim$ 75 cMpc), so neglecting the cosmological redshift of ionizing photons should be a reasonable approximation. The resulting $\Gamma_{\rm min}(z)$ will be referred to as the "minimum" background model in the rest of the paper. We will see in Section 2.3 that the minimum model ionization rate is nearly constant over the redshift range we consider.

In our model, the minimum background provides a maximum average opacity for the IGM. To implement the minimum background into our modified cosmological radiative transfer model, we make the following approximation: when determining the opacity $d\tau/dz$ at a given redshift, use the larger of $\Gamma_{\rm He\,II}(z)$ and $\Gamma_{\rm min}(z)$.[2] The minimum background model is not meant to represent a universe where there is a floor in the ionizing background at any point in space, but rather one where the *average* ionizing background has a floor based on the proximity effects of rare bright sources. This model could be similar to the pre-reionization universe, where the average ionizing background is dominated by expanding ionized bubbles around such sources. While the difference between this highly fluctuating (by construction) background and the pre-reionization universe is subtle, in practice we find that distinction does not matter for our purposes. In the regime where the minimum background model dominates our results, the behaviour of the ionizing background is unlikely to be well-described by globally averaged quantities, so we focus our analysis at redshifts when $\Gamma > \Gamma_{\rm min}$.

The results of this modified cosmological radiative transfer model will be referred to as the "fluctuating" background model in the rest of the paper.

2.2.4.1 Summary of Fluctuating Method

In summary, we calculate the fluctuating background model in the following manner:

1. Initialize $\Gamma_{\rm He\,II}(z)$ and $\lambda_{\rm mfp}(z)$ using the standard cosmological radiative transfer approach (equations 2.2–2.5, 2.11–2.12).

2. Calculate $f(\Gamma)$ as a function of redshift using $\lambda_{\rm mfp}(z)$ as input to the method of Furlan-

[2]This discontinuity in the opacity calculation results in a slight redshift discontinuity in the ionizing background evolution, but as mentioned in the text, the mean background we calculate in this regime is unlikely to be physically relevant.

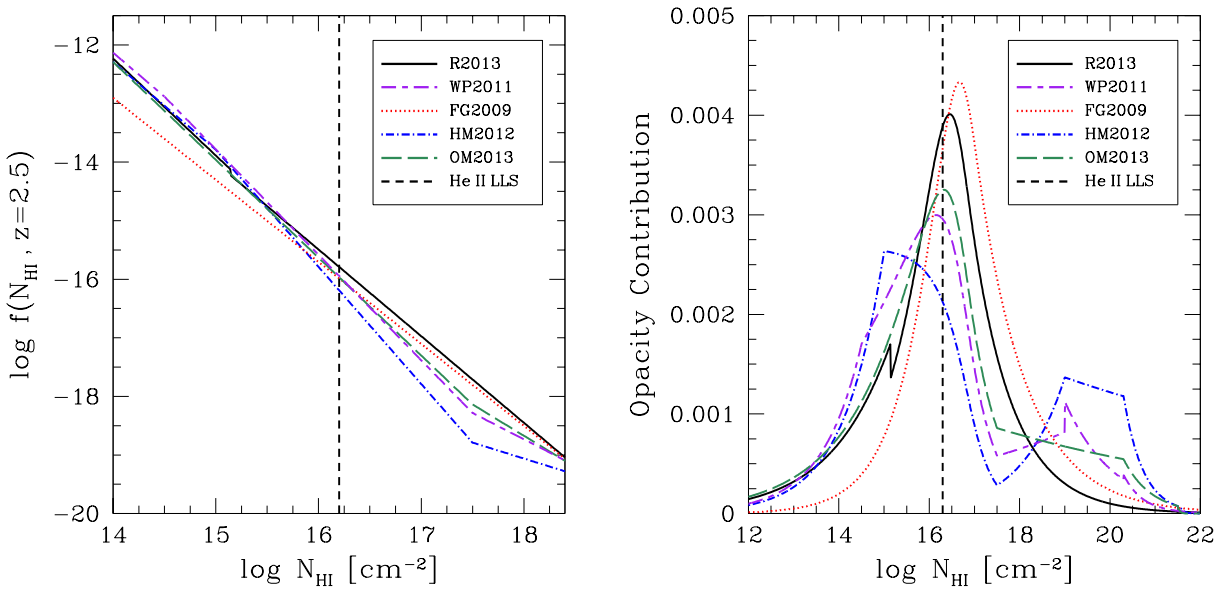

Figure 2.3: Left: Column density distribution functions $f(N_{\rm H\,I}, z = 2.5)$ considered in the text: Rudie et al. (2013) (solid black), Haardt & Madau (2012) (dot-dashed blue), Faucher-Giguère et al. (2009) (dotted red), O'Meara et al. (2013) (long-dashed green), Worseck & Prochaska (2011) (short-dashed-long-dashed purple), focusing on $N_{\rm H\,I}$ that correspond to the most important He II absorbers. The vertical dashed line shows the $N_{\rm H\,I}$ corresponding to a He II "LLS". Right: Relative contribution to the continuum opacity at $\nu_{\rm He\,II}$ per $\log(N_{\rm H\,I})$.

etto (2009).

3. Calculate the average opacity $\langle d\bar{\tau}/dz \rangle$ as a function of redshift using $f(\Gamma)$ (equation 2.15).

4. Calculate $\Gamma_{\rm He\,II}(z)$ with equations 2.2–2.5 using $\langle d\bar{\tau}/dz \rangle$ in equation 2.3.

5. Calculate $\lambda_{\rm mfp}(z)$ with equations 2.11–2.12, substituting $\langle d\bar{\tau}/dz \rangle$ for $d\bar{\tau}/dz$ in equation 2.12.

6. Repeat steps (ii)–(v) until $\Gamma_{\rm He\,II}(z)$ converges.

2.2.5 Model Input Parameters

Other than our simple model assumptions, the largest sources of uncertainty in our analysis are three observed parameters: the He II ionizing emissivity, ϵ_ν, the H I ionization rate, $\Gamma_{\rm H\,I}$, and the neutral hydrogen column density distribution, $f(N_{\rm H\,I}, z)$. In this section, we discuss the range of observed values for these parameters.

2.2.5.1 He II Ionizing Emissivity

We adopt the Lyman limit quasar ionizing emissivity from Haardt & Madau (2012),

$$\begin{aligned} \epsilon_{912}(z) &= 10^{24.6} \mathrm{erg\,s^{-1}\,Mpc^{-3}\,Hz^{-1}} \\ &\quad \times (1+z)^{4.68} \frac{\exp[-0.28z]}{\exp[1.77z] + 26.3}, \end{aligned} \tag{2.19}$$

which is a fit to the integrated B-band quasar luminosity function of Hopkins et al. (2007) converted to $\nu_{\rm H\,I}$ by a constant factor,

$$L_{\nu_{\rm H\,I}} = L_B \times 10^{18.15} \mathrm{erg\,s^{-1}\,Hz^{-1}} \left(\frac{L_\odot}{L_B} \right). \tag{2.20}$$

This factor is effectively an estimate of the average quasar spectrum between ν_B and $\nu_{\rm H\,I}$. For frequencies above the Lyman limit, we assume a power law spectrum with $\epsilon_\nu \propto \nu^{-\alpha}$. For reference, the integrated quasar emissivity given by equation (2.19) increases by $\sim 30\%$ from $z = 3$–2.

The uncertainty in the He II ionizing emissivity is a combination of the uncertainty in the Hopkins et al. (2007) quasar luminosity function and the assumed average quasar spectrum. The former is likely to be small, because the integrated quasar B-band emissivity at $z \gtrsim 2$ comes predominantly from the brightest, and therefore best measured, sources (Hopkins et al., 2007). The latter uncertainty is dominated by the choice of far-UV spectral index α. Telfer et al. (2002) find $\alpha = 1.57 \pm 0.17$ for a composite spectrum of 77 radio-quiet quasars, while the composite including an additional 107 radio-loud quasars has $\alpha = 1.76 \pm 0.12$. In contrast, Scott et al. (2004) found that the average spectral index for their sample of 85 sources was considerably harder, $\alpha = 0.56^{+0.28}_{-0.38}$. Shull et al. (2012) measured a best-fit spectral index of $\alpha = 1.41 \pm 0.21$ for their sample of 22 sources using *HST/COS*.

We adopt $\alpha = 1.6$ as our fiducial value. Note that, because the He II Lyman limit $\nu_{\rm He\,II} = 4\nu_{\rm H\,I}$, a change in the spectral index $\Delta\alpha$ corresponds to a factor of $4^{-\Delta\alpha}$ difference in the emissivity at $\nu_{\rm He\,II}$.

2.2.5.2 H I Ionization Rate

The absorber model in § 2.2.1.1 depends on the H I ionization rate, $\Gamma_{\rm H\,I}$. Measurements of $\Gamma_{\rm H\,I}$ from $z \sim$ 2–3 yield values $\sim 0.5 - 1.0 \times 10^{-12}$ s^{-1} from flux decrement observations (Rauch et al., 1997; Bolton et al., 2005; McDonald & Miralda-Escudé, 2001; Faucher-Giguère et al., 2008a) or $\sim 1.0 - 3.0 \times 10^{-12}$ s^{-1} from proximity effect measurements (Scott et al., 2000). The most recent cosmological radiative transfer model by Haardt & Madau (2012) suggests $\Gamma_{\rm H\,I} \sim 0.8 - 0.9 \times 10^{-12}$ s^{-1}, but as discussed in the next section, that study may have significantly underestimated the total H I opacity of the IGM. We adopt $\Gamma_{\rm H\,I} = 0.6 \times 10^{-12}$ s^{-1}, a value consistent with the measurements of Faucher-Giguère et al. (2008a), as our fiducial value but consider a range of plausible values.

2.2.5.3 Column Density Distribution

The column density distribution of neutral hydrogen $f(N_{\rm H\,I}, z) = \partial^2 N / \partial N_{\rm H\,I} \partial z$ has been measured several times and over a range of redshifts through observations of the H I Lyα

forest. Early observations indicated that the $N_{\rm H\,I}$ distribution is well-fit by a power law of the form $f(N_{\rm H\,I}) \propto N_{\rm H\,I}^{-\beta}$ with $\beta \sim 1.5$ over a wide range of observed column densities ($10^{12} < N_{\rm H\,I} < 10^{22}$ cm^{-2}) and redshifts ($z \sim 0.2$–3.5) (Tytler, 1987). Recent studies of H I ionizing continuum opacity in stacked quasar spectra at $z \sim 2$ and $z \sim 4$ suggest a deficit of Lyman limit systems ($10^{17.2} < N_{\rm H\,I} < 10^{19}$ cm^{-2}; LLS) and intermediate H I column density systems ($10^{15} < N_{\rm H\,I} < 10^{17.2}$ cm^{-2}) relative to the canonical single power law model, and several authors have proposed multi-step power law distributions to describe this feature (Prochaska et al., 2009, 2010; Worseck & Prochaska, 2011; O'Meara et al., 2013; Haardt & Madau, 2012). Rudie et al. (2013) performed the largest survey of $10^{12} < N_{\rm H\,I} < 10^{17.2}$ cm^{-2} systems to date for redshifts $z = 2.02$–2.84 ($\langle z \rangle \sim 2.4$) and found no evidence of the deficit suggested by stacked quasar spectra studies. They found that their measured distribution is well-parameterized by a relatively steep $\beta \sim 1.66$ power law for $N_{\rm H\,I} \lesssim 10^{15}$ cm^{-2} and a $\beta \sim 1.48$ power law for larger H I column densities. The left panel of Figure 2.3 shows several of these distributions graphically.

The redshift evolution of the CDDF is usually parameterized by a power law $f(N_{\rm H\,I}, z) \propto (1+z)^{\gamma}$. However, observationally this γ appears to depend on $N_{\rm H\,I}$, implying that the shape of the CDDF evolves with time. The observational constraints on γ for $z \gtrsim 2$ in the Lyα forest regime ($N_{\rm H\,I} < 10^{17.2}$ cm^{-2}) are $\gamma \sim 2.0$–3.0 from line-counting (Kim et al., 2002a) and measurements of the effective optical depth (Faucher-Giguère et al., 2008b; Dall'Aglio et al., 2008). The number densities of super-Lyman limit (10^{19} cm $^{-2} < N_{\rm H\,I} < 10^{20.3}$ cm $^{-2}$) and damped Lyα ($N_{\rm H\,I} > 10^{20.3}$ cm $^{-2}$) absorbers appear to evolve more slowly with $\gamma \sim 1.7$ (O'Meara et al., 2007; Worseck & Prochaska, 2011) and ~ 1.27 (Rao et al., 2006), respectively. Rudie et al. (2013) found that their data were consistent with $\gamma = 2.5$ and 1.0 for $N_{\rm H\,I}$ below and above $\sim 10^{15}$ cm^{-2}, respectively.

Worseck & Prochaska (2011) and Haardt & Madau (2012) compiled these observations (with the exception of Rudie et al. 2013) and constructed similar multi-step power law CDDFs. The primary difference between the two is the enhanced redshift evolution ($\gamma = 3.0$) of Lyα forest absorbers in the Haardt & Madau (2012) model compared to the Worseck & Prochaska (2011) model ($\gamma = 2.04$). Both models determine the redshift evolution of the

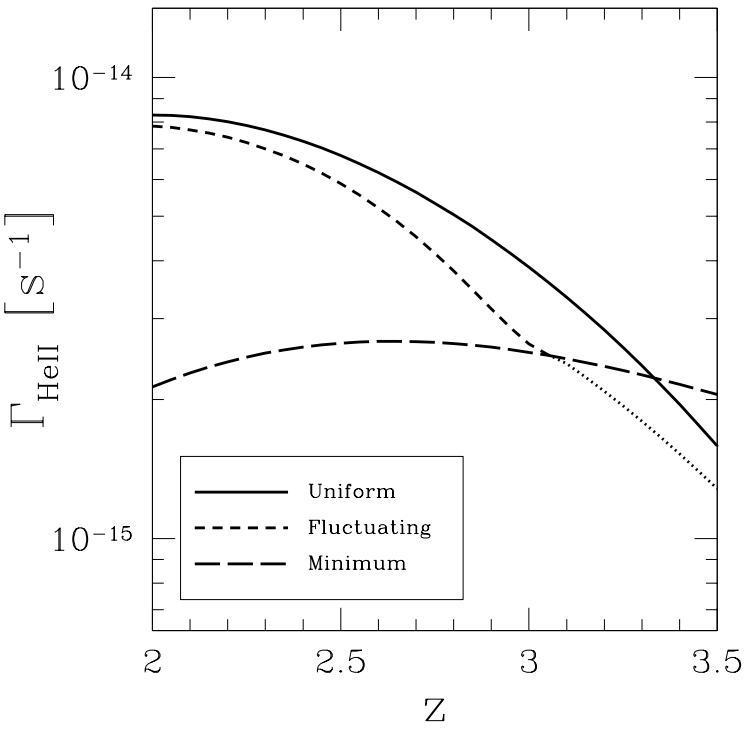

Figure 2.4: Uniform and fluctuating $\Gamma_{\rm He\,II}$ in the fiducial model (solid and dashed curves, respectively) and the "minimum" average ionization rate from isolated quasar profiles (long-dashed). The dotted curve represents the result of the fluctuating model calculation when it is inconsistent (i.e. below) the minimum background model from §2.2.4.

CDDF by comparing to observations of the evolution of the H I Lyα effective optical depth, which is proportional to $(1+z)^{\gamma+1}$. However, Haardt & Madau (2012) calibrate to the measurements of Faucher-Giguère et al. (2008b), while Worseck & Prochaska (2011) chose the measurements of Dall'Aglio et al. (2008). It is unclear why such a difference exists in the effective optical depth evolution measured by these two groups, but it does not significantly affect our results.

In the following sections, we use the broken power-law CDDF from Rudie et al. (2013) as our fiducial model. Their model represents the first solid measurement of intermediate H I column density absorbers that are critical to the He II ionizing opacity, and is consistent with measurements of the H I Lyα effective optical depth (G. Rudie, priv. comm.). However, as the following sections will show, our choice of CDDF does not have significant implications for our final results, given the overall uncertainty in the amplitude of the ionizing background.

2.3 Evolution of the Ionizing Background

2.3.1 The Ionizing Background With Uniform Emissivity

The solid curve in Figure 2.4 shows how the He II ionization rate ($\Gamma_{\rm He\,II}$) evolves in our *uniform* fiducial model, ignoring fluctuations in the ionizing background. The uniform background model results in a steeply evolving ionizing background from $z \sim 3$–2, with an ionization rate that increases by a factor of ~ 2 over that range before flattening out substantially at later times. In the following sections, we discuss how variations in the input parameters affect this result.

2.3.1.1 Column Density Distribution

We considered a variety of CDDFs in our model. The top panel of Figure 2.5 shows the uniform ionizing background calculated with CDDFs used in earlier ionizing background calculations by Haardt & Madau (2012) and Faucher-Giguère et al. (2009), the direct measurement at $\langle z \rangle \sim 2.4$ by Rudie et al. (2013), and indirect extrapolation from higher redshift

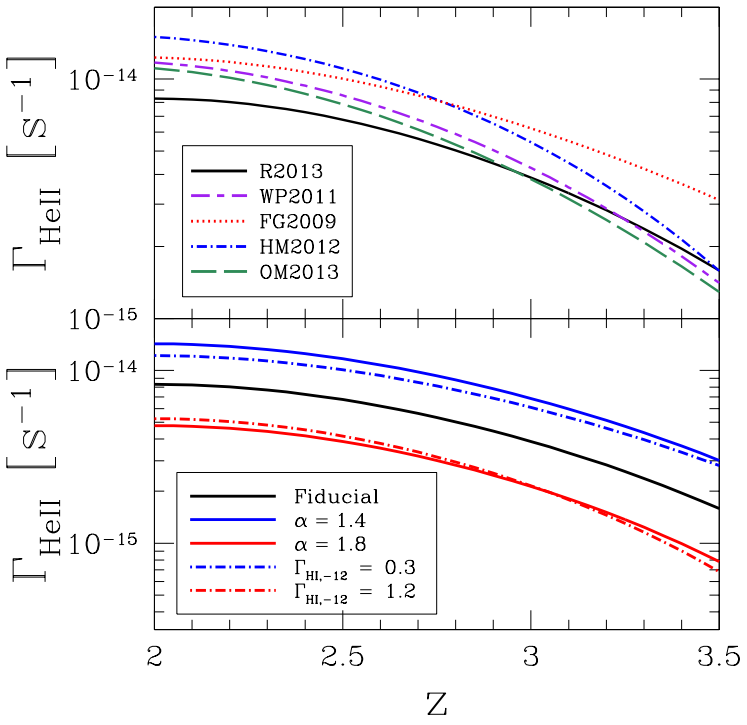

Figure 2.5: Top: $\Gamma_{\rm He\,II}$ in the uniform background model calculated for CDDFs from Figure 2.3. Bottom: Effect of assumed average quasar spectrum shortward of 912 Å, given by $F_\nu \propto \nu^{-\alpha}$ (solid curves), and assumed (constant) $\Gamma_{\rm H\,I}$ (dot-dashed curves).

opacity measurements (Worseck & Prochaska, 2011; O'Meara et al., 2013). In general, despite the significant differences between CDDFs apparent in the left panel of Figure 2.3, the evolution of the uniform background from $z = 3$–2 is fairly insensitive to the CDDF. The most significant differences are due to the different redshift evolution of the CDDFs, which is not very well constrained.

The right panel of Figure 2.3 shows the relative contribution to the ionizing continuum opacity at the He II edge as a function of $N_{\rm H\,I}$. Most of the opacity is due to He II "LLSs" with $N_{\rm He\,II} \sim \sigma_{\rm He\,II}^{-1}$, but the multi-step power law CDDFs have an increased contribution from relatively low $N_{\rm H\,I}$ ($\lesssim 10^{15}$ cm^{-2}) absorbers compared to the shallow power law Faucher-Giguère et al. (2009) CDDF. The H I column density corresponding to the peak He II opacity contribution varies from 10^{15} to $10^{16.7}$ cm^{-2} depending on the shape of the CDDF.

Figure 2.5 also shows that the normalization of $\Gamma_{\rm He\,II}$ depends sensitively on the total opacity calculated from the CDDF, which can vary significantly between models. If $\Gamma_{\rm He\,II}$ were accurately measured near $z \sim 2$, that measurement could in principle be used to help distinguish between models. However, measuring $\Gamma_{\rm He\,II}$ directly is extremely difficult, and as shown in the following sections, the other model parameters can be adjusted to produce similar differences in the normalization. For example, measurements of both the $\eta_{\rm thin}$ parameter and $\Gamma_{\rm H\,I}$ could potentially be used to constrain acceptable normalizations of $\Gamma_{\rm He\,II}$ (because the expected He II Lyα opacity in the IGM depends strongly on the value of the former parameter; see equation 2.6), but the current constraints on these parameters are too weak, and the degeneracies are too strong, to distinguish between the models presented in this and the following sections.

2.3.1.2 Quasar Spectrum

To assess the effect of choosing different average far-ultraviolet quasar spectral indices, we fix the H I Lyman limit emissivity given by equation 2.19 and scale to He II ionizing photons by $\epsilon_\nu \propto \nu^{-\alpha}$. The solid curves in the bottom panel of Figure 2.5 show how the range of observed values of the quasar spectral index α affects the He II ionization rate. A harder spectrum,

which produces more ionizing photons at $\nu_{\rm He\,II}$, results in a higher ionization rate. Fixing the emissivity at $\nu_{\rm He\,II}$ and changing the spectral index has very little effect on the resulting $\Gamma_{\rm He\,II}$. In contrast, we find that $\Gamma_{\rm He\,II}$ changes more strongly than linearly with $\epsilon_{\rm He\,II}$; this is because the absorber structure changes with the ionizing background (and hence the emissivity). In general, as $\Gamma_{\rm He\,II}$ increases, the H I column density corresponding to a He II LLS increases. Since $N_{\rm H\,I} f(N_{\rm H\,I}, z)$ is a decreasing function of $N_{\rm H\,I}$, the number density of He II LLSs, and thus the overall opacity, decreases. This behaviour is similar to the emissivity-Γ feedback studied by McQuinn et al. (2011). The redshift evolution of the background is affected by α as well, but the effect is subtle.

2.3.1.3 H I Ionization Rate

The dot-dashed curves in the bottom panel of Figure 2.5 show how the He II ionization rate is affected by the assumed value of $\Gamma_{\rm H\,I}$. The effect is similar to changing the number of He II ionizing photons, because both parameters modulate the ratio of He II to H I in absorbers. While the decrease in He II opacity with an increasing number of He II ionizing photons is straightforward in principle, the relationship between $\Gamma_{\rm H\,I}$ and $\Gamma_{\rm He\,II}$ is more subtle. Consider an optically thin absorber: if $\Gamma_{\rm H\,I}$ decreases, the amount of H I in a fixed physical structure will increase while the amount of He II stays the same. This shift of the H I column density corresponding to a He II LLS causes $\Gamma_{\rm He\,II}$ to change with $\Gamma_{\rm H\,I}$: if $\Gamma_{\rm H\,I}$ is larger, the $N_{\rm H\,I}$ corresponding to a He II LLS will decrease, so He II LLSs will be more numerous and the overall He II opacity will increase. $\Gamma_{\rm H\,I}$ appears to affect the redshift evolution more strongly than α.

2.3.1.4 Mean Free Path

The solid curve in Figure 2.6 shows the evolution of $\bar{\lambda}_{\rm He\,II}$ in the uniform model. We also show how $\lambda_{\rm H\,I}$ increases with cosmic time (dotted curve); for ease of comparison we scale this curve to $\bar{\lambda}_{\rm He\,II}$ at $z = 2$. In contrast to the power-law evolution of $\lambda_{\rm H\,I}$ (described by equation 2.13), $\bar{\lambda}_{\rm He\,II}$ evolves much faster than a simple power law.

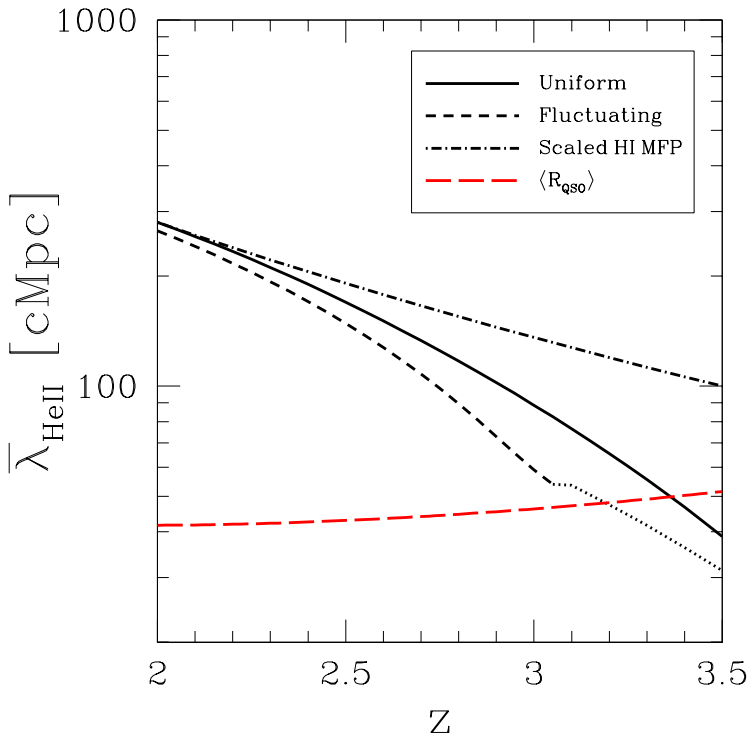

Figure 2.6: Evolution of the He II ionizing photon mean free path with redshift (black), evaluated at the average ionizing energy, for the uniform (solid) and fluctuating (dashed) models. The dotted curve represents the results of the fluctuating model when it is inconsistent with the minimum expected background from §2.2.4 as in Figure 2.4. The evolution of the hydrogen ionizing photon mean free path is shown as the dot-dashed curve, scaled to the He II mean free path at $z = 2$. The red long-dashed curve shows the average separation between luminous ($\nu_B L_B > 10^{11} L_\odot$) quasars given by the Hopkins et al. (2007) QLF.

The evolution of the mean free path at the He II ionizing edge in our fiducial model is well-approximated by a power law with an index that itself evolves as a power law,

$$\lambda_{\rm He\,II} \sim 188 \text{ comoving Mpc} \times \left(\frac{1+z}{3}\right)^{\zeta(z)} \quad (2.21)$$

$$\zeta(z) = -2.41 \times \left(\frac{1+z}{3}\right)^{1.92}. \quad (2.22)$$

This fit differs by no more than $\sim 3\%$ from our full numerical calculations over the redshift range $z = 2$–3.8, but we caution the reader that the systematic uncertainties from our model input parameters are much, much larger than this. We also caution the reader against using this fit at $z \gtrsim 3.4$, where fluctuations in the ionizing background *must* be included (see below).

Because $\lambda_{\rm He\,II}$ is linked to $\Gamma_{\rm He\,II}$ through the absorber structure prescription, it evolves more quickly than $\lambda_{\rm H\,I}$. That is, increasing the mean free path increases the ionizing background, which will then increase the H I column density at which He II becomes optically thick, which in turn increases the mean free path, etc. This feedback effect is the fundamental source of the rapid evolution we see in $\Gamma_{\rm He\,II}$. (In fact, one could argue that it is strange that such rapid evolution does *not* occur in $\Gamma_{\rm H\,I}$; see McQuinn et al. 2011.)

The dependence of the mean free path on frequency is a function of the logarithmic slope of the CDDF, $\lambda_{\rm mfp} \propto \nu^{3(\beta-1)}$ (equation 2.13). The He II CDDF is not precisely defined in our model, but a mapping of our fiducial H I CDDF through our absorber prescription results in $\beta_{\rm He\,II} \sim 1.43$ for the absorbers that contribute the bulk of the opacity near the He II ionizing edge ($10^{14.5} \lesssim N_{\rm H\,I} \lesssim 10^{17.0}$ cm^{-2} as in Figure 2.3), and consequently $\lambda_{\rm He\,II} \propto \nu^{1.3}$ for $1 \leq \nu/\nu_{\rm He\,II} \lesssim 2.5$. $\bar{\nu}/\nu_{\rm He\,II} \sim 1.37$ is typical for our fiducial model, so $\bar{\lambda}_{\rm He\,II}/\lambda_{\rm He\,II} \sim 1.51$.

2.3.1.5 Recombination Photons

The fractional contribution of recombination emission to $\Gamma_{\rm He\,II}$ is fairly minor. In the absence of quasars, but with the opacity as a function of redshift fixed to the uniform model, recombination photons alone produce an ionization rate about ~ 7–15% of the fiducial value. However, because the absorber population is sensitive to the emissivity (as in § 2.3.1.2), the

relative difference between $\Gamma_{\rm He\,II}$ calculated with recombination emission and $\Gamma_{\rm He\,II}$ calculated without recombination emission is larger ($\sim$ 20–40%). While Faucher-Giguère et al. (2009) found that including recombination emission increased $\Gamma_{\rm He\,II}$ by only $\sim$ 10%, Figure 2.3 shows that their CDDF has a significant deficit of the optically thin ($N_{\rm H\,I} \lesssim 10^{16}$ cm^{-2}) systems that contribute most of the recombination emissivity.

In simple models of the reionization process, it is conventional to describe the enhanced recombination rate of ionized species n_i due to an inhomogeneous IGM through the so-called clumping factor, $C = \langle n_i n_e \rangle / (\langle n_i \rangle \langle n_e \rangle)$. Usually, this is estimated from simple phenomenological arguments or from the density structure in numerical simulations. However, these approaches are not entirely satisfactory, as the clumping factor should incorporate information that depends on the distribution of ionized and neutral patches. For example, recombinations that occur inside of dense, self-shielded systems do not produce photons that can ionize the IGM, as the resulting photons are trapped within the systems.

With our detailed model, we can estimate this factor for He III self-consistently (given a model for the emitting and absorbing populations) by explicitly following the fraction of recombinations that occur inside of self-shielded systems. In particular, we have

$$C_{\rm eff} = \frac{\int_{\nu_{\rm He\,II}}^{\infty} \epsilon_{\nu,{\rm rec}}/(h\nu) d\nu}{(\alpha^{A}_{\rm He\,II} - \alpha^{B}_{\rm He\,II}) \langle n_{\rm He\,III} \rangle \langle n_e \rangle}, \tag{2.23}$$

which describes the effective recombination rate after correcting for self-absorption of ionizing recombination photons within the emitting clouds relative to a uniform IGM. In our fiducial uniform model, $C_{\rm eff}$ increases from $C_{\rm eff} \sim 1$ at $z = 3.5$ to $C_{\rm eff} \sim 4$ at $z = 2$.

2.3.2 The Ionizing Background Including Fluctuations

It is instructive to compare the mean free path from the preceding section to the average separation between the primary sources of ionizing photons, bright quasars with $\nu_B L_B > 10^{11} L_\odot$. We calculate the number density of the bright quasars by integrating the Hopkins et al. (2007) luminosity function over this luminosity range and estimating their average separation by $\langle R \rangle \sim n^{-1/3}$. The long-dashed red curve in Figure 2.6 shows this separation; $\langle R \rangle \sim 45$ Mpc is a good approximation for the entire redshift interval from $z \sim 2$–3.

When the mean free path is similar to the average source separation, fluctuations in the background contribute a substantial opacity excess. The dashed curve in Figure 2.4 shows the effect of these fluctuations on the ionizing background. Figure 2.7 shows that, compared to the uniform model, the fluctuating background model exhibits a ~ 20–40% dip at $z \sim 3$–3.2 for our fiducial input parameters and various CDDFs from § 2.3.1.1. The evolution of all the CDDF models, with the exception of the shallow slope model from Faucher-Giguère et al. (2009), is very similar. The "feedback" effect between the opacity and the ionizing background is weaker for shallower CDDF slopes (e.g. McQuinn et al. 2011), so the net effect of fluctuations is smaller in the Faucher-Giguère et al. (2009) model. The "recovery" of the fluctuating model at higher redshift relative to the uniform model is due to our minimum ionization rate approximation from Section 2.2.4 which limits the effective opacity to ionizing photons.

We note that there are two related sources for the differences between the curves in Figure 2.7: the shape of the column density distributions and the normalization of the ionizing background. Leaving the CDDF shape fixed, different choices for the ionizing emissivity result in very similar shapes to those in Figure 2.7, though the redshift above which the minimum background is larger than the fluctuating background will shift depending on the relative normalization of the two models. The more subtle differences in the shapes of the curves are due to variations in the shape of the CDDF; this is most dramatically seen by the dotted curve (which is only below the minimum background model at $z \gtrsim 3.8$).

The most important effect of including fluctuations is to induce a more rapid increase in $\Gamma_{\rm He\,II}$ with cosmic time. Consider a region with a smaller than average emissivity. In that region, the ionizing background will also be smaller, so each absorber will be more optically thick and the mean free path will be smaller. This will further decrease the ionizing background, etc. In a realistic model of the distribution of $\Gamma_{\rm He\,II}$ in the presence of quasars, most of the volume of the universe has an ionizing background a few times *below* the universal average (to compensate for the very brightly illuminated, but small, regions around quasars; see Figure 2.1). Thus, the average opacity through the universe is higher, decreasing the resulting mean ionizing background.

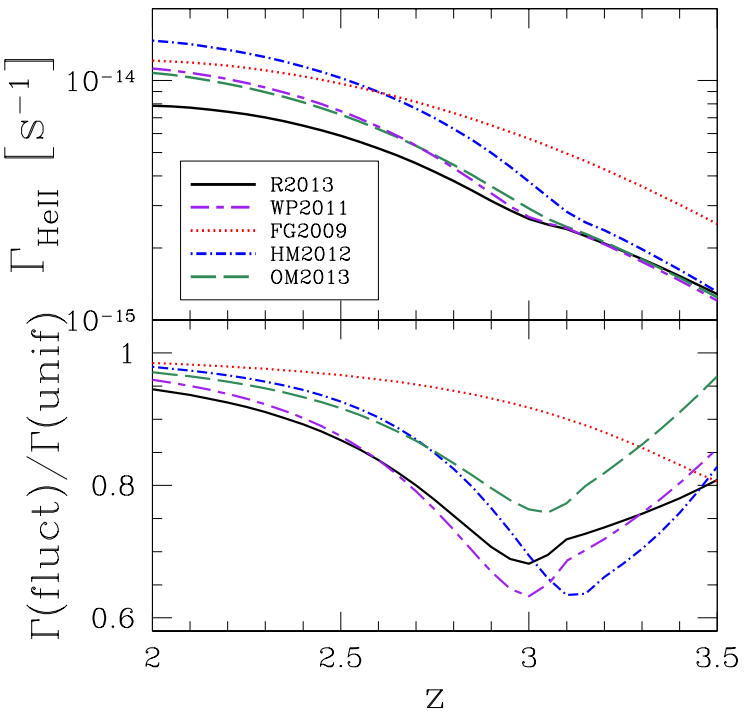

Figure 2.7: Top: Fluctuating model ionization rate for the same CDDFs as Figure 2.3. Bottom: Ratio of the fluctuating and uniform model ionization rates.

The turndown from the uniform model is thus a straightforward and robust prediction of our fluctuating background model, though its magnitude depends on the CDDF. At higher redshift ($z \gtrsim 3$), it is clear that the He II ionizing background evolution should no longer be described by a cosmological radiative transfer model without properly taking into account the effect of localized transparent regions around sources. Our simple analytic model for the minimum ionization rate from isolated quasars, the minimum background model, should represent a fairly strict lower limit to the ionizing background in the post-reionization (i.e. ionization equilibrium) limit. If this is indeed the case, one might expect the volume-averaged ionization rate to evolve *more slowly* at higher redshift ($z \gtrsim 3.1$) than predicted by standard cosmological radiative transfer. While our minimum model neglects a diffuse partially-neutral component to the IGM that should exist prior to the completion of He II reionization, this slower evolution is consistent with the He II reionization simulations of McQuinn et al. (2009) and with expectations from hydrogen reionization (Furlanetto & Mesinger, 2009). In both cases, the ionizing background is reduced to a set of independent "proximity zones" (though for different reasons), with the mean background depending principally on the filling factor of these regions.

These calculations show that the ionizing background can evolve very rapidly at $z \lesssim 3$, *even without any assumptions about an evolving He II fraction.* The precise degree of evolution is uncertain, but it is at least a factor of a few–even in the standard uniform emissivity model–and likely nearly a factor of five when fluctuations are included. In other words, even without late He II reionization, we should see a rapid increase in the intensity of the metagalactic radiation field. This evolution is in stark contrast to observations of the H I ionization rate, which appears to be roughly constant from $z \sim 2$–4; this difference is most likely due to the increasing influence (towards higher redshift) of star-forming galaxies (as opposed to quasars) to the H I ionizing emissivity. We will consider the observable implications of this conclusion in the following section.

For $z \lesssim 3$, the mean free path at the He II ionizing edge in the fluctuating background model is well-characterized by a similar power law within a power law as the uniform model

(equation 2.21),

$$\lambda_{\mathrm{He\,II}} \sim 178 \text{ comoving Mpc} \times \left(\frac{1+z}{3}\right)^{\zeta(z)} \tag{2.24}$$

$$\zeta(z) = -2.64 \times \left(\frac{1+z}{3}\right)^{2.61}. \tag{2.25}$$

The primary difference between the uniform and fluctuating background fits is the larger power law index of $\zeta(z)$, a consequence of faster ionizing background evolution. As discussed previously, the mean free path of average energy ionizing photons that we use in the fluctuating background calculation is somewhat larger:

$$\bar{\lambda}_{\mathrm{He\,II}} \sim 266 \text{ comoving Mpc} \times \left(\frac{1+z}{3}\right)^{\zeta(z)} \tag{2.26}$$

$$\zeta(z) = -2.62 \times \left(\frac{1+z}{3}\right)^{2.38}. \tag{2.27}$$

2.4 Effective Optical Depth

To gauge the observable import of our results, we will briefly consider how they manifest in the evolution of the IGM opacity to far-ultraviolet photons. He II Lyα absorption has been measured in far-ultraviolet spectra from $z \sim 2$–4 (Dixon & Furlanetto 2009 and references therein; Worseck et al. 2011; Syphers et al. 2011, 2012; Syphers & Shull 2013). We will compare to the most basic observable from the resulting forest of observed absorption features, the average optical depth τ_{eff} for the He II Lyα transition. We use two different methods to predict τ_{eff}: a semi-analytic model using a gas density probability distribution $P(\Delta)$ as in Dixon & Furlanetto (2009), and a direct integration of the He II Lyα opacity from the H I CDDF and our absorber structure prescription.

Under the assumptions of a highly-ionized universe in ionization equilibrium, line opacity dominated by zero-width optically thin absorbers, and a power-law temperature-density relation $T = T_0 \Delta^{1-\gamma_d}$, the He II Gunn-Peterson optical depth can be expressed as (Dixon & Furlanetto, 2009)

$$\tau_{\mathrm{GP}} \simeq 13.6\kappa \left(\frac{\Gamma_{\mathrm{He\,II}}}{10^{-14}\,\mathrm{s}^{-1}}\right)^{-1} \left(\frac{T_0}{10^4\,\mathrm{K}}\right)^{-0.7} \left(\frac{\Omega_b h^2}{0.0241}\right)^2$$

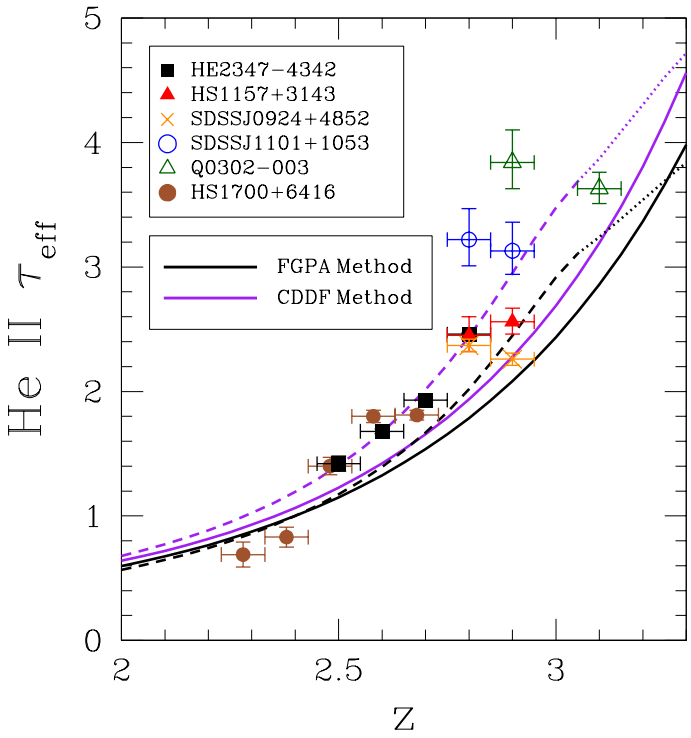

Figure 2.8: Effective optical depth for the uniform (solid), fluctuating (dashed), "plateau" (dotted), and "minimum" (dash-dotted) models, using the FGPA (black) and CDDF (purple) methods. The points are $\Delta z = 0.1$-binned effective optical depth data for various quasar sightlines from Syphers & Shull (2013) ((HS1700+6416, filled brown circles; excluding metal absorption) and Worseck et al. (2011) (G. Worseck, priv. comm.; HE2347-4342, black squares; HS1157+3143, filled red triangles; SDSSJ0924+4852, orange crosses; SDSSJ1101+1053, open blue circles; Q0302-003, open green triangles).

$$\times \left(\frac{\Omega_m h^2}{0.142}\right)^{-1/2} \left(\frac{1+z}{4}\right)^{9/2} \Delta^{2-0.7(\gamma_d-1)}. \quad (2.28)$$

This "fluctuating Gunn-Peterson approximation" (FGPA; Weinberg et al. 1997) relates the continuum optical depth to the local overdensity Δ and ionization rate $\Gamma_{\rm He\,II}$. The systematic uncertainty in $\tau_{\rm GP}$ due to the above simplifications is collapsed into a normalization constant κ, which we calibrate to (one of) the observations. We assume an isothermal temperature-density relation ($\gamma_d = 1$) for simplicity, but this does not affect our results significantly. Assuming the gas density probability distribution given by Miralda-Escudé et al. (2000), we then calculate $\tau_{\rm eff}$ by integrating over the density and ionization rate distributions:

$$e^{-\tau_{\rm eff}} = \int_0^\infty d\Gamma f(\Gamma) \int_0^\infty d\Delta e^{-\tau_{\rm GP}(\Gamma,\Delta)} P(\Delta). \quad (2.29)$$

We normalized the FGPA results for the uniform and fluctuating models to produce an optical depth of $\tau = 1.0$ at $z = 2.4$ to roughly match observations (Worseck et al., 2011; Syphers & Shull, 2013) when the expected variation between sightlines is small. These normalizations require $\kappa = 1.56$ and $\kappa = 1.28$ (equation 2.28) for the uniform and fluctuating models, respectively.

An alternative method to calculate $\tau_{\rm eff}$ is to directly integrate the He II Lyα opacity from the CDDF. The only additional information needed is the distribution of line widths, provided by the Doppler parameter b. In this method, $\tau_{\rm eff}$ is given by (Zuo, 1993)

$$\tau_{\rm eff} = \frac{1+z}{\lambda_{\rm He\,II,Ly\alpha}} \times \int_{N_{\rm H\,I,min}}^{N_{\rm H\,I,max}} dN_{\rm H\,I} \int_0^\infty db f(N_{\rm H\,I}, b) W(N_{\rm H\,I}, b), \quad (2.30)$$

where $W(N_{\rm H\,I}, b)$ is the He II Lyα equivalent width of an absorber with Doppler parameter b and $f(N_{\rm H\,I}, b)$ is the joint distribution of $N_{\rm H\,I}$ and b. We assume that $N_{\rm H\,I}$ and b are uncorrelated and that the distribution of b is a Dirac-delta function at $b = 30$ km s^{-1}, a representative approximation for H I Lyα forest systems (Kim et al., 2001). In this method we do not subject the resulting optical depth to any extra normalization.

The results of the FGPA and CDDF methods are shown in Figure 2.8. Both methods demonstrate that steep evolution of $\Gamma_{\rm He\,II}$ naturally leads to steep evolution in the observed

$\tau_{\rm eff}$. The addition of fluctuations further accelerates the evolution. The results for different input parameters (α, $\Gamma_{\rm H\,I}$, CDDF) are largely the same in the FGPA method when normalized at $z = 2.4$. In contrast, the CDDF method depends sensitively on $\eta_{\rm thin} \propto \Gamma_{\rm H\,I}/\Gamma_{\rm He\,II}$ (equation 2.6), which can differ by a factor of a few between models. Thus, for a given CDDF, the He II optical depth places a joint constraint on $\Gamma_{\rm H\,I}$ and α, subject to the uncertainties inherent in our cosmological radiative transfer model.

For context, we also show measured $\tau_{\rm eff}$ points in Figure 2.8 from Syphers & Shull (2013) and Worseck et al. (2011). These two works determine the effective optical depth by measuring the transmission uniformly across the redshift interval ($\tau_{\rm eff} = -\ln\langle F\rangle$) instead of averaging transmission from sparse redshift coverage provided by past works (Dixon & Furlanetto, 2009) or averaging pixel optical depths (Shull et al., 2010). It is interesting that our models – which explicitly ignore He II reionization – match the evolution in the observed optical depth rather well. Additionally, the fluctuating background models appear to match the observations more closely than the uniform models, especially at $z \gtrsim 2.7$ where the observed optical depth evolution is very steep. Our result demonstrates that the observed trend in and of itself does not *require* the He II fraction to evolve, although it also does not rule out such evolution.

Unfortunately, our models do not explicitly describe how the integrated $\tau_{\rm eff}$ should vary at the same redshift along different lines of sight, even when averaged over large path lengths. This is because our model assumes that the high and low Γ regions are distributed perfectly randomly, without the spatial correlations between them that are essential to understanding the observed averages (Furlanetto & Dixon, 2010). Hydrodynamic simulations by McQuinn et al. (2009) and semi-analytic models by Furlanetto & Dixon (2010) have described spatial variations in $\tau_{\rm eff}$. Interestingly, the well-studied spectrum of HE 2347–4342 (Reimers et al., 1997; Kriss et al., 2001; Zheng et al., 2004; Shull et al., 2004, 2010) shows regions of high optical depth that appear to require large swathes of He II at $2.7 \lesssim z \lesssim 2.9$. We therefore emphasize that our models do not demand that He II reionization be over by $z \sim 3$; they instead demonstrate that, with respect to the evolution of the mean opacity, it is not required.

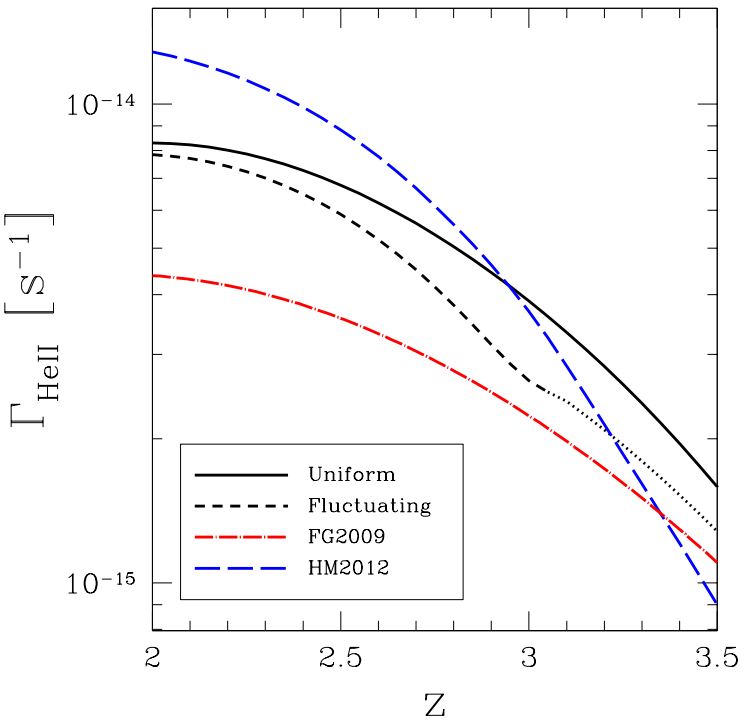

Figure 2.9: Uniform (solid black) and fluctuating (dashed black) He II ionization rate from this work compared to the models from Haardt & Madau (2012) (long-dashed blue) and Faucher-Giguère et al. (2009) (long-dash-dotted red).

2.5 Discussion

Our model for background fluctuations increases the average opacity of the IGM when the mean free path is comparable to the separation between bright sources. This effect is primarily due to the skewness of $f(\Gamma)$ towards lower Γ as the mean free path decreases (as in Figure 2.1). While the effect of our fluctuations prescription on the ionizing background is relatively small, it predicts a steep increase in the ionizing background when the background transitions from being dominated by local sources to a smoother background with contributions from distant sources.

2.5.1 Comparison to past theoretical work

Figure 2.9 shows how our model compares to a pair of recent ionizing background calculations by Haardt & Madau (2012) and Faucher-Giguère et al. (2009).

Faucher-Giguère et al. (2009) used a single power-law CDDF with $\beta = 1.4$ and $\gamma = 1.5$ that severely underestimates the number of low-density Lyα forest absorbers compared to recent observations (see the left panel of Figure 2.3) and evolves more slowly than implied by Lyα forest measurements (Kim et al., 2002a). Because their CDDF severely underestimates the H I opacity of the IGM from sub-LLS absorbers, they were forced to renormalize the quasar emissivity of ionizing photons at the hydrogen ionizing edge by a factor of 0.36 to match their measured $\Gamma_{\rm H\,I} \sim 0.5 \times 10^{-12}$ s^{-1} (Faucher-Giguère et al., 2008a), and thus their $\Gamma_{\rm He\,II}$ is normalized somewhat lower as well. Their $\Gamma_{\rm He\,II}$ evolves at a similar rate to our fiducial uniform background model.

Haardt & Madau (2012) used a CDDF that evolves more rapidly with redshift than our fiducial model and calculated a $\Gamma_{\rm H\,I}$ that peaks at $z \sim 2$ and declines slowly towards higher redshift. They also used a different fitting form for the structure of IGM absorbers. In their fit they more accurately approximated the average ionization rate within absorbers, which resulted in a more accurate fit to η at large H I column densities. However, as mentioned previously in § 2.2.1.1, those high $N_{\rm H\,I}$ systems do not contribute a substantial fraction of the opacity near the He II edge, and thus our approximation should not significantly affect our results.

2.5.2 Fluctuating Model Caveats

Other than the general simplifications necessary to invoke the cosmological radiative transfer model, our parameterization of the fluctuations in the background is an ad hoc addition to a model designed for a medium with a uniform emissivity. In this section, we describe the primary uncertainties with such an approach.

First of all, we may not have accurately captured the extent and character of the fluctuations. Spatial correlations in the ionizing background exist due to the large proximity regions

of the primary sources (as seen in the minimum model of § 2.2.4). It is possible that a full characterization of the ionizing background fluctuations including proximity effects would negate the need to separately consider the minimum background due to isolated sources, though obviously such an effort is different. Additionally, the massive hosts of these luminous quasars are clustered, which will increase the amplitude of the fluctuations. However, the proximity zones of the quasars are so large, and the quasars so rare, that stochastic variations dominate over large-scale clustering in all reasonable scenarios anyway (Dixon et al., 2014). The absorbers also show some clustering (Rudie et al., 2012; Rudie et al., 2013) which will modulate the metagalactic radiation field (although likely only modestly).

Other obvious sources of additional fluctuations in the ionizing background – over and above those from the discrete sources – include radiative transfer effects (e.g. "shadows" behind optically thick regions as in Tittley & Meiksin 2007) and collisional ionization in superheated shocks (Muzahid et al., 2011). Of course, incomplete He II reionization may leave opaque patches of He II that would introduce severe fluctuations (McQuinn et al., 2009; Furlanetto & Dixon, 2010) which have possibly been observed recently (Zheng et al., 2004; Shull et al., 2010; Worseck et al., 2011). We have explicitly ignored this possibility here so as to consider the evolution of the ionizing background in the absence of such effects.

We also treat recombinations only approximately. We include recombination emission in our fluctuating model calculation in the same way as in the uniform model, by simply adding to the pre-existing quasars' emissivity. It therefore implicitly has the same source distribution, while in fact it will be more uniform than the point-like quasars because it is distributed throughout the IGM. On the other hand, recombination emission in low $\Gamma_{\rm He\,II}$ regions will be weaker, and much of the emission from high $\Gamma_{\rm He\,II}$ regions (i.e. near bright quasars) will not travel much beyond those quasar proximity regions before redshifting below $\nu_{\rm He\,II}$ ($\lesssim 30$ Mpc; § 2.2.1.2), so its effect on $f(\Gamma)$ should be fairly minor.

2.6 Conclusion

We have calculated the He II ionizing background using a cosmological radiative transfer model that takes into account the latest constraints on quasar and IGM source properties. In our uniform background model, which closely mimics previous work (Fardal et al., 1998; Faucher-Giguère et al., 2009; Haardt & Madau, 2012), we found that the He II ionization rate, $\Gamma_{\rm He\,II}$, and the mean free path of He II ionizing photons should both evolve significantly during the time after He II reionization ($z \sim 2-3$). However, at $z \sim 3$, the mean free path of He II ionizing photons is comparable to the average distance between the bright quasars that contribute most of the ionizing emissivity. While previous work investigated how this effect introduces fluctuations in the ionizing background (Fardal et al., 1998; Meiksin & White, 2003; Furlanetto, 2009), its implications for the *mean* ionizing background itself have not been studied in detail until now.

We investigated for the first time how these fluctuations can affect the evolution of the mean background. We incorporated the distribution $f(\Gamma)$ into our cosmological radiative transfer model by averaging the opacity to He II ionizing photons over it. However, that procedure still models the emission as diffuse sources rather than point-like quasars, so we supplemented it with a physical model that accounts for the decreased average opacity at high redshift by considering *isolated* transparent zones around individual quasars. Including that model, our results showed that the fluctuating background introduces another source of opacity which causes the ionization rate to decrease by a factor of $\sim 30\%$ at $z \sim 3.1$ relative to the uniform background calculation. For $z \gtrsim 3.1$, the cosmological radiative transfer model predicts a mean background below the minimum model, suggesting that it is no longer adequate to properly model the evolution of the He II ionizing background at those redshifts.

As an example of the utility of our ionizing background model, we used the resulting ionization rate to estimate the evolution of the He II Lyα effective optical depth, $\tau_{\rm eff}$. Rapid evolution at $z \gtrsim 2.5$, similar to that seen in observations, appears to be a natural consequence of a steeply evolving ionization rate. The addition of fluctuations improves our model's

resemblance to the observed $\tau_{\rm eff}$ evolution somewhat, though systematic uncertainties in the data analysis make a detailed comparison difficult.

We note that our model does not incorporate He II reionization: that is, we assume that the He II fraction is very small throughout the IGM. We have therefore shown that reionization is not the *only* possible cause of a rapidly evolving ionizing background. Instead, the interaction between the (slowly) increasing emissivity and the (slowly) evolving IGM clumpiness can feed back on each other, strongly amplifying the evolution of the ionizing background. Such evolution is naively predicted by simple models (McQuinn et al., 2011) but is not observed in the hydrogen-ionizing background at these redshifts.

Our result emphasizes the importance of understanding the IGM for interpreting measurements of the ionizing background and of reionization, including that of both He II and H I. In the context of He II reionization, Dixon & Furlanetto (2009) argued that the rapidly increasing mean optical depth in the He II Lyα line is consistent with ongoing He II reionization at $z \gtrsim 2.7$. However, they prescribed a relatively slow evolution in the mean free path of ionizing photons. On the other hand, a number of observations show substantial fluctuations in the mean optical depth, even when averaged over large scales (Reimers et al., 1997; Zheng et al., 2004; Shull et al., 2004, 2010). Our model does not address such large-scale fluctuations, because we have not incorporated any spatial information into the calculation.

This calculation may also have important implications for H I reionization, where an apparent rapid increase in the H I Lyα optical depth has long been attributed to the tail end of reionization (Fan et al., 2002; Fan et al., 2006). Furlanetto & Mesinger (2009) previously showed that the overlap process of reionization (when ionized bubbles overlap to fill space) does not by itself cause a rapid increase in the ionizing background. We have shown that such an increase can be caused by "normal" post-reionization processes, through the interaction of a slowly increasing emissivity and slowly decreasing IGM clumping. Whether this occurs during H I reionization cannot be said, because it depends sensitively on the evolution of that clumping (which is largely hidden due to the high opacity of the Lyα forest beyond $z \sim 6$). However, this He II analog indicates that a proper interpretation of data regarding H I reionization requires careful modelling (and ideally observations) of the IGM and not

simply an understanding of the emitting sources.

CHAPTER 3

A self-consistent 3D model of fluctuations in the helium-ionizing background

3.1 Introduction

The hydrogen and helium reionization epochs produce some of the largest scale features in the Universe. They reflect the cumulative ionizing photon output of galaxies and black holes, or in other words, the history of star formation and supermassive black hole accretion across cosmic time. Helium reionization is believed to finish at $z \sim 3$–4, when quasars start to dominate the ionizing photon production in the universe (e.g. Sokasian et al. 2002; Wyithe & Loeb 2003; Furlanetto & Oh 2008b). Occurring near the peak era of star and black hole formation, this is the last global transition experienced by the intergalactic medium (IGM) and significantly heats that material (e.g. Theuns et al. 2002; Hui & Haiman 2003; Bolton et al. 2009). This heating indirectly affects the star formation history of the Universe (by influencing its fuel supply) as well as observables like the H I Lyα forest. The He II-ionizing background also offers the prospect of shedding light on the sources that drive it, including the abundance, spectra, lifetimes, and emission geometries of quasars (e.g. Worseck & Wisotzki 2006; Worseck et al. 2007; Furlanetto & Lidz 2011).

Observations of substantial transmission through the He II Lyα forest below $z \sim 2.7$ (Davidsen et al., 1996; Kriss et al., 2001; Zheng et al., 2004; Fechner et al., 2006) suggest that helium reionization is complete by that epoch. At $z \gtrsim 2.7$, however, the He II Lyα forest opacity rapidly increases and significant fluctuations in the He II Lyα effective optical depth $\tau_{\rm eff}$ arise on scales ranging from 10–100 comoving Mpc (e.g. Reimers et al. 1997; Heap et al. 2000; Shull et al. 2004). Recent observations with HST/COS have confirmed these

features (Shull et al., 2010; Worseck et al., 2011; Syphers & Shull, 2013, 2014) and continue to increase the number of He II Lyα forest sightlines (Syphers et al., 2012; Worseck et al., 2014a). Straightforward models of the He II ionizing background with a uniform mean free path of ionizing photons cannot explain the fluctuations observed at $z \gtrsim 2.7$ (Furlanetto & Dixon, 2010), suggesting that the culprit is incomplete helium reionization (see also Worseck et al. 2011). This interpretation appears to be in moderate tension with the existence of regions with significant He II transmission at $z \sim 3.5$ (Worseck et al., 2014a; Compostella et al., 2014). Unfortunately, the era immediately following He II reionization has not been well-studied, as radiative transfer simulations (which have mostly focused on the reionization process) are expensive and hence limited to "best-guess" parameters.

Davies & Furlanetto (2014; henceforth DF14) showed that fluctuations in the ionizing background could play an important role in the evolution of the *mean* background by inducing spatial variations in the opacity to ionizing photons. Toward higher redshifts, as the opacity of the IGM to He II-ionizing photons increases, the fluctuations in the background similarly increase (Furlanetto, 2009), leading to a rapidly evolving ionizing background. However, once these fluctuations become an important source of additional opacity the assumption of uniform emission and absorption of ionizing photons in commonly used 1D cosmological radiative transfer models (Haardt & Madau, 1996, 2012; Faucher-Giguère et al., 2009) breaks down. A full treatment of these effects requires a 3D realization of Γ-dependent opacity and discrete ionizing sources. In this work we construct such a model and find that it can describe the observed evolution of $\tau_{\rm eff}$ and its variations between sightlines decently well even under the assumption of a post-reionization universe.

The structure of the paper is as follows. In Section 3.2, we outline our prescription for the fluctuating opacity of the IGM to He II-ionizing photons. In Section 3.3, we describe our numerical model for computing the ionizing background and qualitatively discuss the effect of a fluctuating mean free path. In Section 3.4, we employ a simple prescription for the He II Lyα forest to relate our ionizing background model to observations. In Section 3.5, we discuss the uncertainties of our simplified approach. Finally, in Section 3.6 we conclude by discussing the implications of our model and future improvements that will enhance its

predictive power.

In this work we assume a standard ΛCDM cosmology with $H_0 = 70\,\mathrm{km/s/Mpc}$, $\Omega_m = 0.3$, and $\Omega_\Lambda = 0.7$. Distance units should be assumed to be comoving unless otherwise specified.

3.2 The Opacity of the IGM to Ionizing Photons

The opacity of the IGM to ionizing photons can be parameterized by the optical depth per unit redshift,

$$\frac{d\bar{\tau}}{dz}(\nu, z) = \int_0^\infty dN_{\mathrm{H\,I}} f(N_{\mathrm{H\,I}}, z)(1 - e^{-\tau_\nu}), \tag{3.1}$$

where $f(N_{\mathrm{H\,I}}, z)$ is the H I column density distribution function (CDDF), and

$$\tau_\nu = N_{\mathrm{H\,I}}\sigma_{\mathrm{H\,I}}(\nu) + N_{\mathrm{He\,I}}\sigma_{\mathrm{He\,I}}(\nu) + N_{\mathrm{He\,II}}\sigma_{\mathrm{He\,II}}(\nu) \tag{3.2}$$

is the optical depth of an absorber with H I column density $N_{\mathrm{H\,I}}$ at frequency ν. We adopt the shape and normalization of the $z \approx 2.5$ CDDF from Prochaska et al. (2014) and assume that the normalization evolves as $(1+z)^{2.5}$ to roughly match the measured redshift evolution of the H I effective optical depth (Becker et al., 2013). For He II-ionizing photons with $\nu > 4\,\nu_{\mathrm{H\,I}} = \nu_{\mathrm{He\,II}}$, the opacity of an individual absorber is dominated by its He II content, which depends on the ratio of the H I and He II ionization rates ($\Gamma_{\mathrm{H\,I}}$, $\Gamma_{\mathrm{He\,II}}$). In the optically thin limit, $N_{\mathrm{He\,II}}$ can be related to $N_{\mathrm{H\,I}}$ by the parameter η_{thin},

$$\eta_{\mathrm{thin}} \equiv \frac{N_{\mathrm{He\,II}}}{N_{\mathrm{H\,I}}} = \frac{\Gamma_{\mathrm{H\,I}}}{\Gamma_{\mathrm{He\,II}}} \frac{\alpha^A_{\mathrm{He\,II}}}{\alpha^A_{\mathrm{H\,I}}} \frac{Y}{4X}, \tag{3.3}$$

where $\alpha^A_{\mathrm{H\,I}}$ and $\alpha^A_{\mathrm{He\,II}}$ are the case-A recombination coefficients of H I and He II, and X and Y are the hydrogen and helium mass fractions, respectively. For optically thick absorbers, the relationship is more complicated due to self-shielding of He II and H I ionizing photons. Modern cosmological radiative transfer models (e.g. Faucher-Giguère et al. 2009; Haardt & Madau 2012) determine $\eta(N_{\mathrm{H\,I}})$ by computing simplified radiative transfer of the UVB assuming a slab geometry and Jeans ansatz for absorbers (Schaye, 2001). Because of the implied dependence of absorber properties on $\Gamma_{\mathrm{He\,II}}$, UVB calculations must iterate several times to achieve self-consistency between the radiation field and the He II absorber distri-

bution. This link between $\Gamma_{\rm He\,II}$ and absorbers leads to an enhanced sensitivity of $\Gamma_{\rm He\,II}$ to evolution in the emissivity of ionizing photons (DF14; see also McQuinn et al. 2011).

In DF14, we extended this idea to link the *local* opacity of the IGM to the *local* $\Gamma_{\rm He\,II}$, which fluctuates significantly due to the rarity of the dominant sources of He II-ionizing photons (Furlanetto, 2009). In effect, this means that the mean free path of ionizing photons λ fluctuates along with the intensity of the ionizing background. We showed that if ionizing photons sample the distribution of ionization rates $f(\Gamma)$, the overall opacity of the IGM increases due to the skewed nature of the distribution. However, naive application of this effect to a one-dimensional cosmological radiative transfer model caused the UVB to vanish at all redshifts unless a somewhat ad-hoc correction due to proximity effects was applied. Such a one-dimensional model also cannot account for spatial coherence of ionizing background fluctuations on large scales. These limitations suggest that a one-dimensional model is insufficient to study the effect of opacity fluctuations on the He II ionizing background, motivating the three-dimensional approach described in the following section.

In this work, we apply the Faucher-Giguère et al. (2009) model for $\eta(N_{\rm H\,I})$ to compute $d\bar{\tau}/dz$ as a function of the *local* intensity of the He II-ionizing background. This procedure assumes that the He II fraction in the absorbers responds instantaneously to changes in $\Gamma_{\rm He\,II}$. In reality, the He II fraction will change on a characteristic timescale $t_{\rm eq} = (\Gamma_{\rm He\,II} + \alpha_{\rm He\,II} n_e)^{-1} \sim 10(\Gamma_{\rm He\,II}/10^{-14.5})^{-1}$ Myr. If the average quasar lifetime is shorter than this timescale then non-equilibrium ionization effects could be very important. All other analytic treatments of the He II-ionizing background have made the same assumption with respect to the absorbers of He II-ionizing photons (e.g. Fardal et al. 1998; Faucher-Giguère et al. 2009; Haardt & Madau 2012.

3.3 Numerical Model of the He II Ionizing Background

In this work, we present a simple three-dimensional extension to the 1D model of DF14. The basic structure of the model is as follows. Quasars are randomly placed in a cosmological volume 500 cMpc on a side from $z = 4$ to $z = 2.5$ following the Hopkins et al. (2007) B-band

quasar luminosity function (QLF). By placing quasars randomly we neglect their clustering; the effect of quasar clustering on fluctuations in the ionizing background is likely small (Dixon et al., 2014) but could play a role when the mean free path is very short (Desjacques et al. 2014; see Section 3.5.1). The ionizing spectrum of each quasar is determined by first converting the B-band luminosity to the luminosity at the H I ionizing edge with the constant conversion factor from Hopkins et al. (2007) and assuming that the spectrum at $\nu > \nu_{\rm H\,I}$ is a power law $L_\nu \propto \nu^{-\alpha_{\rm Q}}$ with $\alpha_{\rm Q} = 1.6$ in agreement with Telfer et al. (2002) and consistent with the most recent estimate by Lusso et al. (2015). We assume isotropic emission of ionizing radiation and a "lightbulb" model for quasar light curves with a lifetime of 50 Myr, similar to Compostella et al. (2013, 2014). The ionizing background due to these quasars is then calculated at all points on a 50^3 grid, giving a spatial resolution of 10 cMpc. This resolution is sufficient because the fluctuations in the ionizing background that we hope to characterize will only manifest on scales larger than the typical mean free path inside the simulation volume ($\gtrsim 30$ Mpc). Additionally, the simplified absorber physics from Section 2 is likely only a reasonable description on large-scales, so higher resolution would not add to our understanding.

The specific intensity of ionizing radiation J_ν at each point $\vec{r}$ on the grid is computed by adding together the contribution from every quasar i with specific luminosity $L_i(\nu)$ at position $\vec{r}_i$ that is turned on at time $t - |\vec{r} - \vec{r}_i|/c$,

$$J_\nu(\vec{r}, t) = \sum_i \frac{L_i(\nu) e^{-\tau(\vec{r}, \vec{r}_i, \nu)}}{(4\pi|\vec{r} - \vec{r}_i|)^2}, \tag{3.4}$$

where the optical depth of ionizing radiation from the quasar $\tau(\vec{r}, \vec{r}_i, \nu)$, which in previous work has been approximated as $\sim |\vec{r} - \vec{r}_i|/\lambda_{\rm mfp}$, is computed by integrating the fluctuating IGM opacity along the light cone,

$$\tau(\vec{r}, \vec{r}_i, \nu) = \int_{\vec{r}_i}^{\vec{r}} \frac{d\tau}{dz} \frac{dz}{dl} dr', \tag{3.5}$$

where $d\tau/dz$ is given by equation (1) evaluated at the redshift corresponding to $t' = t - |\vec{r}' - \vec{r}|/c$, and which depends on the local ionization rate $\Gamma_{\rm He\,II}(\vec{r}', t')$ through the absorber model

discussed in Section 2. The ionization rate is then computed by integrating over frequency,

$$\Gamma_{\mathrm{He\,II}}(\vec{r},t) = 4\pi \int_{\nu_{\mathrm{He\,II}}}^{\infty} \frac{J_\nu(\vec{r},t)}{h\nu} \sigma_{\mathrm{He\,II}}(\nu) d\nu, \tag{3.6}$$

where in practice this integral is computed discretely with 12 logarithmic bins in ν from $\nu_{\mathrm{He\,II}}$ to $10^{1.2}\nu_{\mathrm{He\,II}}$. We neglect the redshifting of photons as they travel from the quasar to the cell and use the proper distance to the source rather than the luminosity distance when computing J_ν, but these should be relatively small effects. Because the opacity between the cell and the quasar depends on the *history* of the opacity between the source and cell, a fully self-consistent model requires a time-dependent fluctuating background.

Because the IGM opacity depends on the local value of $\Gamma_{\mathrm{He\,II}}$, which in turn depends on the opacity, as discussed in Section 3.2, the calculation must be iterated in order to achieve self-consistency. We iterate until the average change of $\Gamma_{\mathrm{He\,II}}(\vec{r},t)$ across all grid cells between iterations is less than 1% at $z = 3$, which typically requires 7–8 iterations.

We have additionally run a "control" simulation that ignores spatial fluctuations in the mean free path. Instead, $d\tau/dz$ is spatially uniform and computed as a function of redshift from a standard 1D ionizing background model with the same input parameters (i.e. quasar emissivity, CDDF). The rest of the computation is done in a similar manner to the full model described above, including finite quasar lifetimes and light cone effects. We will refer the this model as the "uniform MFP" model in the rest of the paper.

3.3.1 Results

The solid curves in Figure 3.1 show the evolution of the distribution of ionization rates, $f(\Gamma)$, from the simulation volume at $z = 3.1$–2.5 in steps of $dz = 0.2$. The dotted curves show the distributions for the uniform MFP model, which are nearly identical to analytic models for $f(\Gamma)$ computed using the same mean free path (Meiksin & White, 2003; Furlanetto, 2009). The distributions in the full simulation are broader than the uniform MFP model due to the enhancement of large-scale features in the radiation field by the fluctuating mean free path, and the disagreement increases with increasing redshift as the mean free path fluctuations become more pronounced.

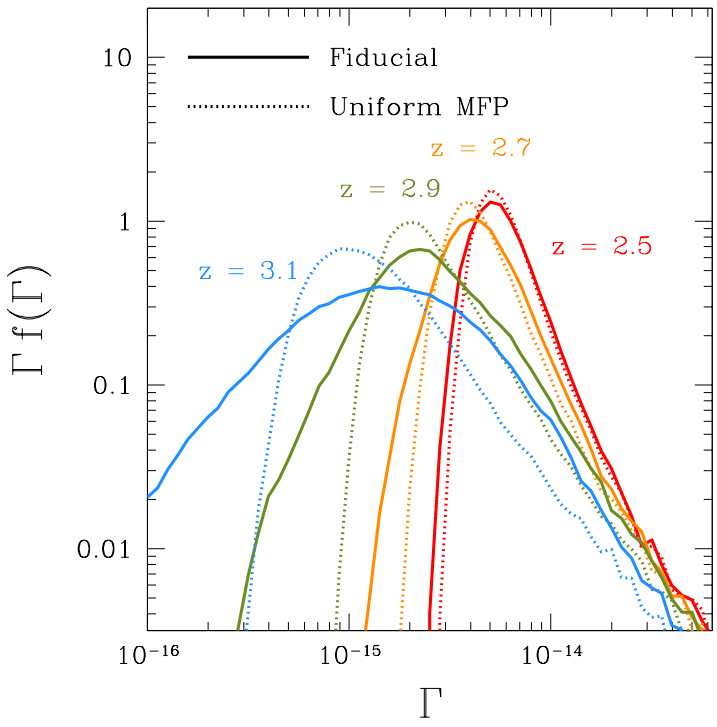

Figure 3.1: The solid curves show $\Gamma f(\Gamma)$ from the fiducial ionizing background simulation for $z = (2.5, 2.7, 2.9, 3.1)$ from right to left. The dotted curves show the distributions from the uniform MFP model at the same redshifts. The differences between the two sets therefore demonstrate the effect of mean free path fluctuations.

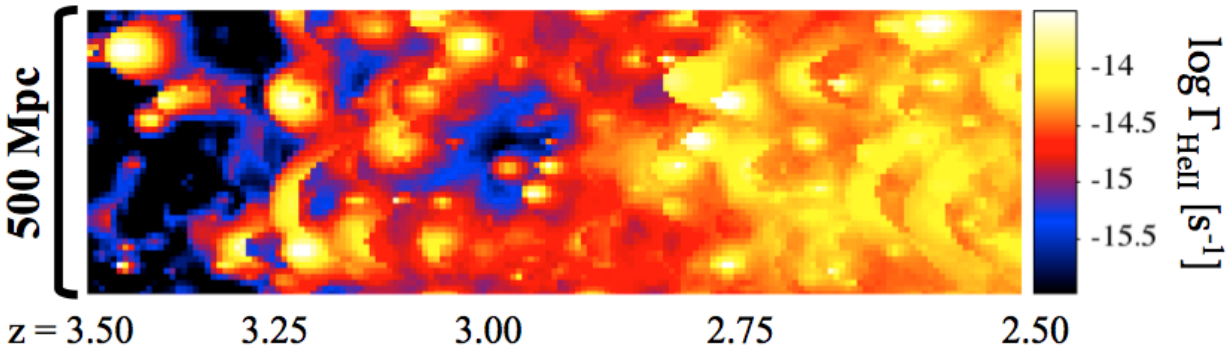

Figure 3.2: Light cone projection of $\Gamma_{\rm He\,II}$ from $z = 3.5$–2.5 in the fiducial fluctuating mean free path simulation. The vertical axis is position on the sky, and the horizontal axis is distance along the light cone with the observer located to the right. The parabolic features are due to the intersection of the light cone with a nearby bright quasar, though the exact geometry depends on the transverse distance. Large-scale correlations are seen along the light cone due to the coherence of ionization structures in the fluctuating mean free path model.

The evolution of fluctuations in the helium-ionizing background is shown visually in Figure 3.2 as a light cone projection from $z = 3.5$–2.5. The parabolic features are caused by the intersection of the light cone with the expanding 50 Mly-thick "light shell" from a particularly bright quasar near the sightline (similar to Figure 5 in Croft 2004). At high redshift, the mean background is dominated by the relatively transparent proximity zones around luminous quasars. By $z \sim 2.5$, the mean free path is $\gtrsim 100$ Mpc, leading to modest background fluctuations of about a factor of two that are similar to observations (McQuinn & Worseck, 2014). Figure 3.3 shows a series of snapshots of a slice through the simulation volume, with Γ from the uniform and fluctuating mean free path models and maps of the logarithmic difference between the two. The dominant features change from transparent proximity zones at $z > 3$ (top row) to large-scale (~ 200 Mpc) coherent structures at $z \sim 2.9$ (middle row) before finally the ionizing background becomes mostly uniform and unaffected by mean free path fluctuations at $z < 2.7$ (bottom row). At early times, the fluctuating model has substantial differences from the uniform model principally because the mean free path is substantially larger near the bright sources, leading to larger proximity zones (or

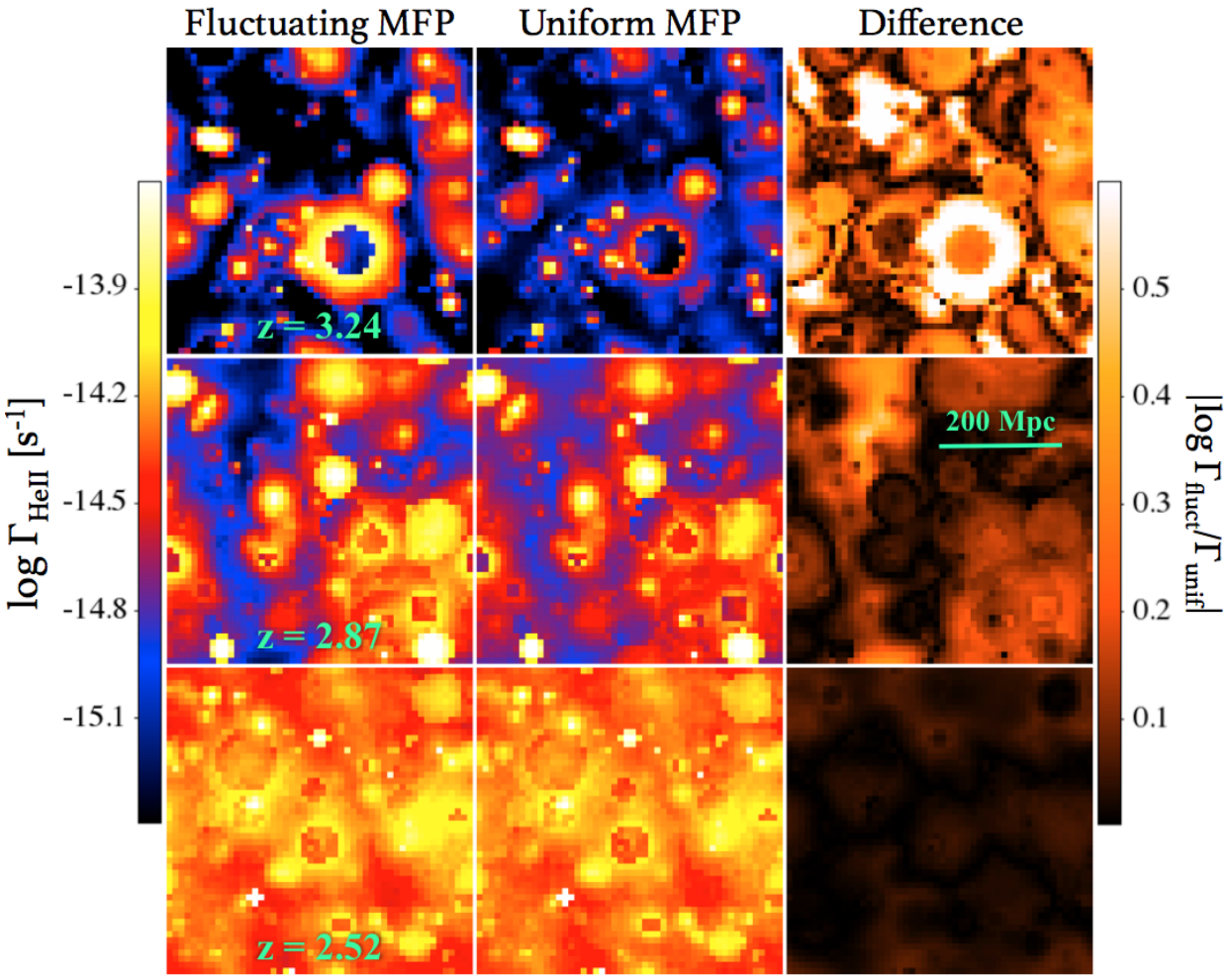

Figure 3.3: Slices of the simulation volume at $z = 3.24$, 2.87, 2.52 from top to bottom. The left and middle panels show the He II ionization rate from the fluctuating and uniform mean free path simulations, respectively. The right panel shows the difference between the two, expressed as the "distance" between the models in log space. The ionizing background becomes significantly more uniform over time and as a result the effect of including a fluctuating mean free path decreases. The topology of the fiducial model evolves from proximity-zone dominated at $z \gtrsim 3$ (top), to highly fluctuating at $2.7 \lesssim z \lesssim 3.0$ with large-scale correlations (middle), to mostly uniform at $z \lesssim 2.7$ (bottom).

"fossils" once the quasar has turned off), and deeper opacity far from those sources where the mean free path becomes very small. At later times ($z = 2.87$ in Figure 3.3), the amplitude of these effects decreases, but their large-scale coherence remains, thanks to the rarity of the sources.

From Figure 3.1 we see that the high-Γ end of $f(\Gamma)$ ($\log\Gamma \gtrsim -13.8$) changes very little with redshift. These high-Γ regions typically lie in the *transparent* proximity zones of bright quasars (DF14), which do not evolve significantly because they are largely decoupled from the global ionizing background evolution (i.e. the *local* mean free path is long enough that $\Gamma(r) \propto r^{-2}$ is a good approximation). The small variation with redshift that remains depends on both the evolution of the QLF and Poisson fluctuations in the number of extremely luminous quasars present in the simulation volume at any given time.

3.4 Predictions for the He II Lyα Forest

The primary observable of He II is the opacity of the He II Lyα forest ($\lambda_{\rm rest} < 304$ Å) in far-ultraviolet spectra of $z \sim 3$–4 quasars. In this section we describe a simple model of mock He II Lyα transmission spectra through the fluctuating ionizing background computed in the previous section.

The foundation of our mock spectrum model is a Monte Carlo realization of absorbers drawn from the observed CDDF, computed in a manner similar to Worseck & Prochaska (2011). We draw H I absorbers in the range $10^{11.3} < N_{\rm H\,I} < 10^{19}$ cm^{-2} from the same evolving CDDF used in Sections 3.2 and 3.3 to compute the ionizing continuum opacity and place them randomly along a sightline. The He II content of each absorber is computed as in Section 3.2, assuming a constant uniform $\Gamma_{\rm H\,I} = 10^{-12}$ s^{-1} (Becker & Bolton, 2013) and $\Gamma_{\rm He\,II}$ extracted along the light cone from the fluctuating He II ionizing background simulation. Doppler widths for each absorber are drawn in the range $10 < b < 100$ km/s from the distribution function $dN/db \propto b^{-5} \exp -b_\sigma^4/b^4$ (Hui & Rutledge, 1999) with $b_\sigma = 24$ km/s (Kim et al., 2001), and we assume that $b_{\rm H\,I} = b_{\rm He\,II}$ (velocity-broadening dominated). Finally, we compute transmission spectra assuming Voigt profiles for each absorber using the

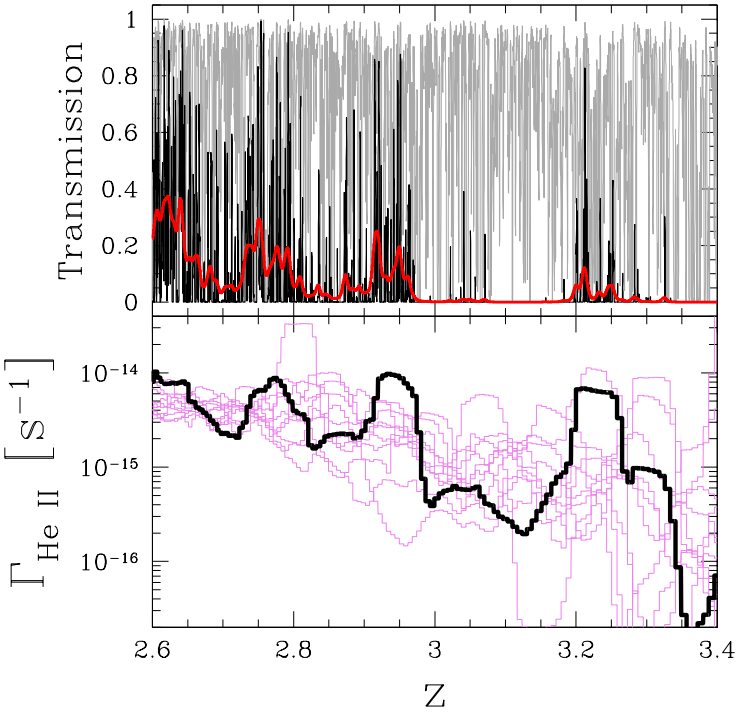

Figure 3.4: Top panel: Mock He II Lyα forest (black) and H I forest (grey) transmission spectrum for a single light cone sightline. Both transmission spectra are shown at the arbitrarily high resolution of our simulations and do not include instrumental smoothing or noise. In particular, the narrow transmission spikes seen in the model He II Lyα forest spectrum no longer exist when smoothed to mimic the resolution of HST/COS G140L, shown by the red curve. Bottom panel: $\Gamma_{\rm He\,II}$ along the same sightline (thick curve) along with ten other random sightlines (thin curves). Large-scale features in the He II Lyα transmission are due to variations in $\Gamma_{\rm He\,II}$ that are enhanced in the fluctuating mean free path model.

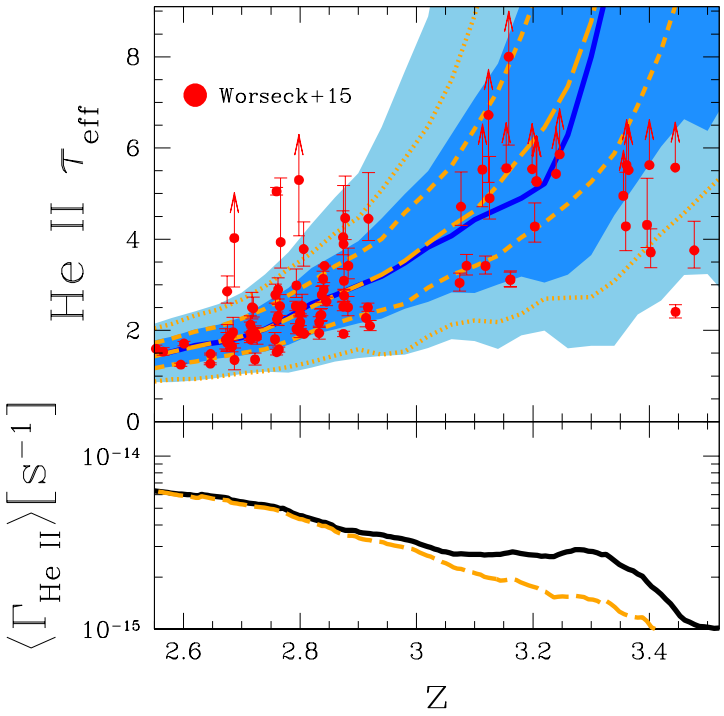

Figure 3.5: Top: Evolution of the He II effective optical depth in $\Delta z = 0.04$ (≈ 40 cMpc) bins. The solid curve shows the median He II $\tau_{\rm eff}$ in our fiducial (500 cMpc)^3 ionizing background simulation, and the dark and light shaded regions show ± 1 and 2σ variations, respectively. Long-dashed, dashed, and dotted curves show the median optical depth and $\pm 1, 2\sigma$ variations for the uniform MFP model (see text) normalized slightly to match the fiducial simulation at $z \sim 2.5$. The red data points are the $\Delta z = 0.04$ measurements by Worseck et al. (2014a) with small Δz offsets for clarity. Bottom: The solid curve shows the evolution of the mean $\Gamma_{\rm He\,II}$ in the simulation. At $z \gtrsim 3.2$, the mean $\Gamma_{\rm He\,II}$ is sensitive to the number of extremely luminous quasars present at any given time due to the transparent proximity effect and thus shows substantial stochastic variations. The long-dashed curve is the mean $\Gamma_{\rm He\,II}$ in the uniform MFP model, increased by $\sim 7\%$ to match the fiducial model at $z \sim 2.5$.

efficient approximation of Tepper-García (2006). An example He II (black) and H I (grey) transmission spectrum is shown in the top panel of Figure 3.4. The transmission through the He II forest is closely tied to the variations in $\Gamma_{\rm He\,II}$ along the sightline, shown in the bottom panel. Large-scale regions along the light cone with enhanced $\Gamma_{\rm He\,II}$ are apparent, which share a characteristic width corresponding to our chosen quasar lifetime.

We then binned mock spectra from 3000 randomly directed sightlines into $\Delta z = 0.04$ pieces to allow direct comparison to the observations of Worseck et al. (2014a). We compute the effective optical depth of each bin as $\tau_{\rm eff} = -\ln(\sum T_i/N)$ where T_i is the transmission in each of the N pixels inside the bin. The solid curve in Figure 3.5 shows the evolution of the median effective optical depth in the full simulation. The median optical depth increases steadily from $\tau_{\rm eff} \sim 2$ at $z \sim 2.7$ to $\tau_{\rm eff} \sim 5$ by $z \sim 3.1$, similar to the observations by Worseck et al. (2014a). The dark and light shaded regions in Figure 3.5 show the ± 1 and 2σ range of $\tau_{\rm eff}$ values. Across the entire redshift range the low-τ end of the distribution, corresponding to regions with high $\Gamma_{\rm He\,II}$, evolves slowly. In contrast, the high-τ end, corresponding to regions with low $\Gamma_{\rm He\,II}$, increases rapidly above $z \sim 2.8$.

The thin dashed and dotted curves in Figure 3.5 show the median and distributions of the uniform MFP simulation, re-normalized slightly to match the median optical depth at $z = 2.55$. The median τ of the uniform MFP simulation is very similar to the full model, but the distribution tends to be more narrow. Fluctuations in the mean free path are most important in the tails of the distribution, as seen by the growing 2σ width at $z \gtrsim 2.8$. DF14 predicted that the evolution of Γ should be accelerated by including fluctuations in the mean free path because the IGM opacity increases when averaged over $f(\Gamma)$. Instead, in our 3D model the evolution of Γ from the uniform MFP model is strikingly similar to the fluctuating MFP model at $z \lesssim 3$. This is likely due to the fact that ionizing photons are preferentially emitted from bright quasars with transparent proximity zones, so the distribution of Γ seen by ionizing photons is biased towards higher values.

The mock distribution is similar to the observations in Worseck et al. (2014a) (red points), with the exception of a handful of high-$\tau_{\rm eff}$ regions at $z \sim 2.75$ and a very low $\tau_{\rm eff}$ region at $z = 3.44$. In particular, the well-measured $\tau_{\rm eff} \sim 5$ region seen towards HE2347-4342 is

quite rare in our simulations, appearing only in $\sim 0.1\%$ of sightlines. There is some evidence for disagreement at $z \sim 3.4$ – our model predicts that only $\sim$ 1–2/10 $\Delta z = 0.04$ segments should show detectable transmission (i.e. $\tau_{\rm eff} \lesssim 5.5$) while the observed fraction is 5/10. We leave a full statistical comparison of our modeled optical depth distributions to observations to future work.

The upper and lower bounds to the $\tau_{\rm eff}$ distribution are driven by the volume of space far away from (i.e. $\tau(\vec{r}, \vec{r}_{\rm Q}, \nu_{\rm He\,II}) > 1$) and very close to luminous quasars, respectively. The former evolves very quickly with redshift – not only is the number density of luminous quasars decreasing above $z \sim 2.5$, but more importantly the mean free path also decreases very rapidly. Additionally, as one moves further away from luminous sources in real space, the weaker ionizing background causes the mean free path to shrink, causing a non-linear increase in the optical depth. The lower bound to the $\tau_{\rm eff}$ distribution evolves only due to the evolution of the bright end of the QLF, with some fluctuations due to Poisson variance in the number of very luminous quasars – the "bumpy" evolution in our model is due to this variance rather than poor sampling of the $\tau_{\rm eff}$ distribution.

Our model allows a considerable amount of "tuning" of parameters to reproduce the smoothly evolving median $\tau_{\rm eff}$ at $z \lesssim 3$, namely through the emissivity of He II-ionizing photons (via the quasar spectral index $\alpha_{\rm Q}$), the ionization state of H I absorbers (via $\Gamma_{\rm H\,I}$), and the exact form of the CDDF (via the shape, normalization, and minimum $N_{\rm H\,I}$). It is actually a remarkable coincidence that – without deliberate tuning – our fiducial set of model parameters provides good agreement to the He II $\tau_{\rm eff}$. We discuss the effect of variations in model parameters further in Section 3.5.

In Figure 3.6 we compare the associated H I and He II $\tau_{\rm eff}$ on scales of $\Delta z = 0.01$ (≈ 10 cMpc) for comparison to Figure 8 of Worseck et al. (2014a). This scale is also coincidentally the spatial resolution of our simulations, and thus the smallest scale that we can make predictions for variations in $\tau_{\rm eff}$ due to the fluctuating ionizing background. The behavior of the median optical depth is very similar to that of the Worseck et al. (2014a) data at all redshifts. However, at $z \sim 2.85$ our simulations fail to reproduce the substantial observed fraction of regions with $\tau_{\rm H\,I} \lesssim 0.5$ and $\tau_{\rm He\,II} \gtrsim 6$. At these scales, the correlation between

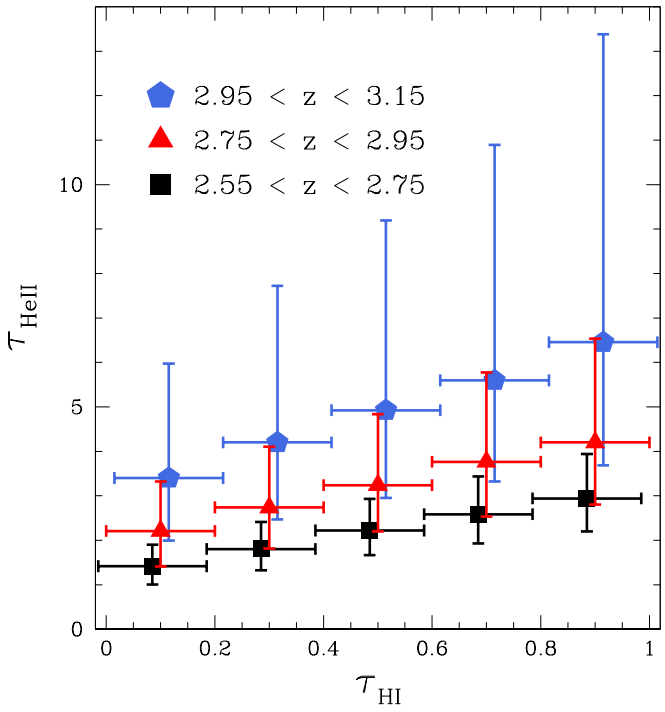

Figure 3.6: Distribution of He II optical depths at $\Delta z = 0.01$ scales, roughly corresponding to the spatial resolution of our ionizing background model, as a function of H I optical depth. The black squares, red triangles, and blue pentagons show the median $\tau_{\rm He\,II}$ in bins of $\Delta\tau_{\rm H\,I} = 0.2$ for $z \sim 2.65$, 2.85, and 3.05, respectively. Error bars show the 1σ dispersion in $\tau_{\rm He\,II}$ within each bin. The points and H I ranges have been shifted slightly between the redshift ranges for clarity. Compare to Figure 8 of Worseck et al. (2014a).

absorber systems and quasars, which we explicitly ignore, likely plays an important role in the distribution of effective optical depths. Nevertheless, the agreement of our median relationship between H I and He II suggests that our modeling approach is not an entirely unreasonable one. It is worth noting that for $z \gtrsim 3$ a large fraction of sightlines have little-to-no detectable flux given current observational limitations, so judging the agreement between our simulation and observations is difficult.

3.5 Model Uncertainties

We have shown that a relatively simple model of fluctuations in the helium ionizing background can reproduce most of the observed properties of the He II Lyα forest across cosmic time. This implies that fluctuations in the radiation field should be considered a viable alternative to ongoing He II reionization (e.g. Worseck et al. 2011) as an explanation of the observed $\tau_{\rm eff}$ variations, at least for $z \lesssim 3.2$. We discuss some important caveats to our simple model assumptions below.

3.5.1 Caveats

(i) He II Lyα forest prescription

Our model assumes that the He II Lyα forest can be described as an ensemble of randomly distributed absorbers following the Prochaska et al. (2014) CDDF. While this kind of description has been successfully used to model the H I effective optical depth in previous work (e.g. Haardt & Madau 2012), He II effective optical depths greater than ~ 2.0 at $z \lesssim 3$ require near-complete blanketing of the spectrum by numerous low $N_{\rm H\,I}$ ($\lesssim 10^{12}$ cm^{-2}) lines (Fardal et al., 1998). The abundance of such "absorbers" are completely unconstrained by observations, and physical interpretation via the Jeans ansatz (Schaye, 2001) becomes unrealistic with implied absorber sizes of $\gtrsim 2$ cMpc. In effect, these lines act as a "smooth" component to the He II Lyα absorption that is required to reproduce the observed $\tau_{\rm eff} \gtrsim 1.5$ absorption. Our treatment of the He II Lyα forest as a set of discrete absorption lines is a rough approximation, with the low $N_{\rm H\,I}$ systems representing the smooth low density envi-

ronments of cosmic voids that provide the majority of the He II Lyα opacity (Croft et al., 1997).

(ii) Ionization equilibrium

Our simulations assume that the universe is in ionization equilibrium – that is, reionization is assumed to have completed some time in the past. Assuming the gas density probability distribution from Miralda-Escudé et al. (2000) and following their procedure to compute the neutral fraction of the IGM, the equilibrium He II fraction in our simulation is below 1% by volume at $z \lesssim 3$. For the lowest $\Gamma_{\rm He\,II}$ regions at $z \sim 3$ the equilibrium He II fraction can be as high as $\sim 10\%$, so an equilibrium treatment is unlikely to be very accurate. This is the primary weakness of our model compared to full radiative transfer simulations (e.g. McQuinn et al. 2009; Compostella et al. 2013, 2014).

(iii) Clustering of sources and absorbers

In both the source and absorber models we neglect the effect of clustering. As mentioned previously, Dixon et al. (2014) showed that the impact of quasar clustering on ionizing background fluctuations was likely small. Recent work by Desjacques et al. (2014) suggests that clustering could have a significant effect on background fluctuations at $z \sim 3$ if the mean free path is comparable to the correlation length of quasars, $r_\xi \sim 15$ Mpc. The average mean free path in our simulations is substantially larger than this for the redshifts we are interested in ($\lambda_{\rm mfp} \gtrsim 30$ Mpc), but it is likely that the addition of mean free path fluctuations would enhance the effect of clustering to some degree, and we will investigate this in future work. In constructing our mock Lyα forest spectra the only large-scale fluctuations in the density field we consider are the Poisson variations in the number of absorber systems, which are expected to be fairly small (Fardal et al., 1998). Cosmic variance in the large-scale density field at the $\Delta z = 0.04 \approx 40$ cMpc scale considered in this work should also be small compared to the fluctuations in the ionizing background, with $\sigma(R = 40\,{\rm cMpc}) \sim 0.1$. While the overall effect of clustering may be small, its largest effect would likely be to extend the tails of the $\tau_{\rm eff}$ distribution, which could ease some tension with the highest $\tau_{\rm eff}$ regions at $z \sim 2.8$.

(iv) Cosmic variance

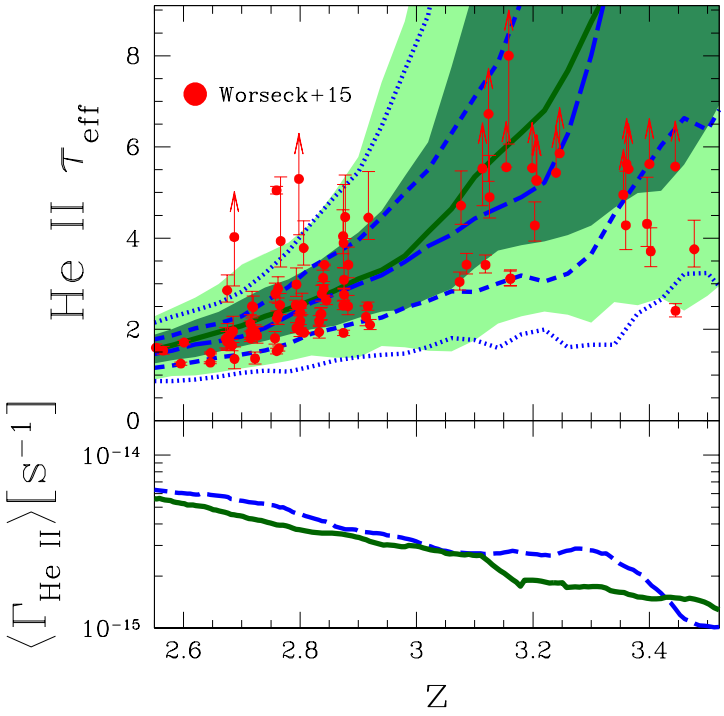

Figure 3.7: Top: Comparison of He II effective optical depth in $\Delta z = 0.04(\approx 40$ cMpc) bins between our fiducial simulation and a similar simulation with a different random seed. The solid curve shows the median He II $\tau_{\rm eff}$ in the second simulation, and the dark and light shaded regions show ± 1 and 2σ variations, respectively. The dashed and dotted curves show the effective optical depth distributions from the fiducial simulation in Figure 3.5. Bottom: Evolution of the mean $\Gamma_{\rm He\,II}$ in the fiducial and secondary simulations. Small random differences in the emissivity evolution result in a systematically lower $\Gamma_{\rm He\,II}$ in the secondary simulation.

Despite the large volume probed by our simulations, the mean optical depth and fluctuations that we measure are still affected somewhat by cosmic variance. The non-linear response of the ionizing background due to mean free path fluctuations implies that a random upward boost in the number of bright quasars leads to large-scale regions with larger-than-average mean free path that persist until the radiation from those quasars leaves the simulation volume. This can be seen in our fiducial simulation which has a pair of $\sim 70 L_*$ quasars turn on at $z \sim 3.4$. The "boost" in $\Gamma_{\rm He\,II}$ and scatter of optical depths to low values from $z \sim 3.2$–3.4 seen in Figure 3.5 is almost entirely attributable to these two sources. This demonstrates the sensitivity of our model to the number of brightest sources, at least at early times when the average mean free path is small. We show the results of a secondary simulation with the same input parameters, but a different random seed for generating quasars, in Figure 3.7. In this secondary simulation, the emissivity is on average somewhat smaller than the fiducial simulation, causing the overall mean $\Gamma_{\rm He\,II}$ to be smaller at all times. The variance we see suggests that simulations hoping to fully characterize the helium-ionizing background following He II reionization must be extremely large (> 500 cMpc on a side) to be accurate at the $\sim 10\%$ level. Achieving accurate radiative transfer in such large volumes will require substantial computational resources, far more than our simplified approach.

3.5.2 Variations in Model Parameters

The primary input parameters to our model are: the quasar ionizing spectral index $\alpha_{\rm Q}$, the strength of the H I-ionizing background $\Gamma_{\rm H\,I}$, the column density distribution of H I absorbers $f(N_{\rm H\,I}, z)$, and the quasar lifetime $t_{\rm Q}$. We leave a full analysis of variations in these parameters to future work, but we qualitatively describe their effects and importance below.

The primary effect of adjusting $\alpha_{\rm Q}$ is on the normalization of the quasar ionizing output at $\nu_{\rm He\,II}$, because $L_{\rm He\,II} = 4^{-\alpha_{\rm Q}} L_{\rm H\,I}$. At fixed redshift, due to the self-consistency of absorbers with the ionizing background, the average ionization rate should roughly follow $\Gamma_{\rm He\,II} \propto \epsilon^{1/(2-\beta)}$ (McQuinn et al., 2011), where β is the power law index of the CDDF in absorbers

with He II ionizing opacity $\tau_{\nu,\mathrm{He\,II}} \lesssim 1$ ($N_{\mathrm{H\,I}} \lesssim 10^{15.5}$ cm^{-2}). In the Prochaska et al. (2014) CDDF model that we adopt, $\beta = 1.6$–1.75 in the relevant range of column densities, so we expect $\Gamma_{\mathrm{He\,II}} \propto \epsilon^{2.5-4.0} \propto 4^{-(2.5-4.0)\alpha_{\mathrm{Q}}}$. In practice, we find that $\Gamma_{\mathrm{He\,II}} \propto \epsilon^{2.5}$, so an adjustment of α_{Q} by 0.1 results in a change of $\Gamma_{\mathrm{He\,II}}$ by a factor of ~ 1.4. This sensitivity is completely degenerate with any other adjustment in the ionizing emissivity, such as the conflict between the typical conversion of the Hopkins et al. (2007) rest-frame optical QLF and the UV luminosity density measured by Cowie et al. (2009). Changing the shape of the He II-ionizing spectrum alone leads to a minor adjustment of the relationship between $\Gamma_{\mathrm{He\,II}}$ and the mean free path of average-energy ionizing photons that regulates the fluctuations in the background, so a harder spectrum would result in weaker fluctuations and a softer spectrum would lead to stronger fluctuations at fixed $\langle\Gamma_{\mathrm{He\,II}}\rangle$

In our model, $\Gamma_{\mathrm{H\,I}}$ is fixed at a constant value, consistent with measurements by Becker & Bolton (2013). Because $\lambda_{\mathrm{mfp}} \propto \eta^{-1} \propto \Gamma_{\mathrm{H\,I}}$, adjusting $\Gamma_{\mathrm{H\,I}}$ is roughly equivalent to changing the normalization of the mean free path at fixed $\Gamma_{\mathrm{He\,II}}$. In effect, we find that $\Gamma_{\mathrm{He\,II}} \propto \Gamma_{\mathrm{H\,I}}^{-1}$, so for a given absorber in our He II Lyα forest model, $N_{\mathrm{He\,II}} \propto \Gamma_{\mathrm{H\,I}}^{-2}$, and so very roughly $\tau_{\mathrm{eff}} \propto \Gamma_{\mathrm{H\,I}}^{-2}$. If one assumed a smaller $\Gamma_{\mathrm{H\,I}}$ (e.g. Faucher-Giguère et al. 2009), a simple way to maintain the same τ_{eff} would be to increase the He II-ionizing emissivity such that η remained constant, or in other words, $\Delta \log \Gamma_{\mathrm{He\,II}} \sim 2 \times \Delta \log \Gamma_{\mathrm{H\,I}}$.

The redshift evolution of the mean free path and the details of its dependence on the local background are sensitive to the evolution and shape of the CDDF. The CDDF of H I absorbers has been well-measured at $z \sim 2.5$, but discrepancies between different works exist in the difficult (i.e. saturated) $N_{\mathrm{H\,I}}$ regime that is most important to cosmological He II radiative transfer ($N_{\mathrm{H\,I}} \sim 10^{15}$–$10^{16}$ cm^{-2}; see, e.g., Kim et al. 2013; Rudie et al. 2013; Prochaska et al. 2014). While recent observations have greatly increased our knowledge of the CDDF at $z \sim 2.5$, the *evolution* of both the shape and normalization of the CDDF are still very uncertain.The effects of different CDDF parameterizations on the evolution of the He II-ionizing background are discussed in detail in DF14.

In our model we assume that quasars emit ionizing photons isotropically at a fixed rate for a fixed lifetime of 50 Myr and fixed spectral index α_{Q}. This is an enormously simpli-

fied picture of quasars that ignores realistic light curves (e.g. Hopkins & Hernquist 2009), anisotropic/beamed emission, and variations in the ionizing spectral index (Vanden Berk et al., 2001; Telfer et al., 2002). We tested small volume simulations with 25 and 100 Myr and found that the main results of this work, the distribution of $\tau_{\rm eff}$ over $dz = 0.04$, were qualitatively unchanged. The primary difference was in the characteristic width of features in $\Gamma_{\rm He\,II}$ along the light cone, as seen in Figures 3.2 and 3.4. If quasar lifetimes are significantly shorter than the time corresponding to $dz = 0.04$, the blending of features would likely reduce the amount of fluctuations observed. However, on those short time scales ($\Delta t \lesssim 10$ Myr), the equilibration time of the gas (Section 3.2) would become comparable to the quasar lifetime.

Given the number of uncertain parameters in modeling both the sources and absorbers, there are important degeneracies in our model. For example, for a fixed CDDF and model of the physical nature of absorbers, the measured average He II $\tau_{\rm eff}$ corresponds to a locus of reasonable combinations of the He II-ionizing emissivity and $\Gamma_{\rm H\,I}$. In that sense, the matching of our fiducial model to the $z \sim 2.5$ measurements of the He II $\tau_{\rm eff}$ is something of a coincidence – other "solutions" exist in a reasonable range of parameter space. However, our results show that a self-consistent model of the He II-ionizing background, with parameters consistent with other measurements, is compatible with the vast majority of the forest observations. This conclusion does not result from a fortuitous choice of parameters but is true for a large swath of - though by no means the entirety of - parameter space.

3.6 Discussion & Conclusion

Recent observations of excursions to high effective optical depths in the He II Lyα forest at $z \lesssim 3$ have been interpreted as evidence for ongoing He II reionization (Shull et al., 2010; Worseck et al., 2011). We have shown that the majority of the $z \lesssim 3$ high-$\tau_{\rm eff}$ measurements can be explained by fluctuations in the ionizing background when mean free path fluctuations are included self-consistently. Our model consists of a 3D realization of randomly distributed quasars following the measured quasar luminosity function, with finite quasar

lifetimes and a finite speed of light. We additionally let the mean free path vary depending on the strength of the local ionizing background in a manner analogous to standard 1D cosmological radiative transfer models (Faucher-Giguère et al., 2009; Haardt & Madau, 2012) that assumes ionization equilibrium throughout the IGM.

The resulting radiation field fluctuates strongly on large scales, leading to large variations between sightlines. These large-scale features are due to the additional coherence caused by mean free path fluctuations, which are present even though we have neglected the clustering of sources. If bright sources randomly lie close to each other, the excess background is enhanced due to the locally transparent IGM. Similarly, regions that are far from bright sources suffer from a more opaque IGM, further decreasing the radiation they receive. The strength of these effects increase strongly with redshift, such that by $z \gtrsim 3.2$ they dominate the structure of the ionizing background (see the top panels of Figure 3.3). At these relatively high redshifts it is likely that the progression of He II reionization is important to the budget of He II-ionizing photons and the size of proximity zones, but it is currently unclear how to distinguish the two scenarios observationally. Despite the enhanced fluctuations of our model, a handful of observed regions with abnormally high optical depth at $z \sim 2.7$–2.9 are in modest tension with our model predictions, suggesting that we may still be missing an important piece of the puzzle.

In future work, we will increase the predictive power of our model in several ways while still maintaining the flexibility and efficiency of our simple basic method. Effects we have not considered explicitly in this work include: realistic quasar light curves (e.g. Hopkins & Hernquist 2009), variations in $\alpha_{\rm Q}$, quasar clustering, and anisotropic emission of ionizing radiation (i.e. beaming). We will also improve our model for the Lyα forest by applying our model radiation field to hydrodynamical simulations of the IGM. Finally, we will extend the applicability of our model to the He II reionization epoch by combining it with a semi-numerical reionization model (Dixon et al., 2014) for comparison to the highest redshift observations of the He II Lyα forest ($z \gtrsim 3.5$; Worseck et al. 2014a).

Our model may also have implications for fluctuations in the H I ionizing background. H I-ionizing sources, namely, star-forming galaxies, have very high space densities compared to

quasars, thus the common expectation is that the ionizing background should be completely uniform – indeed, uniform ionizing background models are sufficient to describe the well-characterized H I Lyα forest at $z \sim 2$–4 (Meiksin & White, 2004; Croft, 2004; Becker & Bolton, 2013; Becker et al., 2015). However, the mean free path to H I-ionizing photons drops steeply with redshift (Worseck et al., 2014b), such that at $z \gtrsim 5$, the *clustering* of galaxies is able to produce significant fluctuations in the ionizing background (Mesinger & Furlanetto, 2009). Ionizing background models that assume a uniform mean free path struggle to explain the substantial sightline-to-sightline variations in H I $\tau_{\rm eff}$ at large scales seen at $z \gtrsim 5.5$ (Becker et al., 2015), suggesting that either reionization has not yet completed or that fluctuations in the mean free path start to play a role (Davies & Furlanetto, in prep.).

The large-scale variations in the He II-ionizing background we have described here show that He II reionization is a rich and complex event. The interaction of the sources, IGM, and radiation field require careful modeling, which is made possible by our detailed understanding of the IGM at $z \sim 3$. Observers are discovering more and more lines of sight along which the He II Lyα forest can be studied, and the large fluctuations in our model imply that a full understanding of the reionization event will require exploring these new lines of sight in detail.

CHAPTER 4

Large-scale fluctuations in the hydrogen-ionizing background following the epoch of reionization

4.1 Introduction

The reionization of hydrogen was an important milestone in the history of the Universe, representing the culmination of early structure formation and a dramatic "phase change" in the intergalactic medium (IGM). Great efforts have been made to investigate the reionization epoch, both theoretically and observationally, as it provides a powerful tool for testing theories of the formation of the first galaxies.

One of the dominant features of neutral hydrogen is strong Lyman-series absorption. Observations of large-scale opaque regions in the Lyα forest of high-redshift quasars, also known as Gunn-Peterson troughs (Gunn & Peterson, 1965), have already placed intriguing constraints on the end stages of reionization (e.g. Fan et al. 2001, 2006; Mesinger 2010; McGreer et al. 2011, 2015). Searches for Lyα damping wing absorption due to the presence of a neutral IGM (Miralda-Escudé, 1998a) in high-redshift quasar spectra have been inconclusive (e.g. Mesinger & Haiman 2007; Mesinger & Furlanetto 2008b; Schroeder et al. 2013; Bolton & Viel 2011 but see Bosman & Becker 2015), but could eventually provide "smoking gun" evidence for primordial neutral material. Lyα damping wing absorption due to a neutral IGM may also be responsible for the precipitous drop in the fraction of star-forming galaxies that show strong Lyα emission lines above $z \sim 6$ (e.g. Stark et al. 2010; Ono et al. 2012; Schenker et al. 2014; Pentericci et al. 2014; Tilvi et al. 2014), subject to considerable model-dependent uncertainties due to the complexity of Lyα emission and scattering processes and the inhomogeneous reionization process (e.g. McQuinn et al. 2007b; Mesinger & Furlanetto

2008a; Dijkstra et al. 2011; Bolton & Haehnelt 2013; Choudhury et al. 2014; Mesinger et al. 2015).

The ionization state of gas in the IGM is regulated by the "ionizing background", the extragalactic ionizing radiation field. The ionizing background is comprised of ionizing photons emitted by young stars and quasars, filtered by neutral gas structures that set an average attenuation length or mean free path λ (e.g. Haardt & Madau 1996, 2012; Faucher-Giguère et al. 2009). Interpretation of Lyα forest observations typically assumes a constant hydrogen ionization rate $\Gamma_{\rm H\,I}$ due to the large mean free path ($\lambda > 100$ Mpc) of ionizing photons at $z < 5$ that smooths the radiation field on large scales. More sophisticated models include the effect of discrete sources of ionizing photons and attenuate ionizing radiation with a constant mean free path (e.g. McDonald et al. 2005; Mesinger & Furlanetto 2009). Recently, Becker et al. (2015) (henceforth B15) discovered an enormous ~ 100 Mpc/h opaque trough in the Lyα forest spectrum of ULAS J0148+0600 covering $z \sim 5.5 - 5.9$ which is at odds with their uniform mean free path ionizing background simulations. They suggest that this discrepancy could be due to fluctuations in the mean free path of ionizing photons, possibly as a result of an extended reionization process.

However, the mean free path of ionizing photons is likely to vary substantially at $z \sim 5.6$ even in an ionization equilibrium context. Post-processing of hydrodynamical simulations of the IGM suggest that the mean free path should vary with the strength of the ionizing background as $\lambda \propto \Gamma_{\rm H\,I}^{\xi}$ with $\xi \sim 0.6$–0.8 (McQuinn et al. 2011; henceforth M11), and uniform mean free path ionizing background simulations at $z \sim 5.6$ lead to large-scale (tens of Mpc) regions with enhanced and diminished background (Mesinger & Furlanetto, 2009). Regions with a weak ionizing background should thus have a short mean free path, while regions with a strong ionizing background should be more transparent to ionizing photons.

In this work, we construct a semi-numerical model to compute the ionizing background in a large cosmological volume at $z \sim 5.6$ including a varying mean free path of ionizing photons. The local mean free path is iteratively determined by the local overdensity and strength of the ionizing background, the latter of which is computed by filtering ionizing radiation through the varying opacity medium. The resulting radiation field is "self-consistent" in the sense

that the opacity of the IGM and ionizing background are set by each other – the opacity depends on the strength of the ionizing background, and the ionizing background itself is filtered by that opacity. We then investigate the statistics of large-scale features in Lyα forest transmission that our new ionizing background model implies and compare to the observations compiled by B15.

The structure of the paper is as follows. In Section 4.2, we describe our models for sources and absorbers of ionizing photons. In Section 4.3, we compute the self-consistent fluctuations in the ionizing background and mean free path. In Section 4.4, we investigate an application of our ionizing background model to the statistics of large-scale Lyα forest absorption. In Section 4.5, we test the redshift evolution of our model across $z \sim 5.8$–5.4. In Section 4.6, we discuss the implications of our model on the IGM and sources of ionizing photons at high-redshift. Finally, in Section 4.7 we conclude with a summary and speculate on future observational tests of our model.

In this work we assume a standard ΛCDM model with $\Omega_{\rm m} = 0.3$, $\Omega_\Lambda = 0.7$, $h = 0.7$. Distance units are to be assumed comoving unless otherwise noted.

4.2 Sources and Sinks of Ionizing Photons

Our three-dimensional model for the ionizing background requires two ingredients: the distribution of ionizing sources, and a prescription for variations in the mean free path.

4.2.1 Semi-numerical Density and Halo Fields with DEXM

To construct the distribution of ionizing sources in our model, we use the semi-numerical cosmological simulation code DEXM (Mesinger & Furlanetto 2007; henceforth MF07). In the following, we summarize the method employed in DEXM, deferring the detailed implementation to MF07. We begin with a 2100^3 grid of Gaussian cosmological initial conditions (ICs) in a volume 400 Mpc on a side. The linear velocity field is then computed on a coarser grid of 700^3 using the Zel'dovich approximation (ZA; Zel'dovich 1970; Efstathiou et al. 1985). In

the public release of DEXM, the quasi-linear density field is then computed by displacing "particles" corresponding to the grid of initial conditions following the coarsely computed ZA velocity field (with no interpolation) and assigning their mass to the nearest grid cell to compute the density field. The right panel of Figure 4.1 shows that while the standard DEXM density field is reasonably smooth in high-density regions with a large number of particles per cell, in low-density regions there are grid cells with zero density and other artifacts. In particle-based cosmological simulations, a nearest-neighbor smoothing approach is typically performed on the particle distribution to estimate the continuous density field (e.g. Monaghan 1992; Springel 2005a). Nearest-neighbor schemes naturally degrade resolution in low-density environments in favor of high-density regions, ideal for computationally intensive hydrodynamical simulations of galaxy formation. However, these void environments are crucial to modeling transmission through the Lyα forest at $z > 5$ (Bolton & Becker, 2009), so we adopt a novel approach that does not degrade our simulation resolution through explicit smoothing.

The linear velocity field produced by the ZA is typically smooth on small scales, instead dominated by large-scale bulk flows of material into sheets and filaments. To compute the quasi-linear density field, we displace a super-resolved grid of 21000^3 IC particles by interpolating the ZA displacement field via trilinear interpolation and then bin these subparticles onto a 700^3 grid. The material in each IC grid cell is not only displaced but also stretched and sheared due to local gradients in the velocity field. Because the velocity field is smooth on small scales, this procedure results in a smooth distribution of matter on a uniform grid without any additional spatial filtering – even in the lowest density environments. The left panel of Figure 4.1 shows the resulting density field computed from the same ICs as the right panel.

We use the halo finding algorithm of DEXM to populate the simulation volume with a realistically-clustered distribution of dark matter halos. In brief, halos are located by filtering the linear density field on successively smaller scales and searching for (non-overlapping) regions where the filtered density $\delta(\vec{x}, M)$ is greater than the linear collapse threshold δ_c. We locate halos with masses as low as $M_h \sim 2 \times 10^9 M_\odot$ ($\sim$ 30 IC cells) and show the

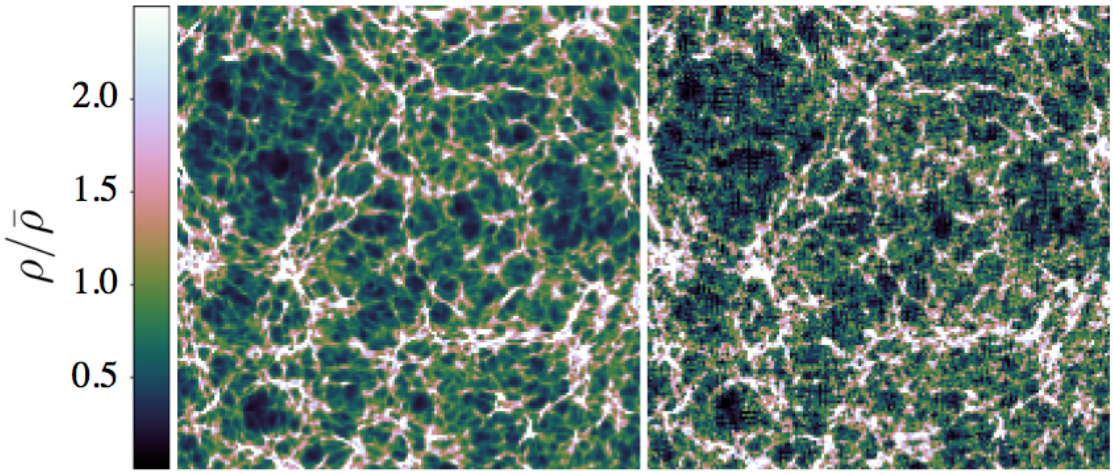

Figure 4.1: Comparison of the standard nearest-grid-particle Zel'dovich approximation density field from DEXM (right) with our interpolated ZA velocity approach (left). The slice shown is 0.57 Mpc thick (1 pixel) and 100 Mpc on a side.

resulting mass function at $z = 5.6$ compared to the Sheth & Tormen (1999) mass function in Figure 4.2. We then displace the halos using the ZA velocity field described above, enhancing their bias on large-scales and resulting in clustering statistics that are consistent with N-body simulations (MF07). As discussed by MF07, we do not expect one-to-one agreement between halo locations found with this procedure and those formed in an N-body simulation with the same initial conditions, but the agreement with large-scale clustering statistics is adequate for our purposes.

To compute the ionizing photon output of each halo, we abundance match to the observed UV luminosity function from Bouwens et al. (2015b) and assume a constant ratio of $f_{\rm ion}/A_{912}$ between the non-ionizing and ionizing continuum luminosity as in B15, where $A_{912} = 6.0$ is the expected ratio for a young stellar population and $f_{\rm ion}$ is a free parameter that represents a combination of the escape fraction of ionizing photons $f_{\rm esc}$ and uncertainties in the value of A_{912}. For easier comparison to the B15 models we further assume that the spectrum of ionizing photons emitted by each galaxy is a power law $L_\nu \propto \nu^{-\alpha}$ with $\alpha = 2.0$[1].

[1]See Section 5.1 of Becker & Bolton 2013 for a detailed assessment of this choice.

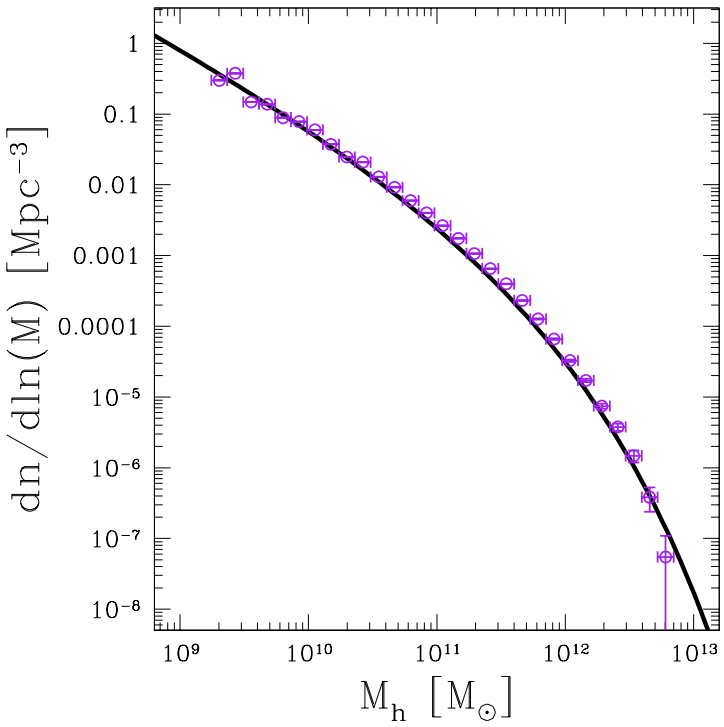

Figure 4.2: Sheth-Tormen halo mass function at $z = 5.6$ (solid curve) compared to the mass function of halos in our DEXM simulation (open points).

4.2.2 Varying Mean Free Path

The mean free path of ionizing photons in the IGM has been measured out to $z \sim 5$ through stacking analyses of quasar ionizing continua (Worseck et al. 2014) and by counting absorption lines in the Lyα forest (e.g. Songaila & Cowie 2010; Rudie et al. 2013). Typically this mean free path is assumed to be uniform in space. However, the mean free path itself should be sensitive to the strength of the ionizing background due to the regulation of H I absorber sizes (M11; see also Muñoz et al. 2014) and overdense regions likely contain more dense self-shielded gas.

M11 developed an analytic framework to describe the self-consistent relationship between the mean free path λ and the ionization rate Γ based on the IGM model of Miralda-Escudé et al. (2000) (henceforth MHR). The MHR model describes the ionization state of the universe by assuming that all gas with density above a critical value Δ_i is neutral, self-shielded from the ionizing background, while all lower density material is completely ionized. This means that global parameters that depend on the amount of neutral or ionized gas can be completely specified through the gas density probability distribution function (PDF) $P(\Delta)$. Additionally, the MHR model assumes that the mean free path is given by $\lambda \propto F_V(\Delta_i)^{-2/3}$, where $F_V(\Delta_i)$ is the volume filling factor of gas above the density Δ_i. If the gas density PDF is approximated by a power law $P(\Delta) \propto \Delta^{-\gamma}$, then $\lambda \propto \Delta_i^{2(\gamma-1)/3}$. Under the assumption of ionization equilibrium, M11 showed that $\Gamma \propto \Delta_i^{(7-\gamma)/3}$. In other words, $\lambda \propto \Delta_i^{2(\gamma-1)/(7-\gamma)}$. The fundamental picture is that if the ionization rate is larger, higher density gas will be ionized, reducing the total volume of neutral gas and thus increasing the mean free path (see also Muñoz et al. 2015). M11 then confirmed this scaling by performing radiative transfer through hydrodynamic cosmological simulations.

In our fiducial simulations we allow the mean free path to vary as $\lambda \propto \Gamma^{-2/3}$, corresponding to a gas density PDF $P(\Delta) \propto \Delta^{-2.5}$. This PDF is equivalent to assuming that all gas lies in spherically symmetric clouds with an isothermal density profile, i.e. $\rho \propto r^{-2}$. This is likely a conservative assumption; M11 found that the true PDF is likely to be even more steep at high redshift, leading to a more sensitive dependence with $\Gamma_{\rm H\,I}$. In Section 4.6 we

will discuss the effect of modifying this choice.

The variation of the mean free path with large-scale density depends on the relative number density of self-shielded absorbers. At $z \gtrsim 5.5$, the overdensity threshold for self-shielding is less than the virial overdensity, and so the population of absorbing clouds is likely dominated by the distant outskirts of very low-mass halos and filamentary structures in the IGM (Muñoz et al., 2014). These overdense structures are unresolved in our simulations and so we only attempt to describe the variation in their abundance on the same coarse scale as the ionizing background (see below). The absorbing clouds are likely only weakly biased with respect to the density field, so we assume a fiducial absorption bias of unity for simplicity (i.e. $\lambda \propto \Delta^{-1}$). However, in the densest environments in our simulations which have the strongest ionizing background, the Muñoz et al. (2014) argument for the connection between neutral gas and dark matter halos may hold, leading us to overestimate the mean free path in these regions. We leave a full exploration of the relationship between large-scale density and the mean free path for future work.

For comparison with B15, we assume that the column density distribution of absorbers that are most relevant to H I opacity ($N_{\rm H\,I} \sim N_{\rm LL} \sim 10^{17-18}$ cm^{-2}) behaves as a power law $f(N_{\rm H\,I}) \propto N^{-\beta}$ with $\beta = 1.3$, consistent with the $z \sim 2$–5 model in Becker & Bolton (2013). This implies a frequency dependence of the mean free path of $\lambda_\nu \propto \nu^{3(\beta-1)} \propto \nu^{0.9}$ (e.g. Haardt & Madau 1996). In practice, our results are insensitive to this choice because of the already steep frequency dependence of the H I cross section ($\propto \nu^{-3}$) and galaxy spectrum ($\propto \nu^{-2}$) which also contribute to the ionization rate calculation in the following section.

Extrapolation of the Worseck et al. (2014c) mean free path evolution fit to $z \sim 5.6$ suggests $\lambda \sim 54$ Mpc as an estimate of the average mean free path. However, the ionization rate in the IGM is constant from $2 \lesssim z \lesssim 5$ before dropping by an order of magnitude from $z \sim 5$ to $z \sim 6$ (Bolton & Haehnelt, 2007b; Wyithe & Bolton, 2011; Calverley et al., 2011). This suggests that extrapolation of this fit to higher redshifts is likely to *overestimate* the mean free path by as much as a factor of a few. In this work we are interested in exploring a range of fluctuating background scenarios, so we investigate models with $\lambda = 15$, 22, and 34 Mpc at the mean ionization rate.

4.3 Numerical model of the ionizing background

In this section, we describe the method used to compute the ionizing background given the ingredients listed in the previous section.

Our fiducial ionizing background models are computed on a coarse 80^3 grid, corresponding to cells of 5 Mpc on a side. This coarse resolution is sufficient for our purposes because it resolves the typical mean free path in our simulations (which sets the smoothing scale) and we have found little difference in the large-scale radiation field structures over a range of grid sizes from 48^3 to 100^3. The halo-finding procedure in Section 4.2.1 results in $\sim 2.4\times10^7$ halos. While a uniform mean free path computation of the radiation field is trivial for any number of sources (i.e. $J_\nu \propto \sum L_\nu \mathrm{e}^{-R/\lambda}/R^2$, or computed via FFT), self-consistently including the mean free path variations from Section 4.2.2 requires line-of-sight integrations between each source and grid cell. For computational efficiency, we bin the ionizing sources from Section 4.2.1 onto the ionizing background grid, then compute the local and non-local contributions to the ionizing background separately[2]. We additionally smooth the density field onto the same 80^3 grid for computational efficiency – as described in the previous section, we do not resolve neutral gas in our simulations, but instead assume that the number density of absorbers scales proportional to the large-scale overdensity.

The non-local contribution to the specific intensity J_ν at cell i is summed over every other cell j located at $\vec{r}_j$,

$$J_{\nu,i} = \sum_{j\neq i} \frac{L_{\nu,j}}{(4\pi|\vec{r}_i - \vec{r}_j|)^2} \mathrm{e}^{-\tau_\nu(\vec{r}_i,\vec{r}_j)}, \tag{4.1}$$

where $L_{\nu,j}$ is the specific luminosity of cell j and $\tau_\nu(\vec{r}_i,\vec{r}_j)$ is the integrated optical depth between cells i and j,

$$\tau_\nu(\vec{r}_i,\vec{r}_j) = \int_{\vec{r}_i}^{\vec{r}_k} [\lambda_\nu(\Gamma_{\mathrm{H\,I}}(\vec{r}),\Delta(\vec{r}))]^{-1} dr, \tag{4.2}$$

where λ_ν is the mean free path of frequency ν photons corresponding to $\Gamma_{\mathrm{H\,I}}$ and Δ along the line of sight. By integrating along the line of sight, the varying H I opacity of the IGM

[2]This reduces computation time in two ways: the number of sources drops from $\sim 2.4\times10^7$ to $\sim 5\times10^5$, and the opacity between each pair of cells only has to be computed once. Thus, the total computation time is decreased by a factor of ~ 100. The gain in efficiency is higher or lower depending on the resolution of the 3D grid.

due to variations in the strength of the radiation field and the large-scale density field is explicitly taken into account as described in the previous section.

The local contribution is computed by assuming that sources are spread evenly throughout each cell and can be described with a uniform emissivity ϵ_ν. The radiation field at the center of a uniform emissivity sphere of radius $l/2$ and mean free path λ is simply the integration over spherical shells with luminosity $dL = \epsilon \times 4\pi r^2 dr$ or

$$J_\nu^{\rm local,sphere} = \int_0^{l/2} \frac{\epsilon_\nu (4\pi r^2)}{(4\pi r)^2} {\rm e}^{-r/\lambda_\nu} dr = \frac{\epsilon_\nu \lambda_\nu}{4\pi} (1 - {\rm e}^{-(l/2)/\lambda_\nu}), \tag{4.3}$$

which reverts to the "absorption limited" approximation for the ionizing background intensity $J \approx \epsilon\lambda/4\pi$ (Meiksin & White, 2003) when integrated out to infinity. There is no simple exact expression for the radiation field at the center of a cubical volume with uniform emissivity, but we find numerically that the approximation

$$J_\nu^{\rm local,cube} \approx \frac{\epsilon_\nu \lambda_\nu}{4\pi} (1 - {\rm e}^{-\zeta l/\lambda_\nu}) \tag{4.4}$$

with $\zeta \approx 0.72$ results in an average ionization rate that is independent of spatial resolution.

Finally, the hydrogen ionization rate $\Gamma_{\rm H\,I}$ in each cell is computed by integrating over frequency,

$$\Gamma_{{\rm H\,I},i} = 4\pi \int_{\nu_{\rm H\,I}}^{4\nu_{\rm H\,I}} \frac{J_{\nu,i} + J_{\nu,i}^{\rm local}}{h\nu} \sigma_{\rm H\,I}(\nu) d\nu, \tag{4.5}$$

where $\sigma_{\rm H\,I}(\nu)$ is the hydrogen photoionization cross-section from Verner et al. (1996). This additional integration step considerably increases the computation time of our simulations relative to uniform mean free path models. By testing with lower-resolution 48^3 models, we find that the ionizing background fluctuations in the frequency-integrated model can be well-reproduced by a single-frequency model with $\nu \approx 1.32\nu_{\rm H\,I}$, and use this approximation to speed up computation of our highest resolution models[3].

Because the local mean free path is a function of $\Gamma_{\rm H\,I}$, the above procedure must be iterated ~ 10 times until the average change of $\Gamma_{\rm H\,I}$ per cell is less than 0.3%. At this point the ionization rate in the vast majority of the volume has converged, except for a very

[3]The 80^3 single-frequency models presented here require approximately 7 hours of runtime per iteration on a 12-core Intel Xeon (Nehalem generation) computer.

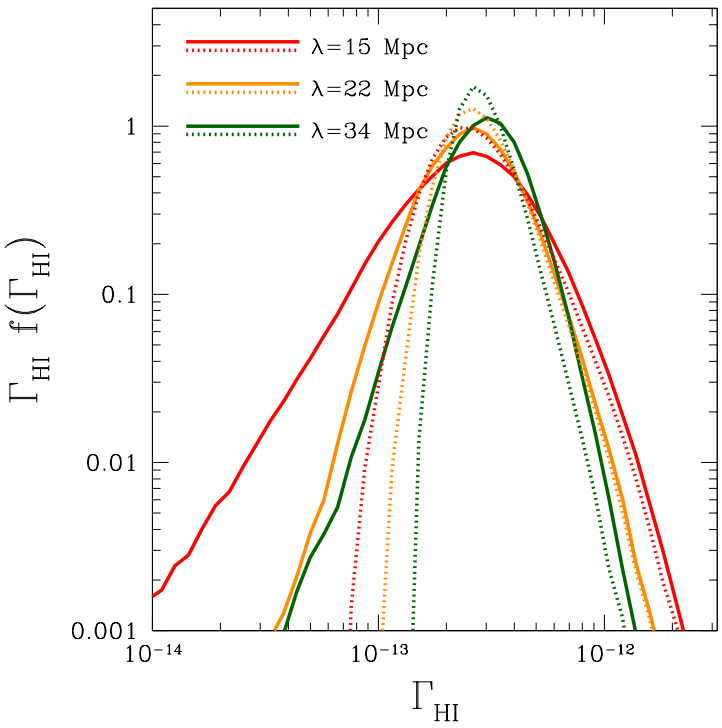

Figure 4.3: The solid curves show $\Gamma_{\rm HI} f(\Gamma_{\rm HI})$ from the fiducial ionizing background simulation at $z = 5.6$ for $\lambda = 15, 22, 34$ Mpc in red, blue, and orange, respectively. The dotted curves show the distributions from the corresponding uniform MFP models (i.e. the first iteration of the ionizing background calculation). The differences between the two sets therefore demonstrate the effect of mean free path fluctuations.

small fraction of cells at the center of opaque void regions that are strongly shielded from all ionizing sources.

In the rest of the paper, we will describe a series of models with a varying average mean free path. Models that employ a uniform mean free path (i.e. λ_ν = constant in equations 2 and 3 above) will be referred to as "uniform-λ" while those that include our full prescription for mean free path variations will be referred to as "fluctuating-λ". The uniform-λ models have been normalized to reproduce the same average Γ, and the fluctuating-λ models were computed using the uniform-λ model as the first iteration.

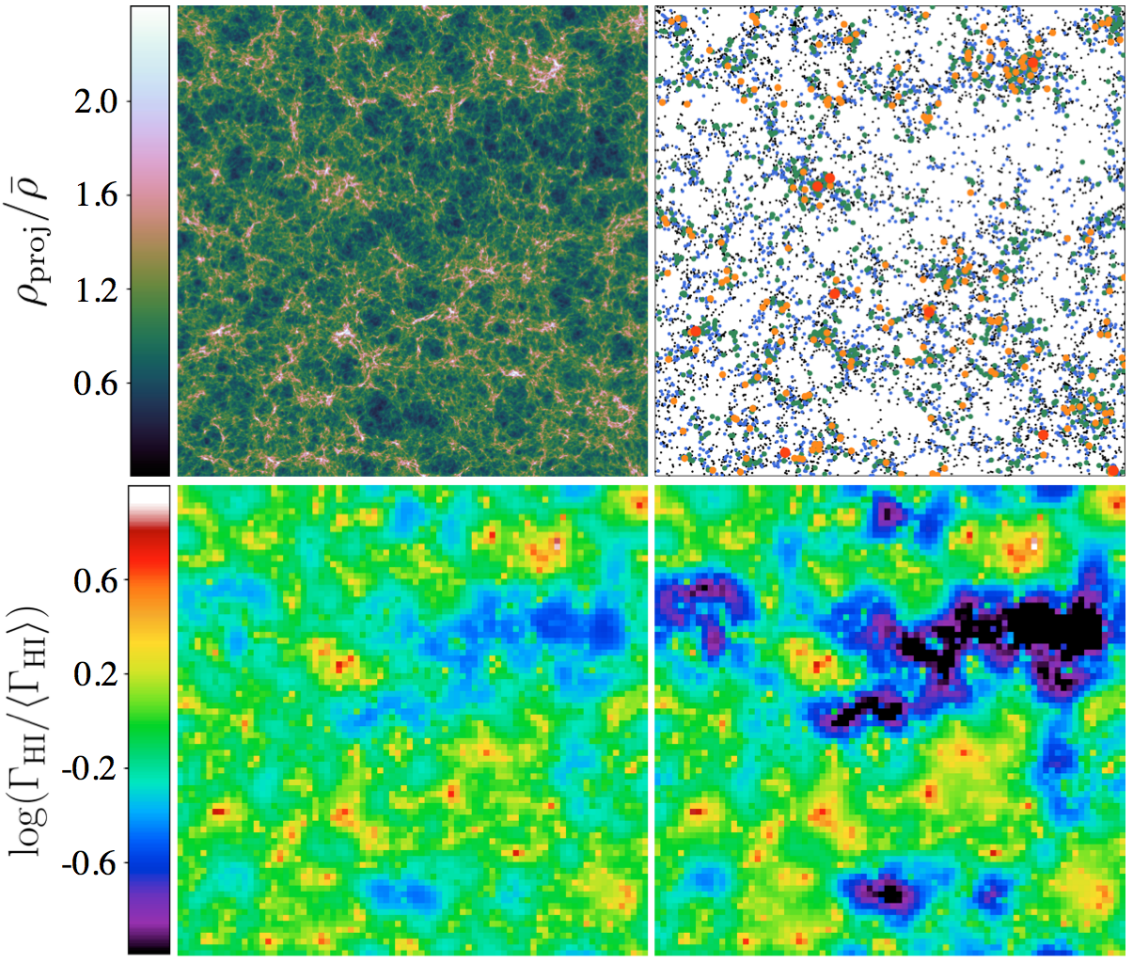

Figure 4.4: Top left: 20 Mpc-thick slice of the density field, 400 Mpc on a side. Top right: Halos found using the DEXM halo-finding procedure for the same slice. The size and color of each point represents the corresponding UV magnitude of the halo when matched to the Bouwens et al. (2015b) luminosity function, from $M_{\rm UV} \sim -18$ (black, smallest) through $M_{\rm UV} \sim -22$ (red, largest) in steps of $\Delta M = 1$. The halos shown represent the brightest $\sim 1\%$ of all galaxies in this slice, with halo masses ranging from $\sim 10^{10.8}$–$10^{12.3} M_{\odot}$. Bottom left: Fluctuations in the uniform-$\lambda = 15$ Mpc ionizing background model. Variations of a factor of $\sim$ 2–3 are common on large scales, as found by previous authors. Bottom right: Fluctuations in the fluctuating-$\lambda = 15$ Mpc ionizing background model. The addition of mean free path fluctuations greatly increases the fluctuations in $\Gamma_{\rm H\,I}$, especially to very low values on large scales.

4.3.1 Ionizing Background Results

In Figure 4.3, we show the distribution of $\Gamma_{\rm H\,I}$ for our fiducial fluctuating-λ models assuming $\lambda = 15$, 22, and 34 Mpc. The solid curves show the self-consistent fluctuating-λ models, while the dotted curves show the corresponding uniform-λ models. Mean free path fluctuations substantially broaden the distribution of $\Gamma_{\rm H\,I}$ towards lower values, and the strength of the effect strongly depends on the average λ. The bottom panels in Figure 4.4 demonstrate the spatial coherence of the background fluctuations graphically with 1 pixel-thick (5 Mpc) slices of the $\lambda = 15$ Mpc model in the uniform-λ and fluctuating-λ cases. The addition of a fluctuating mean free path greatly increases the contrast of the radiation field on $\gtrsim \lambda$ scales. The upper panels in Figure 4.4 show projected density and halo fields ± 10 Mpc from the ionizing background slice slice.

4.4 Implications for Large-scale Lyα Forest Transmission

Our simulations do not resolve the density and velocity fields at the Jeans scale of the gas at these redshifts, so we cannot produce realistic Lyα forest spectra. We can still estimate the effect the ionizing background fluctuations on the large-scale opacity of the Lyα forest by employing the fluctuating Gunn-Peterson approximation (FGPA; e.g. Weinberg et al. 1997) on sightlines through our evolved density field,

$$\tau_{\rm GP} \approx 35.6\kappa \left(\frac{T_0}{7500\,{\rm K}}\right)^{-0.724} \left(\frac{\Gamma_{\rm H\,I}}{3\times 10^{-13}\,{\rm s}^{-1}}\right)^{-1} \times \Delta^{2-0.724(\gamma-1)} \left(\frac{1+z}{6.6}\right)^{4.5}, \tag{4.6}$$

where T_0 is the temperature of the IGM at the mean density, γ is the slope of the temperature-density relation, and κ is a normalization factor to reproduce the measured mean transmission (as in, e.g., Dixon & Furlanetto 2009). We assume $T_0 = 7500$ K and $\gamma = 1.5$, consistent with standard models for the thermal history of the IGM (e.g. Puchwein et al. 2015). We choose a characteristic scale of 50 Mpc/h for comparison to B15 and compute the effective optical depth $\tau_{\rm eff} = -\ln(\sum_i^N {\rm e}^{\tau_{\rm GP}(r_i)}/N)$ in steps of ~ 0.06 Mpc (1/10th of one density field pixel) along each sightline. Our fiducial simulations have $\langle\Gamma_{\rm H\,I}\rangle \sim 3\times 10^{-13}$ s^{-1} and require

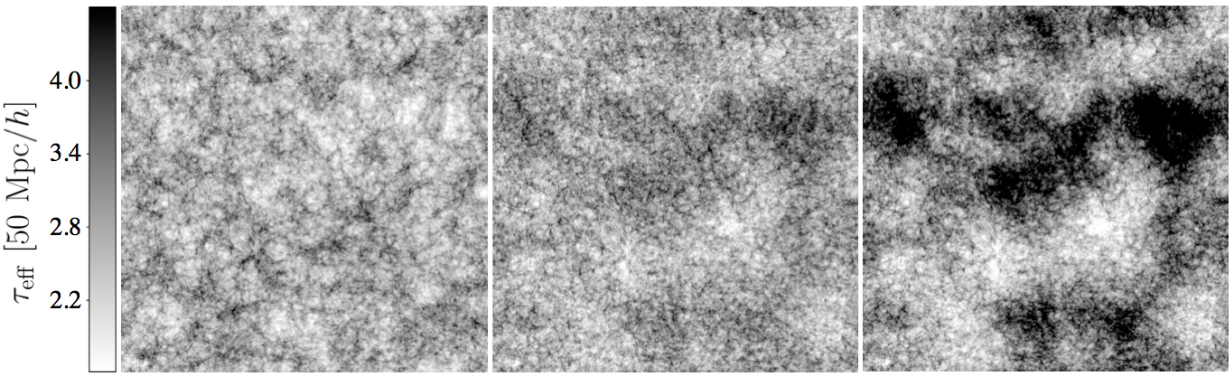

Figure 4.5: Maps of the 50 Mpc/h-projected $\tau_{\rm eff}$ in the Lyα forest at $z = 5.6$ centered on the same slice of the density field shown in Figure 4.4. The left panel shows the $\tau_{\rm eff}$ map for a uniform ionizing background, where the opacity is correlated with the density field (see the upper left panel in Figure 4.4). The middle panel demonstrates the effect of including a fluctuating ionizing background with a uniform λ: the relationship between projected density and $\tau_{\rm eff}$ reverses on large-scales due to the correlation of the density field with the radiation field. The right panel includes the full fluctuating-λ ionizing background model, greatly increasing the correlation and leading to very high $\tau_{\rm eff}$ in the center of large-scale voids.

$\kappa \sim 0.14$ to match the observed mean transmission. In Figure 4.5 we show "maps" of Lyα forest opacity along 50 Mpc/h sightlines perpendicular to the page, centered on the same slice shown in Figure 4.4, for three different models: uniform Γ, uniform-λ=15 Mpc, and fluctuating-λ=15 Mpc from left to right. It is clear that coherent large-scale structure in the radiation field at this redshift plays an important role in the large-scale opacity of the Lyα forest, and that the addition of mean free path fluctuations greatly enhances this effect.

The uniform $\Gamma_{\rm H\,I}$ slice in the left panel of Figure 4.5 is simply a reflection of the projected density field – regions with higher density show less transmission, and vice versa. This is the standard picture of the Lyα forest at lower redshifts when the ionizing background is largely uniform. High density regions only make up a small portion of the volume in the standard cosmological model, so opaque sightlines are rare. Once the correlation between the density field and the radiation field is strong enough, as in the fluctuating-λ model in the right panel of Figure 4.5, this picture reverses: low density regions become opaque due to a *local* dearth of ionizing photons, at least on scales larger than the average mean free path.

To determine the statistical properties throughout our simulation volume, we computed the Lyα effective optical depth along 250000 randomly positioned and oriented 50 Mpc/h sightlines. In Figure 4.6, we compare the observations by B15 to our $\lambda = 15$ Mpc models with and without mean free path fluctuations. The uniform background and uniform-λ models are nearly identical, despite the clear difference in physical environments corresponding to a given optical depth seen in Figure 4.5. In agreement with B15 we find that a uniform ionizing background is sufficient to describe the observed $P(< \tau_{\rm eff}) < 0.5$, but it fails to explain the tail to higher optical depths. Fluctuations in the mean free path naturally lead to a tail of high optical depths that are more consistent with observations than models that assume a uniform mean free path. In Figure 4.7 we show the distribution of $\tau_{\rm eff}$ for $\lambda = 15$, 22, and 34 Mpc fluctuating-λ models. The highest $\tau_{\rm eff}$ observed by B15 is extremely rare unless the average mean free path is small, and it is still quite rare even in our $\lambda = 15$ Mpc model. Because it provides the best fit to the observations, for the rest of the following we will treat the $\lambda = 15$ Mpc model as our fiducial model.

In Figure 4.8 we compare the relationship between the average density along each sightline and the resulting optical depth for the uniform ionizing background, uniform-λ, and fluctuating-λ models. While the average density and optical depth are tightly correlated when the ionizing background is uniform, the situation becomes more complex when the radiation field strongly fluctuates. While the distribution of $\tau_{\rm eff}$ is very similar between the uniform background and uniform-λ cases (Figure 4.6), the physical nature of a sightline with a given $\tau_{\rm eff}$ is different: the rare sightlines with high optical depth are modestly underdense, and dense regions are typically close to the median optical depth. This difference becomes greatly enhanced once mean free path fluctuations are included.

4.5 Evolution of the effective optical depth distribution from $z \sim$ 5.8–5.4

In the preceding sections, we attempted to explain observations of the variations in Lyα forest opacity at $z \sim 5.6$ in the context of a radiation field regulated by a fluctuating mean

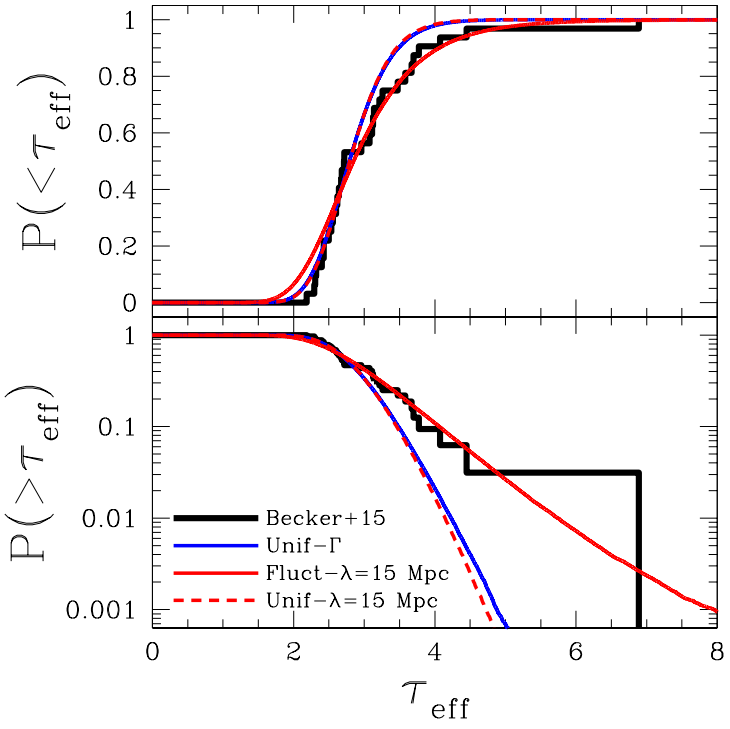

Figure 4.6: Top: Cumulative optical depth distribution $P(< \tau_{\rm eff})$ computed for the uniform background (blue curve) and $\lambda = 15$ Mpc fluctuating background models with uniform-λ (dashed red) and fluctuating-λ (solid red). The observed distribution from Becker et al. (2015), including lower limits, is shown as the black curve. Bottom: The same curves as the top panel but recast as $P(> \tau_{\rm eff}) = 1 - P(< \tau_{\rm eff})$ and shown on a logarithmic scale to emphasize the high-$\tau_{\rm eff}$ behavior.

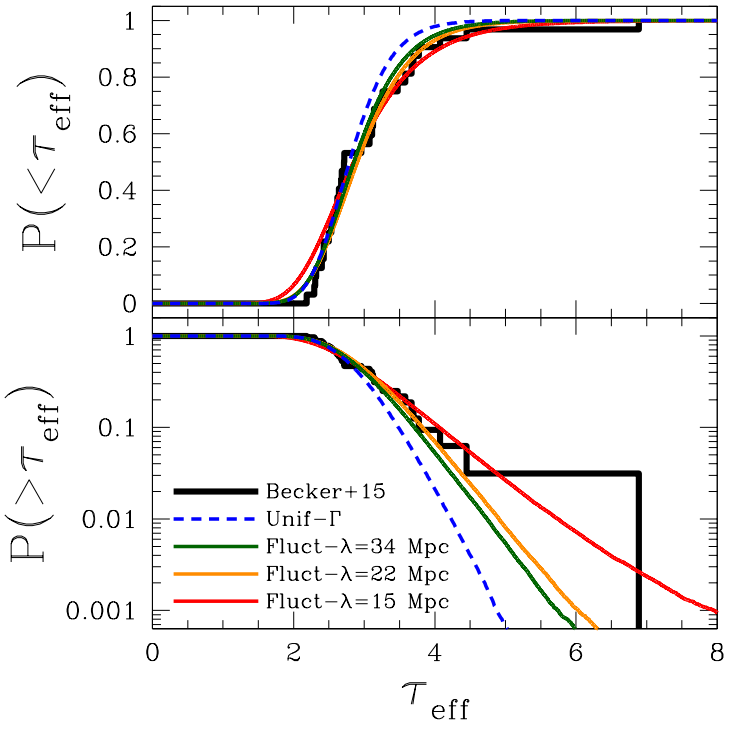

Figure 4.7: Top: Cumulative optical depth distribution $P(< \tau_{\rm eff})$ computed for the uniform background (dashed blue curve) and fluctuating background models (solid color curves). The red, orange, and green curves show the fluctuating-λ = 15, 22, and 34 Mpc models, respectively. The observed distribution from Becker et al. (2015), including lower limits, is shown as the black curve. Bottom: The same curves as the top panel but recast as $P(> \tau_{\rm eff}) = 1 - P(< \tau_{\rm eff})$ and shown on a logarithmic scale to emphasize the high-$\tau_{\rm eff}$ behavior.

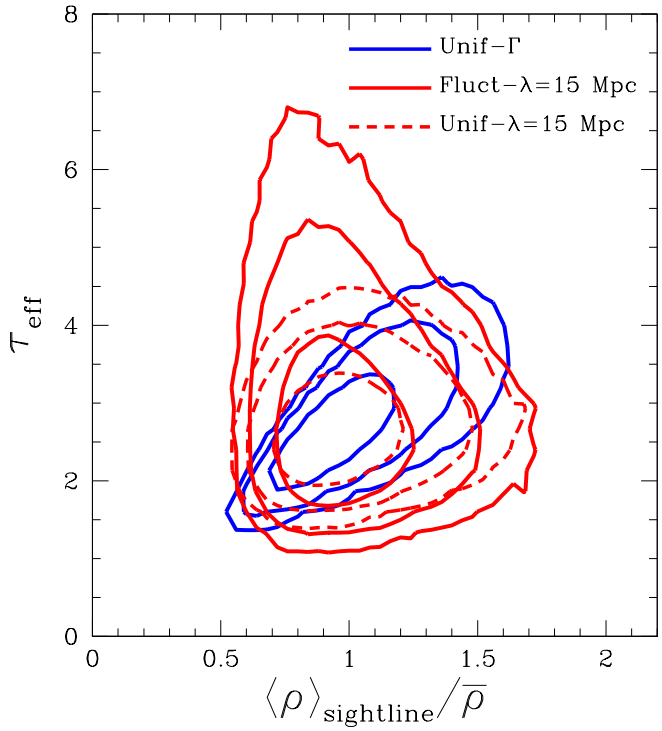

Figure 4.8: Relationship between average density along simulated sightlines and the resulting effective optical depth in the uniform (purple) and fluctuating (solid: fluctuating-λ, dashed: uniform-λ) ionizing background models. The contour levels enclose 68%, 95%, and 99% of sightlines. When the ionizing background is uniform, the large-scale opacity of the IGM is a tracer of the density field, as shown by the tight correlation of the blue contours (see also Figure 4.5). In contrast, in our fluctuating ionizing background model the most opaque regions of the Lyα forest correspond to underdense regions where the radiation field is suppressed. The addition of mean free path fluctuations greatly increases this effect.

free path. However, another interesting feature of the Lyα forest at these redshifts is the rapid decline in the average transmission above $z \sim 5.5$ (Fan et al., 2006) coincident with increased variations in transmission between sightlines (B15). Here we examine whether the fluctuating mean free path model described above can account for this evolution. In particular, we consider models at $z = 5.4$ and $z = 5.8$ to compare with the $z = 5.3$–5.5 and $z = 5.7$–5.9 $\tau_{\rm eff}$ distributions from B15.

To construct models at different redshifts that are consistent with each other, we follow the same procedure from Section 4.2 to create density and halo fields at $z = 5.4$ and $z = 5.8$ using the same initial conditions. Keeping the ratio between ionizing and non-ionizing UV luminosity fixed, integration of the Bouwens et al. (2015b) luminosity function (interpolated between $z \sim 5$–6) results in an evolution of the ionizing emissivity $\epsilon_{\rm ion} \propto (1+z)^{-2}$. As a rough approximation for the evolution of λ at fixed $\Gamma_{\rm H\,I}$, we assume the power law evolution $\lambda \propto (1+z)^{-4.4}$ (comoving) measured by Worseck et al. (2014c) across $2 < z < 5$ where $\Gamma_{\rm H\,I}$ is roughly constant (Becker & Bolton, 2013).

Primarily as a result of the rapid evolution in λ, in this model the average $\Gamma_{\rm H\,I}$ increases by more than a factor of two from $z = 5.8$ to $z = 5.4$. In Figure 4.9, we show the resulting evolution of the cumulative $\tau_{\rm eff}$ distributions in our $\lambda = 15$ Mpc model. The solid curves show the "best-fit" distributions obtained by tuning the κ parameter (equation 4.6) at each redshift. The $z = 5.6$ and $z = 5.8$ curves require the same κ to fit the observations, while $z = 5.4$ requires a substantially higher value. The dotted curve shows the $z = 5.4$ distribution using the same κ as the other redshifts, demonstrating a clear disagreement with the measured values. While the rapid $\Gamma_{\rm H\,I}$ evolution in our model is consistent with the observed evolution in the Lyα forest transmission from $z \sim 5.6$–5.8, it substantially underestimates $\tau_{\rm eff}$ at $z = 5.4$, requiring a substantial adjustment in κ from ~ 0.14 to ~ 0.22 to match observations. The simplest interpretation of this κ adjustment is that our model overestimates $\Gamma_{\rm H\,I}$ at $z = 5.4$ by about a factor of ~ 1.6, essentially requiring $\Gamma_{\rm H\,I}$ to be flat from $z = 5.4$–5.6 while increasing sharply from $z = 5.6$–5.8. This interpretation is in agreement with more sophisticated hydrodynamical simulations of the IGM that require a sudden change in the evolution of the ionizing background to match the observed $\tau_{\rm eff}$

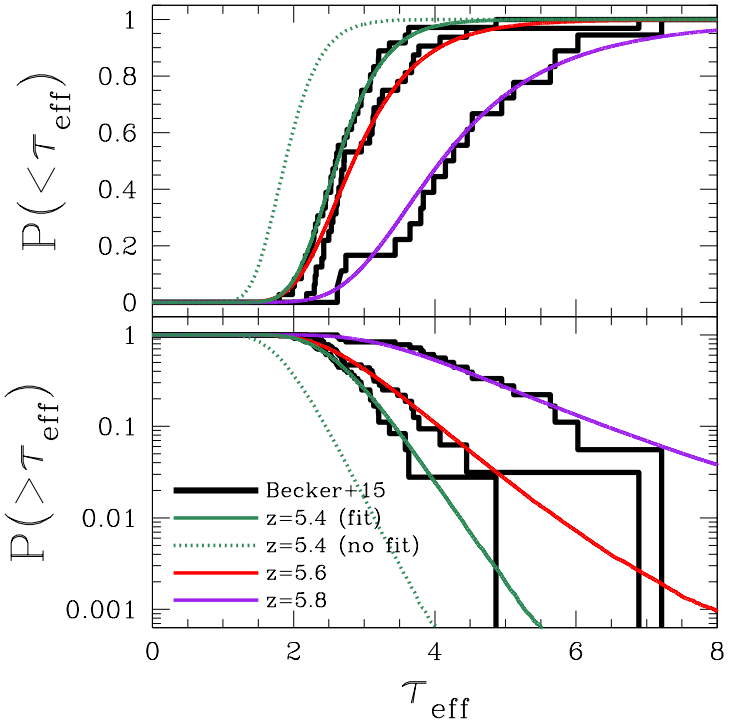

Figure 4.9: Top: Cumulative optical depth distributions $P(<\tau_{\rm eff})$ in the fluctuating λ model (green, red, purple curves) compared to the observations from Becker et al. (2015) (black curves) at $z \sim 5.4, 5.6, 5.8$ from left to right. The dotted green curve shows the distribution at $z = 5.4$ without renormalizing the optical depths with a new value of κ (see equation 4.6). Bottom: The same curves as above, but recast as $P(>\tau_{\rm eff}) = 1 - P(<\tau_{\rm eff})$ and shown on a logarithmic scale to emphasize the high-$\tau_{\rm eff}$ behavior.

evolution (G. Becker, priv. comm.).

4.6 Discussion

Models of the ionizing background that assume a uniform mean free path of ionizing photons are unable to reproduce the distribution of Gunn-Peterson troughs at $z \gtrsim 5.4$ (B15). Using our semi-numerical ionizing background model, we find that introducing fluctuations in the mean free path greatly enhances the fluctuations in the strength of the ionizing background. The increase in fluctuations manifests on the large-scales ($> \lambda$) required by observations.

Mean free path fluctuations come about due to the inherently fluctuating ionizing background in the Universe immediately following reionization – the average mean free path is short and early halos are strongly biased, so fluctuations in the ionizing background of roughly a factor of two above and below the mean are inevitable (Mesinger & Furlanetto, 2009) with underdense regions experiencing a weaker ionizing background than overdense regions.

The resulting mean free path fluctuations then depend on the competition between two effects: the regulation of absorbers by the ionizing background (M11) and the relative number density of absorbers due to the large-scale density field. Under reasonable assumptions ($\lambda \propto \Gamma_{\rm H\,I}^{2/3}\Delta^{-1}$), we find that on average the mean free path decreases in voids and increases in biased regions, leading to enhanced and diminished ionizing background strengths, respectively. Because the radiation field is effectively "smoothed" by the mean free path, the effect of mean free path fluctuations is most prominent on scales larger than the average mean free path in the IGM.

Applying these enhanced ionizing background fluctuations back onto the simulated density field, we find that the typical picture of the Lyα forest where transmission and density are anti-correlated reverses on large-scales (Figures 4.5 and 4.8). The resulting distribution of effective optical depths is very similar to observations if the average mean free path is relatively short ($\lambda \lesssim 20$ Mpc), although in detail we find that our model has difficulty matching the low-$\tau_{\rm eff}$ and high-$\tau_{\rm eff}$ ends of the distribution simultaneously.

4.6.1 Comparison to previous work

The impact of mean free path fluctuations on the Lyα forest has also been examined by Pontzen (2014) and Gontcho et al. (2014), albeit in the context of baryon acoustic oscillations measurements at $z \sim 2.3$. Pontzen (2014) showed that when mean free path fluctuations were included the bias of neutral hydrogen on scales larger than the mean free path becomes negative, in qualitative agreement with our results. In contrast to our non-linear 3D approach, both of these authors applied linear theory arguments to analytically compute the effect of mean free path fluctuations through scale-dependent bias of the radiation field.

They found that the measured flux power spectrum contains valuable information that may allow constraints on the properties of sources of ionizing photons and the mean free path (see also Pontzen et al. 2014). We leave simulations of the flux power spectrum to future work, but note that such arguments may still apply at $z > 5$ on much shorter scales that are more easily measured.

As discussed above, our model provides a much better fit to observations of the Lyα forest at $z \sim 5.6$ than the uniform mean free path models in B15. However, a direct comparison is complicated by our different methods for simulating the density field, the B15 model being higher resolution and a much more accurate simulation of the gas physics. In contrast to the B15 results, we do not find that uniform mean free path models produce a wider distribution of $\tau_{\rm eff}$ than uniform background models (see Figure 4.6), but this may be due to our inclusion of much fainter sources ($M_{\rm UV} \lesssim -13$ vs. $M_{\rm UV} \lesssim -18$) which act to smooth the radiation field because of their weaker level of clustering.

The ionizing emissivity in our fiducial $\lambda = 15$ Mpc model is $\epsilon_{\rm ion} \sim 1.8 \times 10^{25} (\langle \Gamma_{\rm H\,I} \rangle / 10^{-12.5}$ s^{-1}) erg s^{-1} Mpc^{-3} Hz^{-1}. This compares favorably with the estimates by Becker & Bolton (2013) and the required slow evolution to $z > 6$ implied by reionization constraints (Robertson et al., 2015; Bouwens et al., 2015a). We cannot claim to constrain the true value of $\epsilon_{\rm ion}$ with our model – in the context of our Lyα forest modeling, the low κ value we use implies a higher $\Gamma_{\rm H\,I}$ by a factor of ~ 7, but this ignores the substantial error in the mean transmission due to the low resolution of our simulated density field (Bolton & Becker, 2009) and other uncertainties due to the thermal history of the IGM and inaccuracies inherent to the FGPA method (e.g. Bolton et al. 2005). In addition, the average mean free path required to reproduce the observed tail to high optical depths may differ depending on the Γ and Δ dependencies of the mean free path. However, it is reassuring that our model is not grossly inconsistent with the current understanding of ionizing photon output at $z \sim 5.5$.

Recently, Chardin et al. (2015) attempted to address the broad distribution of effective optical depths by computing the radiative transfer of ionizing photons through small volume (10–40 Mpc on a side) high-resolution cosmological simulations. Following the end of reionization the ionizing background in their simulation volumes is extremely uniform, resulting

in only minor variations in $\tau_{\rm eff}$ between sightlines. As a potential explanation for the broad distribution observed by B15 they presented a toy "rare source" model where the ionizing background was dominated by a population of luminous quasars. Such a model is unlikely given the constraints on the number density of such sources (e.g. McGreer et al. 2013), and we suggest that a much simpler explanation for the uniformity of their simulated ionizing background exists. Because their simulation volumes are comparable or smaller than the mean free path after reionization (10–40 Mpc), the "smoothing" effect of the mean free path on the radiation field naturally leads to an almost completely uniform background. We believe that high-resolution radiative transfer modeling, similar to that of Chardin et al. (2015), is critical to understanding the regulation of neutral gas in the IGM by the ionizing background during and after reionization (e.g. Rahmati et al. 2013), but modeling the effect of mean free path fluctuations (i.e. large-scale variations in the properties of absorbers) requires volumes that are at least several λ on a side.

4.6.2 Variation of ionizing source and absorber parameters

The important assumptions we make for sources of ionizing photons in our model are as follows:

1. Duty cycle of unity
2. Fixed ratio of ionizing to non-ionizing UV luminosity
3. Minimum halo mass of $\sim 2 \times 10^9 M_\odot$

These three assumptions all relate to the effective bias of ionizing emissivity in our simulations. If the emissivity bias is larger, then the resulting fluctuations in the ionizing background and mean free path will be stronger. Decreasing the duty cycle from unity would result in an increased emissivity bias and thus result in stronger fluctuations, although likely only modestly (see: Mesinger & Furlanetto 2009). The ratio of ionizing to non-ionizing UV luminosity is typically assumed to be fixed, but the stellar properties and environments of UV-faint and UV-luminous galaxies are likely to be different. Recent simulations by Wise

et al. (2014) found that more massive (and thus more luminous) galaxies exhibited smaller $f_{\rm esc}$ than lower mass galaxies due to the relative robustness of their interstellar medium to supernova explosions. Reducing the ionizing photon output from high-luminosity galaxies would reduce the emissivity bias, leading to weaker fluctuations. However, due to the steep faint-end slope of the Bouwens et al. (2015b) UV luminosity function, the dominant contributors to the ionizing photon budget are already relatively faint galaxies ($M_{\rm UV} \sim -18$), so the effect on our results would likely be modest. For a similar reason, reducing the halo mass cutoff is unlikely to have a substantial effect on ionizing background fluctuations because the contribution from $M_{\rm UV} < -13$ to the UV luminosity density is small.

As discussed above, our mean free path model has two key parameters: the dependencies on $\Gamma_{\rm H\,I}$ and Δ. The mean free path should change with the strength of the ionizing background through regulation of the size of neutral absorbing clouds. Our assumption of $\lambda \propto \Gamma_{\rm H\,I}^{2/3}$ is equivalent to assuming a gas density PDF $P(\Delta) \propto \Delta^{-2.5}$. This assumption may be somewhat conservative – M11 found a steeper PDF slope at $z \sim 5.6$ in their hydrodynamic cosmological simulations corresponding to $\lambda \propto \Gamma_{\rm H\,I}^{\sim 3/4}$. By running additional simulations with this steeper dependence, we find that it has a modest effect that is barely distinguishable from simply adjusting the average mean free path. For example, a $\lambda = 22$ Mpc model run with $\lambda \propto \Gamma_{\rm H\,I}^{3/4}$ is nearly identical to our fiducial model with $\lambda = 15$ Mpc and $\lambda \propto \Gamma_{\rm H\,I}^{2/3}$. The mean free path should also depend on the density of the local environment – higher density regions will have more dense gas to absorb ionizing photons. For simplicity, we assumed that the number density of absorbers in a given volume is proportional to Δ, or $\lambda \propto \Delta^{-1}$. The extremely flat evolution of the ionizing background at $z \sim 2$–5 suggests that neutral gas is associated with dark matter halos (Muñoz et al., 2014) so we may be underestimating the effect that the density field has on the mean free path. At $z \sim 6$, when the ionizing background is evolving extremely rapidly, the overdensities associated with self-shielded gas become smaller than the virial overdensity (Muñoz et al., 2014), and so the bias of absorbers may be small. The sharp change in the inferred redshift evolution of the ionizing background at $z \sim 5.5$ (e.g. Fan et al. 2006) may reflect a transition from neutral gas residing predominantly in the IGM to neutral gas residing predominantly in collapsed

objects.

4.7 Conclusion

In this work, we have constructed a 3D semi-numerical model of the ionizing background that, for the first time, self-consistently includes the effect of fluctuations in the mean free path due to the ionizing radiation field and density field. We combine the semi-numerical halo model of DEXM (MF07) with a prescription for mean free path variations motivated by analytic calculations and hydrodynamic simulations (M11) and compute the ionizing background in a volume 400 Mpc on a side, iterating until the spatially variable mean free path and ionizing background are self-consistent. The resulting radiation field shows strongly enhanced fluctuations relative to previous models that assume a uniform mean free path. Applying the FGPA to sightlines through the quasi-linear density field in our simulation volume, we find that the addition of mean free path fluctuations substantially broadens the distribution of Lyα forest effective optical depths on large scales, particularly at the high-$\tau_{\rm eff}$ end which eluded previous work.

Many avenues exist to improve the predictive power of our model. Potential modifications include a larger simulation volume to better characterize the effect of cosmic variance and long wavelength modes, high-resolution N-body and/or hydrodynamic simulations for a more realistic IGM, and more sophisticated models for variations in the mean free path as a function of environment. Understanding the radiative feedback between ionizing sources and neutral absorbers may be critical to explaining the sudden shift in Lyα forest evolution at $z \sim 5.5$, and the distribution of effective optical depths is a key piece of that puzzle.

Because of the direct connection between large-scale features in the galaxy population to Gunn-Peterson troughs in the IGM, it may be possible to directly observe this effect in surveys of $z \sim 5.5$–5.9 galaxies in high-z QSO fields. For example, comparing the distribution of galaxies in the upper right panel of Figure 4.4 to the effective optical depth map in Figure 4.5, the number of $\gtrsim L_*$ galaxies in fields corresponding to sightlines with large opaque troughs at the same redshift is much smaller than fields with excess transmission. In

future work we will use our model to make predictions for the cross-correlation of large-scale Lyα forest $\tau_{\rm eff}$ and UV-selected galaxy populations that can be directly tested with current ground-based observatories.

CHAPTER 5

Quasar ionization front Lyα emission in an inhomogeneous intergalactic medium

5.1 Introduction

Following the recombination of the universe probed by the cosmic microwave background (CMB) at $z \sim 1100$, the universe consisted almost entirely of neutral hydrogen and helium. The first collapsed structures, stars, and galaxies proceeded to ionize the universe into the state that persists today (Loeb & Furlanetto, 2013). The faint galaxies that produced the majority of these ionizing photons are currently out of reach of modern instruments (Robertson et al., 2013; Oesch et al., 2013; Ellis et al., 2013), so the epoch of reionization is a valuable indirect probe of early structure formation. The time and duration of the reionization process is still under intense observational and theoretical investigation.

The simplest constraint on the epoch of reionization is the measurement of the electron scattering optical depth $\tau_{\rm e}$ by CMB experiments, which determines the average column density of electrons between the present day and the recombination epoch. Current measurements of $\tau_{\rm e}$ are consistent with an instantaneous reionization at $z \sim 10.6$ (Hinshaw et al., 2013), but modeling of the reionization process (e.g. Furlanetto et al. 2004) and kinetic Sunyaev-Zeldovich effect constraints (Zahn et al., 2012; Mesinger et al., 2012) suggest that it should be extended over $3 \lesssim \Delta z \lesssim 7$. More model-dependent constraints have been obtained by studying Lyα absorption in high-redshift quasar spectra, which suggest that the universe has been highly ionized since at least $z \sim 6$ (Fan et al., 2006). Recently, an observed drop in the fraction of broadband color-selected $z \gtrsim 7$ galaxies that show bright Lyα emission relative to $z \sim 6$ has also been used to infer a substantial increase in the neutral fraction

(Stark et al., 2010; Pentericci et al., 2011; Treu et al., 2012; Ono et al., 2012). Proposed measurements of 21 cm emission from the neutral cosmic web during reionization are a promising probe of the ionization state of the IGM (Furlanetto et al., 2006), especially in light of recent advances in foreground suppression (e.g. Parsons et al. 2014), but detection of this emission still eludes current instruments. The search for a definitive probe of reionization that is accessible to current or near-future instruments continues.

Cantalupo et al. (2008) (henceforth C08) introduced a novel method to study the progression and topology of reionization:[1] Lyα emission from the ionization front (IF) of a luminous quasar. While quasars are unlikely to have been an important source of ionizing photons during the reionization epoch (Fan et al., 2006), their (rare) ionized bubbles will be the largest coherent structures in the universe during reionization. C08 showed that the conditions within quasar IFs are ideal for producing Lyα emission. By definition, the IF is the narrow boundary between the neutral IGM (with a neutral fraction close to unity) and the inside of the ionized bubble (with a neutral fraction close to zero). Collisionally excited Lyα emission is strongest when the number of hydrogen atoms equals the number of free electrons, which occurs inside the IF. Also, quasar ionizing spectra are harder than the typically assumed ionizing spectrum of galaxies, and the extra energy of the ionizing photons heats up the gas to 2–4$\times10^4$ K. This temperature is hot enough that collisional excitations to the first excited state are efficient, and a substantial fraction of the absorbed energy is released as Lyα photons. This Lyα emission is analogous to Lyα fluorescence of optically-thick IGM clouds at intermediate redshift (Gould & Weinberg, 1996), but instead of relying on the static ionized skin of a dense system, the emission can arise from any part of the (initially) neutral IGM as the IF passes through it.

In their fiducial model, C08 calculated the ionization and heating of a uniform IGM with clumping factor $C \equiv \langle n^2 \rangle / \langle n \rangle^2 = 35$ by a quasar at $z = 6.5$ and performed Lyα radiative transfer to determine whether this Lyα emission could be observable. The observed ionized region around a luminous quasar depends strongly on finite speed-of-light effects (Yu,

[1]The idea of observing large-scale Lyα emission from the IGM during reionization was first investigated by Baltz et al. (1998), although in the different context of recombination emission from the entire IGM.

2005) which are computationally expensive to include in a radiative transfer code, but they corrected for this effect by re-scaling the timesteps in their simulation depending on the speed of IF expansion (we discuss this method further in Section 5.3.2). In the end, they found that the Lyα emission would appear as faint, large-scale (a few proper Mpc across, $\sim$ several arcmin^2) line emission with Lyα surface brightness $SB_{\mathrm{Ly}\alpha} \sim 10^{-20}((1+z)/7.5)^{-2}$ erg s^{-1} cm^{-2} arcsec^{-2} around quasars with luminosities similar to the population known at $z \gtrsim 6$, which is just bright enough to be barely detectable with current instruments.

We improve on the C08 calculation by performing ionizing continuum radiative transfer through an inhomogeneous IGM. As we show in the next section, the overall clumping factor of the IGM is insufficient to describe the physics of density inhomogeneities in the IF. We also include secondary ionizations by high energy photoelectrons, which significantly modify the shape and temperature of the IF, and correct for causal effects when the IF is propagating close to the speed of light. The net result of these effects is a substantial decrease in the expected Lyα emission, pushing it out of reach of existing instruments.

The structure of the paper is as follows. In Section 5.2 we summarize a basic analytic model for IF Lyα emission from an inhomogeneous IGM. In Section 5.3 we describe our numerical methods including one-dimensional radiative transfer and correction for causal effects. In Section 5.4 we describe the resulting ionization and temperature structure of our radiative transfer models in addition to the custom cosmological simulation from which we draw inhomogeneous IGM sightlines. In Section 5.5 we introduce an analytic method, calibrated to our radiative transfer results, that allows rapid, accurate computation of the causal-corrected Lyα emission along an IGM sightline and sheds light on the processes driving the IF Lyα emission. Finally, in Section 5.6 we discuss the results of our Lyα surface brightness calculation and investigate the detectability of this signal with current and upcoming instruments.

In this work we assume a ΛCDM cosmology with $\Omega_m = 0.3$, $\Omega_\Lambda = 0.7$, $\Omega_b = 0.048$, and $h = 0.68$.

5.2 Ionization Front Lyα Emission – Analytic Description

To build intuition, in this section we describe the basic physics involved in the Lyα emission from the IF. In particular, we discuss the dependence of the IF Lyα emission on the local density, which has not been addressed in past work.

For the conditions within a quasar IF, $T \sim 30,000$ K and neutral hydrogen fraction $x_{\rm H\,I} \sim 0.5$, the collisional excitation rate of Lyα can be orders of magnitude higher than the recombination rate within the ionized region (C08). To first order, the intensity of Lyα emission from the IF is simply a function of two things: the width of the IF, $dR_{\rm IF}$, and the average Lyα emissivity within the IF, $\langle \epsilon_{\rm Ly\alpha} \rangle$. The width of the IF is related to the mean free path of ionizing photons by $dR_{\rm IF} \propto (n_{\rm H} \bar{\sigma}_{\rm H\,I})^{-1}$, where $\bar{\sigma}_{\rm H\,I}$ is the effective ionization cross-section of ionizing photons within the IF and depends on the shape of the ionizing spectrum. The average energy of ionizing photons within the IF is a non-trivial function of the spectral index (Abel & Haehnelt, 1999), but is mostly constant as a function of time. Thus, along a sightline, the width of the IF varies as $dR_{\rm IF} \propto n_{\rm H}^{-1}$. The Ly$\alpha$ emissivity within the IF is a function of both density and temperature: $\epsilon_{\rm Ly\alpha} \propto n_{\rm H\,I} n_e q_{\rm eff}(T)$, where $q_{\rm eff}$ is the effective collisional excitation coefficient (C08). Assuming a constant temperature and ignoring the details of the $x_{\rm H\,I}$ profile within the IF, we can write $\langle \epsilon_{\rm Ly\alpha} \rangle \propto \langle n_{\rm H}^2 \rangle$. Finally, we arrive at the density dependence of the intensity of Lyα emission for a uniform density medium: $I_{\rm Ly\alpha} \propto dR_{\rm IF} \langle \epsilon_{\rm Ly\alpha} \rangle \propto \langle n_{\rm H}^2 \rangle / n_{\rm H}$. In a scenario where the material within the IF is at roughly a single density, the Lyα emission will be proportional to density instead of density squared, so the average intensity along a sightline may not necessarily reflect the overall clumping factor of the medium as assumed by C08. We will address the veracity of this assumption later in the paper.

The previous discussion assumed that the temperature within the IF was constant. However, this is not true in general. The temperature within the IF is largely a result of the competition between photoionization heating and (predominantly) collisional cooling processes. At a given radius from the source, the heating rate is only a function of the optical depth structure of the IF, which should be roughly constant with density, but the collisional

cooling rate will scale as $n_{\rm H}^2$. A simple analytic scaling can be derived as follows: assume there is a fixed temperature to which the IF would heat the medium in the absence of cooling, $T_{\rm max}$, reflecting the energy deposited by photoheating. The presence of cooling will reduce this temperature by an amount $\Delta T \propto t_{\rm IF} L_{\rm cool}/N_{\rm particles}$, where $t_{\rm IF}$ is the time a parcel of gas is within the IF, $L_{\rm cool}$ is the rate of energy loss to cooling, and $N_{\rm particles}$ is the number of gas particles. The time within the IF can be written as $t_{\rm IF} = dR_{\rm IF}/v_{\rm IF}$ where $v_{\rm IF}$ is the *instantaneous* velocity of the IF. The velocity of the IF is determined by the local flux of ionizing photons and density of neutral atoms. For a steady source and assuming constant density within the IF we have $v_{\rm IF} \propto n_{\rm H}^{-1} R^{-2}$. Because $dR_{\rm IF} \propto n_{\rm H}^{-1}$ as discussed before, we have $t_{\rm IF} \propto R^2$. If one further assumes a constant cooling rate within the IF dominated by Lyα excitation, $L_{\rm cool}/N_{\rm particles} \propto \epsilon_{{\rm Ly}\alpha}/n_{\rm H} \propto n_{\rm H}$. Thus, $\Delta T \propto n_{\rm H} R^2$. As expected, denser regions cool more due to collisions, and as the IF slows down at large radii this effect becomes stronger. The effect will in general be much weaker than the scaling derived here because the Lyα emissivity is a very strong function of temperature and will not remain constant. We derive a more accurate scaling of the IF temperature in Section 5.5.2.2. The resulting lower temperature within dense regions further weakens the density scaling of collisional Lyα emission from the IF.

The next step is to consider the inhomogeneous IGM. One way to account for inhomogeneities is to enhance the rate of collisional processes by a clumping factor $C = \langle n^2 \rangle / \langle n \rangle^2$ which can be estimated by cosmological simulations. This approximation assumes that the region of interest covers a broad range of densities representative of the IGM as a whole. This is likely reasonable for the large-scale roughly spherical extent of the IF. However, along the line of sight to the ionizing source, the IF is a relatively narrow structure: ~ 15 proper kpc in width[2] at the mean density of the universe at $z = 7$ for a power law ionizing spectrum typical of luminous quasars[3]. The intensity of Lyα emission from the IF depends on this line of sight profile: when the IF passes through a dense region, it becomes narrower, and as dis-

[2]Due to its density dependence, this width is more accurately (but perhaps less intuitively) described as a *column density* of roughly $N_{\rm IF} \sim 5 \times 10^{18}$ cm^{-2}.

[3]The IF is considerably wider than the mean free path at the ionizing edge ($\bar{n}_{\rm H} \sigma_{\rm H\,I}^{-1} \sim 1$ kpc at $z = 7$) because the average energy of ionizing photons within the IF is $\sim 3\nu_{\rm H\,I}$.

cussed above the temperature of the gas will also change. We will show that *the IF resolves clumping in the IGM*. This means that a clumping factor approximation overestimates the enhancement due to overdense regions. Instead, the average emission from the large-scale Lyα-emitting surface will depend on the relative amount of time spent in low versus high density regions, as well as other effects that we will discuss in Section 5.6. The amount of time that the IF spends in a given overdense region of size dr will be $t_{\rm IF} \sim dr/v_{\rm IF} \propto n_{\rm H}\, dr$. If one assumes (as a simple toy model) that dr scales with the Jeans length of the gas, then $dr \propto n_{\rm H}^{-1/2}$ and so $t_{\rm IF} \propto n_{\rm H}^{1/2}$. Thus, the IF would spend more time in overdense regions, but not enough to recover the $n_{\rm H}^2$ scaling assumed by a clumping factor.

5.3 Numerical Method

5.3.1 1D radiative transfer

To calculate the time-dependent properties of the IF, we developed a one-dimensional radiative transfer model based on the method of Bolton & Haehnelt (2007a). We assume a medium consisting solely of hydrogen and helium at their primordial ratios and a single steady source of ionizing radiation. The radiative transfer model solves the following time-dependent equations governing the abundance of ionized species as a function of time and distance from the ionizing source:

$$\frac{dn_{\rm H\,II}}{dt} = n_{\rm H\,I}(\Gamma^{\gamma}_{\rm H\,I} + n_e\Gamma^{\rm e}_{\rm H\,I}) - n_{\rm H\,II}n_e\alpha^{A}_{\rm H\,II}, \tag{5.1}$$

$$\frac{dn_{\rm He\,II}}{dt} = n_{\rm He\,I}(\Gamma^{\gamma}_{\rm He\,I} + n_e\Gamma^{\rm e}_{\rm He\,I}) + n_{\rm He\,III}n_e\alpha^{A}_{\rm He\,III} - n_{\rm He\,II}(\Gamma^{\gamma}_{\rm He\,II} + n_e\Gamma^{\rm e}_{\rm He\,II} - n_e\alpha^{A}_{\rm He\,II}), \tag{5.2}$$

$$\frac{dn_{\rm He\,III}}{dt} = n_{\rm He\,II}(\Gamma^{\gamma}_{\rm He\,II} + n_e\Gamma^{\rm e}_{\rm He\,II}) - n_{\rm He\,III}n_e\alpha^{A}_{\rm He\,III}, \tag{5.3}$$

where n_i, Γ^{γ}_i, $\Gamma^{\rm e}_i$, and α^{A}_i are the number densities, photoionization rates, collisional ionization rates, and Case A recombination rate coefficients[4] (Hui & Gnedin, 1997), respectively. The

[4]Case A is a reasonable approximation to a full treatment of recombination photons when $t \ll t_{\rm rec}$ (see, e.g., discussion in Cantalupo & Porciani 2011)

remaining species are solved by the closing conditions

$$n_{\rm H\,I} = n_{\rm H} - n_{\rm H\,II}, \tag{5.4}$$

$$n_{\rm He\,I} = \frac{Y}{4(1-Y)} n_{\rm H} - n_{\rm He\,II} - n_{\rm He\,III}, \tag{5.5}$$

$$n_e = n_{\rm H\,II} + n_{\rm He\,II} + 2n_{\rm He\,III}, \tag{5.6}$$

where $Y = 0.24$ is the mass fraction of helium.

The photoionization rate of species i, Γ_i^γ, consists of photoionization by the central source (or "primary" ionization; $\Gamma_{i,1}^\gamma$) and "secondary" ionization by energetic photoelectrons (Shull & van Steenberg 1985; $\Gamma_{i,2}^\gamma$). The collisional ionization by thermal electrons is included by the $\Gamma_i^{\rm e}$ terms using the fit from Theuns et al. (1998). The primary photoionization rate in a given cell is

$$n_i \Gamma_{i,1}^\gamma = \frac{1}{dV} \int_{\nu_i}^\infty \frac{L_\nu {\rm e}^{-\tau_\nu}}{h\nu} P_i d\nu, \tag{5.7}$$

where $L_\nu \propto \nu^{-\alpha_Q}$ is the specific luminosity of the ionizing source at frequency ν with spectral index α_Q, dV is the volume of a spherical shell of width dR at distance R from the source (the location of the cell), and τ_ν is the total optical depth to photons of frequency ν due to gas between the source and the cell. $P_i = {\rm e}^{-\Delta\tau_{\nu,i}}$ is the probability that species i is ionized by a photon with frequency ν inside of the cell, where $\Delta\tau_{\nu,i}$ is given by

$$\Delta\tau_{\nu,i} = f_i n_i \sigma_i(\nu) dR \tag{5.8}$$

where

$$f_i = \frac{n_i \sigma_i(\nu) dR}{\sum_i n_i \sigma_i(\nu) dR} \tag{5.9}$$

is the fraction of ionizations into species i (Friedrich et al. 2012; see also Altay et al. 2008) and $\sigma_i(\nu)$ is the photoionization cross-section of species i from Verner et al. (1996).

We include secondary ionizations by energetic photoelectrons as a function of electron energy using the results of Furlanetto & Johnson Stoever (2010) (henceforth FJS10). The secondary ionization rate is given by

$$n_i \Gamma_{i,2}^\gamma = \frac{1}{dV} \int_{\nu_i}^\infty f_{i,\nu}^{\rm ion} \left(\frac{h\nu - h\nu_i}{h\nu_i} \right) \frac{L_\nu e^{-\tau_\nu}}{h\nu} P_i d\nu, \tag{5.10}$$

where $f_{i,\nu}^{\rm ion}$, the fraction of photoelectron energy that goes into secondary ionization of species i, is calculated by interpolating the publicly available tables of FJS10.

Much of the remaining photoelectron energy is converted into thermal energy in the gas through collisions, with photoheating rates ϵ_i given by

$$n_i \epsilon_i = \frac{1}{dV} \int_{\nu_i}^{\infty} f_{i,\nu}^{\rm heat} (h\nu - h\nu_i) \frac{L_\nu e^{-\tau_\nu}}{h\nu} P_i d\nu, \tag{5.11}$$

where $f_{i,\nu}^{\rm heat}$ is the fraction of photoelectron energy that goes into heating the gas after a photon of frequency ν ionizes species i. Some of the photoelectron energy is released as Lyα emission,

$$n_i \epsilon_{\rm Ly\alpha,2nd} = \frac{1}{dV} \int_{\nu_i}^{\infty} f_{i,\nu}^{\rm Ly\alpha} (h\nu - h\nu_i) \frac{L_\nu e^{-\tau_\nu}}{h\nu} P_i d\nu, \tag{5.12}$$

where $f_{i,\nu}^{\rm Ly\alpha}$ is the fraction of secondary photoelectron energy released as Lyα photons. Contrary to the IF Lyα emission, these photons arise from the absorption of X-ray photons in the external neutral IGM. We find that, in detail, this emission is usually substantially fainter than the IF emission, and hence we ignore it for most of the following.

The calculations by FJS10 assume that all of the interactions of the energetic photoelectrons occur instantaneously. However, this is not actually the case. The timescale over which an electron with energy E is depleted by collisional ionization of hydrogen is roughly (FJS10)

$$t_{\rm loss,H} \sim 10^6 x_{\rm H\,I}^{-1} \left(\frac{E}{1\,{\rm keV}} \right)^{3/2} \Delta^{-1} \left(\frac{1+z}{8} \right)^{-3} {\rm yr}, \tag{5.13}$$

where $\Delta = n_{\rm H}/\bar{n}_{\rm H}(z)$ is the density in units of the cosmic mean at redshift z. We include this timescale in an approximate manner by suppressing the secondary ionization rate in a given grid cell for $\sim t_{\rm loss,H}$ before the IF reaches the cell. To ensure conservation of energy, the energy that would have gone into secondary ionizations is instead directed into heating the gas. We multiply the fraction of energy going into secondary ionizations $f_{\rm H\,I,\nu}^{\rm ion}$ by $1 - {\rm e}^{(t-t_{\rm IF})/t_{\rm loss}}$, where $t_{\rm IF}$ is an estimate of the time at which the IF will reach the current cell based on photon conservation (see Section 5.5) and t is the current time in the simulation. The energy removed from secondary ionizations is then put into heating by adjusting $f_{\rm H\,I,\nu}^{\rm heat}$ accordingly. This approximation causes the temperature and ionization structure to match

the no-secondaries model at very early times ($t \lesssim 10^5$ yr). Over the next few Myr it converges to a model following the unadjusted FJS10 rates. A more precise calculation of this effect taking into account the evolution of the time-dependent energy spectrum of electrons would be ideal but is outside the scope of the present work.

The temperature evolution is determined by

$$\frac{dT}{dt} = \frac{(\gamma - 1)\mu m_{\rm H}}{k_B \rho}(\mathcal{H}_{\rm tot} - \Lambda_{\rm tot}) - 2H(z)T - \frac{T}{n}\frac{dn_e}{dt}, \tag{5.14}$$

where $n = n_e + n_{\rm H} + n_{\rm He}$ is the total number density of all species, $\mathcal{H}_{\rm tot} = \sum_i n_i \epsilon_i$ is the total heating rate, μ is the mean molecular weight, $\Lambda_{\rm tot}$ is the total cooling rate, and $H(z)$ is the Hubble parameter. The cooling rate $\Lambda_{\rm tot}$ contains contributions from recombination cooling from Hui & Gnedin (1997), collisional excitation cooling and free-free emission from Cen (1992), and inverse Compton cooling off of CMB photons.

We compute the Lyα emissivity in a similar manner to C08. The effective Lyα collisional excitation coefficient is the sum over all collisional excitations from the ground state that lead to emission of a Lyα photon,

$$q_{\rm eff} = \sum_{n,l} f_{{\rm Ly}\alpha,nl} q_{1,nl}, \tag{5.15}$$

where $q_{1,nl}$ is the collisional excitation coefficient for the transition from the ground state to atomic level nl and $f_{{\rm Ly}\alpha,nl}$ is the fraction of transitions back to the ground state from atomic level nl that result in the emission of a Lyα photon (Pritchard & Furlanetto, 2006). We use the updated fits to the collisional excitation rate coefficients of Giovanardi et al. (1987) from Giovanardi & Palla (1989) and include excitations up to $n = 4$.

The calculation is discretized into a series of spatial grid cells that, for computational simplicity, correspond to spherical shells around the source. The physical structure of the IF depends on the density field, so to resolve the IF equally well at all times, we define the resolution of the spatial grid in terms of a hydrogen column density $N_{\rm H,cell}$. We find that adequate convergence of the Lyα emission and temperature structure is achieved when $N_{\rm H,cell} \sim 1.2 \times 10^{18}$ cm^{-2}, corresponding to a spatial resolution of $dR \sim 4$ kpc $\Delta^{-1}((1 + z)/8)^{-3}$. In order to avoid wiping out small-scale fluctuations in the density field inside of

voids, we require that $dR \geq dR(\Delta = 1)$, so $N_{\rm H,cell}$ will vary somewhat in underdense regions. This converged resolution may seem rather coarse – the initial optical depth at the hydrogen ionizing edge across each cell is ~ 10. However, the radiative transfer algorithm we use is well-suited to such optically thick cells (Bolton et al., 2004) and we confirmed that the temperature and ionization structure have converged (see Appendix A).

The integrals over frequency in equations (5.7–5.11) are computed as a discrete sum over 80 logarithmic frequency bins[5] from $\nu_{\rm ion,i}$ to $40\nu_{\rm ion,i}$ for each neutral (or partially neutral) species i (H I, He I, He II). In this sense we do not explicitly follow a single spectrum of photons but instead treat the ionizing spectrum of each species independently (except for the optical depths τ_ν and absorption probabilities P_i which include all species).

The global time step Δt is set by the speed of the IF. We require that the IF take more than one time step (typically $\gtrsim 2$) to cross the current grid cell of the IF,

$$\Delta t = \frac{4\pi R_{\rm IF}^2 N_{\rm H,cell}}{\dot{N}_{\rm ion}}, \tag{5.16}$$

where $R_{\rm IF}$ is defined to be the first cell from the origin with $x_{\rm H\,I} > 0.5$. However, while Δt is typically smaller than the light-travel time across the cell, it may be too coarse to accurately integrate the temperature and ionization state equations within the IF, so we loop over each cell with a sub-time step defined by requiring $\Delta n_i/n_i < 0.05$ for each species i and $\Delta T/T < 0.05$. We compute the average transmission of ionizing photons through the cell during the sub-time step loop to propagate a time-averaged spectrum of ionizing photons to the next cell. With these strict criteria on the global and sub-time steps, we avoid numerical artifacts (such as, e.g., the temperature "ringing" seen in Venkatesan & Benson 2011) and accurately compute ionization, heating, and cooling within the rapidly evolving IF.

5.3.2 Causal correction

The numerical radiative transfer method described in the preceding section assumes an infinite speed of light for ease of calculation. This assumption can lead to unphysical effects

[5]We did not attempt to optimize the number of frequency bins (e.g. Mirocha et al. 2012) but this appears to be adequate for convergence.

– most importantly IF velocities greater than the speed of light. Previous studies have found that the infinite speed of light calculation is an exact description of the IF propagation when observed along the line of sight to the source, and that the rest-frame behavior can be recovered by a simple change of coordinates (e.g. White et al. 2003; Shapiro et al. 2006; Bolton & Haehnelt 2007a). We discuss the detailed application of this effect to the IF below.

Let us assume a homogeneous medium for simplicity and an IF with a width $dR_{\rm IF}$ at radius $R_{\rm IF}(t)$ in the rest frame of the quasar. The IF will have a Lyα emissivity profile

$$\epsilon_{\rm Ly\alpha}(R) = I_{\rm rest} F\left(\frac{R - R_{\rm IF}(t)}{dR_{\rm IF}}\right), \tag{5.17}$$

where F is a function describing the emission profile of the IF as a function of radius, normalized such that $\int F(R/dR_{\rm IF})dR = 1$, and $I_{\rm rest}$ is the radially integrated emissivity of the IF. We ignore the time dependence of $I_{\rm rest}$ and $dR_{\rm IF}$ because the relevant timescale in the following is the light-crossing time of the IF.

The Lyα emission from the IF is observed on the light cone at angle θ from the line of sight (see Figure 3 of C08). The intensity on the light cone $I_{\rm LC}$ at time $t_{\rm LC}$ is then

$$\begin{aligned} I_{\rm LC} &= \int I_{\rm rest} F\left(\frac{R - R_{\rm IF}(t_{\rm LC} + R\cos\theta/c)}{dR_{\rm IF}}\right) dR \\ &= \int \left(1 - \frac{v_{\rm IF}(t)}{c}\cos\theta\right)^{-1} I_{\rm rest} F\left(\frac{y}{dR_{\rm IF}}\right) dy \\ &\approx \left(1 - \frac{v_{\rm IF}(t)}{c}\cos\theta\right)^{-1} I_{\rm rest}, \end{aligned} \tag{5.18}$$

where in the second line we have changed variables to $y = R - R_{\rm IF}(t_{\rm LC} + R\cos\theta/c)$ and in the third line we make the approximation that $v_{\rm IF}$ does not change over a light-crossing time. The time in the quasar rest-frame is $t = t_{\rm LC} + R\cos\theta/c$. Here, $v_{\rm IF}$ is the "correct" IF velocity accounting for a finite speed of light ($v_{\rm IF} < c$). Thus, the observed intensity of the IF is corrected by the factor $[1 - (v_{\rm IF}(t)/c)\cos\theta]^{-1}$. This factor is equivalent to the extra fractional time that a photon spends inside a moving IF relative to the static case ($v_{\rm IF} = 0$).

The infinite speed of light calculation provides IF Lyα intensity $I_{\rm code}$ and IF velocity $v_{{\rm IF},c=\infty}$ on the light cone for an observer at $\theta = 0$. This makes sense conceptually: in this frame, the order of photons as they are absorbed is the same as the order they were emitted,

even for photons absorbed at much different distances. To convert this to any arbitrary θ, we first rescale the time coordinate

$$\begin{aligned} t_{\rm code} + R/c &= t_{\rm LC} + R\cos\theta/c \\ t_{\rm LC} &= t_{\rm code} + \frac{R}{c}(1-\cos\theta) \end{aligned} \tag{5.19}$$

at every R. In practice, one can instead implement this at $R = R_{\rm IF}$ by re-scaling the numerical time steps,

$$dt_{\rm LC} = dt_{\rm code}\left(1 + \frac{v_{{\rm IF},c=\infty}}{c}(1-\cos\theta)\right), \tag{5.20}$$

as in C08. The intensity computed from the code is related to the rest-frame intensity through equation (5.18),

$$I_{\rm code} = (1 - v_{\rm IF}/c)^{-1} I_{\rm rest}, \tag{5.21}$$

so the intensity on the light cone is then

$$\begin{aligned} I_{\rm LC} &= \left(1 - \frac{v_{\rm IF}}{c}\cos\theta\right)^{-1} I_{\rm rest} \\ &= \frac{1 - v_{\rm IF}/c}{1 - (v_{\rm IF}/c)\cos\theta} I_{\rm code}. \end{aligned} \tag{5.22}$$

The rest-frame IF velocity $v_{\rm IF}$ is related to the infinite speed of light IF velocity $v_{{\rm IF},c=\infty}$ from the code by (Shapiro et al., 2006)

$$v_{\rm IF} = \frac{v_{{\rm IF},c=\infty}}{1 + v_{{\rm IF},c=\infty}/c}, \tag{5.23}$$

so that

$$I_{\rm LC} = \left(1 + \frac{v_{{\rm IF},c=\infty}}{c}(1-\cos\theta)\right)^{-1} I_{\rm code}. \tag{5.24}$$

In order to properly compute the IF Lyα emission by correcting the infinite speed of light calculation in the manner described above, the calculation must provide an accurate gas temperature. We show below that this is indeed the case.

An arbitrary gas property Z at position x along a sightline is only influenced by properties at $x' > x$ if x' is on its backward light cone. We can write an equation describing the evolution of Z with time,

$$Z(x,t) = Z(x, t - dt) + \int_x^\infty f(x', t - [x' - x]/c) dt dx', \tag{5.25}$$

where f is an unspecified function. If, for example, Z is the ionization state of the gas, f describes the absorption of photons at positions x' along the light cone and the luminosity of the quasar at time $t - [x_{\rm Q} - x]/c$. Writing the above as a differential equation we find

$$\frac{dZ(x, t - x/c)}{dt} = \int_x^\infty dx' f(x', t - x'/c). \tag{5.26}$$

Then, evaluating Z on the light cone,

$$\frac{dZ(x, t_{\rm LC})}{dt_{\rm LC}} = \int_x^\infty dx' f(x', t_{\rm LC}), \tag{5.27}$$

using $t_{\rm LC} = t - x'/c$ and the fact that the Jacobian for the coordinate transformation $dtdx \rightarrow dt_{\rm LC}dx$ is equal to unity.

The equation above is identical to the equation that the infinite speed of light code solves for property Z:

$$\frac{dZ(x, t)}{dt} = \int_x^\infty dx' f(x', t). \tag{5.28}$$

Thus, as long as the boundary conditions for $Z(x, t)$ are the same as the light cone time boundary conditions, the infinite speed of light calculation gives the same solution for the state of the gas as explicitly solving on the light cone.

The argument above implies that the time evolution of physical properties computed by the infinite speed of light code is correct, with the caveat that $t_{\rm code} = 0$ corresponds to the time when the region "sees" the quasar turn on at $t_{\rm LC} = R/c$. This means that the "unphysical" ionization and heating at large radii is perfectly natural and should lead to accurate gas properties inside the IF. Another implication of this is that the application of the "loss timescale" of high-energy photoelectrons as described in the previous section should be accurate because the time coordinate is only translated, not stretched. That is, the time between the IF reaching a given cell and the time the cell was first illuminated by X-rays is equivalent to $t_{\rm IF}$.

While C08 corrected their infinite speed of light simulations to the time observed on the light cone with equation (5.20), it appears they did not include the additional correction to the intensity in equation (5.24). The physical reason for this correction is a difference in the width of the IF when a finite speed of light is taken into account. Consider the rest-frame

($\theta = \pi/2$) expansion of the IF. The width of a slow ($v_{\rm IF} \ll c$) IF is given by the optical depth of ionizing photons into the neutral medium, but for a fast ($v_{\rm IF} \sim c$) IF, the width is instead limited by the ionization timescale $t_{\rm ion} \sim \Gamma_{\rm H\,I}^{-1}$ as neutral gas is illuminated inside the causal boundary $R = ct$. Miralda-Escudé & Rees (1994) showed that the difference between these two widths is given by the correction factor in equation (5.24) with $\theta = \pi/2$. For different θ the correction is analogous to having a finite speed of light equal to $c(1 - \cos\theta)^{-1}$ which is the maximum IF velocity along the light cone.

A full application of this correction requires changing coordinates via equation (5.19) at every cell and timestep in the radiative transfer model. This requires significantly higher spatial and temporal resolution than the infinite speed of light calculation, so in general we do not apply the correction factor directly to the radiative transfer results presented in the following section. Instead, we apply the correction factor to a simplified, yet accurate, analytic model of IF Lyα emission discussed in Section 5.5. We have verified with a handful of high-resolution causal-corrected (via equation 5.19) simulations that this approximation is accurate enough for our purposes. In the rest of the paper, we will refer to the corrections to the time coordinate and Lyα intensity in this section as the "causal correction".

5.4 Radiative Transfer Results

In this section we present the results of our radiative transfer modeling for both a uniform IGM test case and for sightlines through an inhomogeneous IGM drawn from numerical simulations at $z = 7.1$. The results presented in this section assume an infinite speed of light, and do not include the causal correction discussed in Section 5.3.2.

5.4.1 Uniform IGM

We have run a series of simple models assuming a constant density IGM to demonstrate the response of the ionization and temperature structure to the treatment of secondary ionizations and source properties. Our fiducial test model assumes a $\dot{N}_{\rm ion} = 10^{57}$ s^{-1} quasar with EUV spectral index $\alpha = 1.5$, similar to the inferred ionizing emission properties of

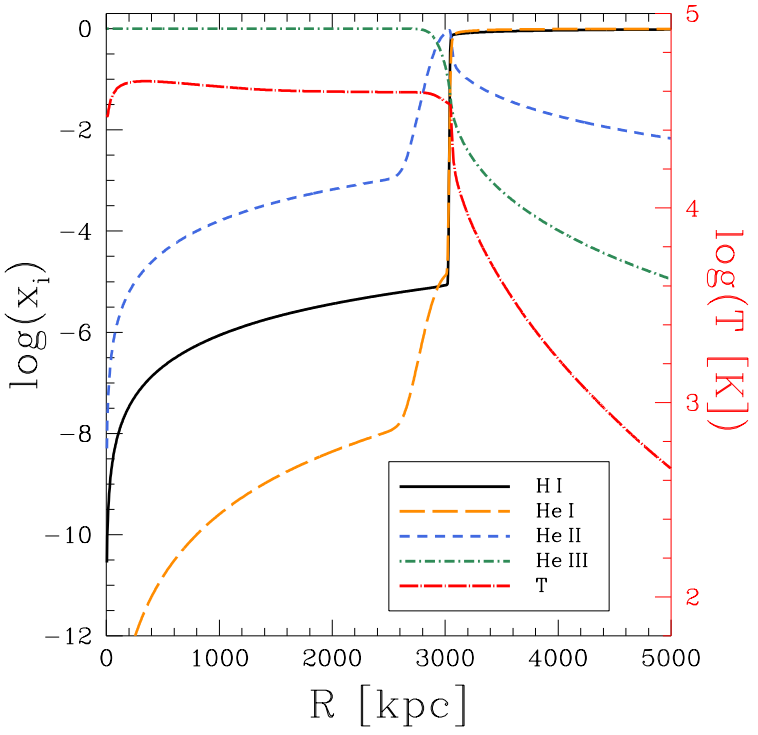

Figure 5.1: Ionization and temperature structure from the radiative transfer model in a uniform medium at $z = 7$ with our fiducial uniform model parameters: $\dot{N}_{\rm ion} = 10^{57}$ s^{-1}, $\alpha_{\rm Q} = 1.5$, $t_{\rm code} = 10$ Myr. Species fractions $x_{\rm H\,I}$ (solid, black), $x_{\rm He\,I}$ (long-dashed, orange), $x_{\rm He\,II}$ (short-dashed, blue), and $x_{\rm He\,III}$ (dot-dashed, green) are shown along with the gas temperature (long-dot-dashed, red).

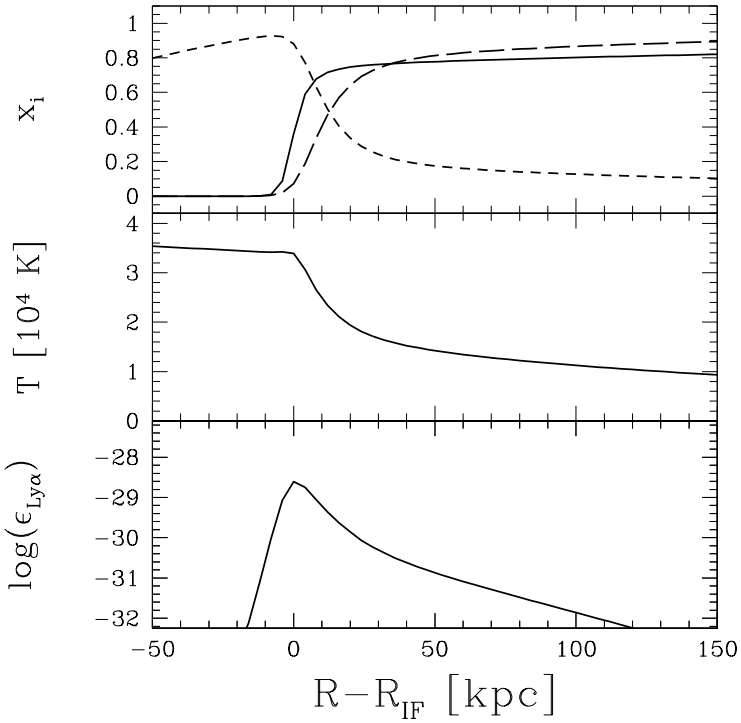

Figure 5.2: Zoom in on the IF ionization structure (top panel), temperature (middle), and Lyα emissivity (bottom) of the fiducial uniform model (see Figure 5.1). In the top panel the solid, long-dashed, and short-dashed curves are the species fractions $x_{\rm H\,I}$, $x_{\rm He\,I}$, and $x_{\rm He\,II}$, respectively.

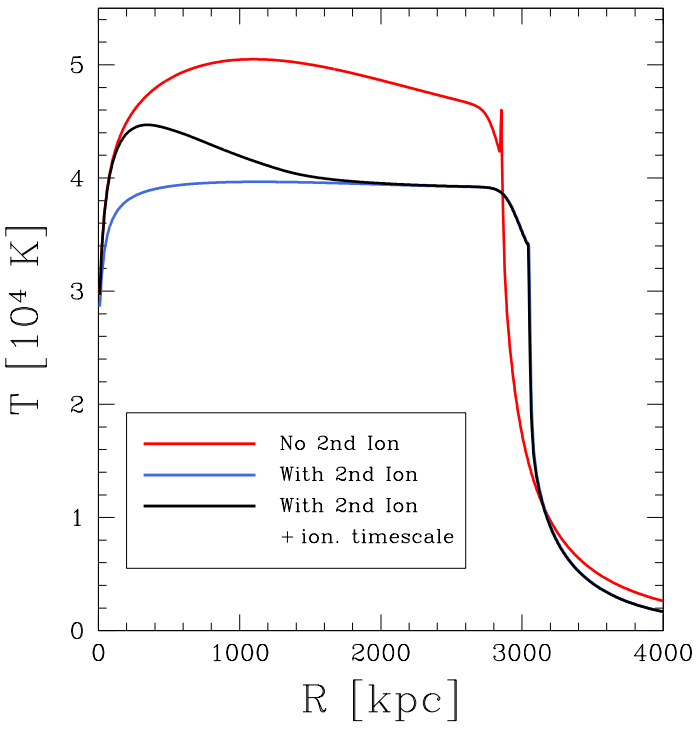

Figure 5.3: Dependence of the temperature structure on secondary ionizations and the secondary ionization timescale correction in the fiducial uniform model (see Figure 5.1). The black curve is the fiducial prescription, the blue curve does not have the secondary ionization timescale correction (see text), and the red curve does not include secondary ionizations at all.

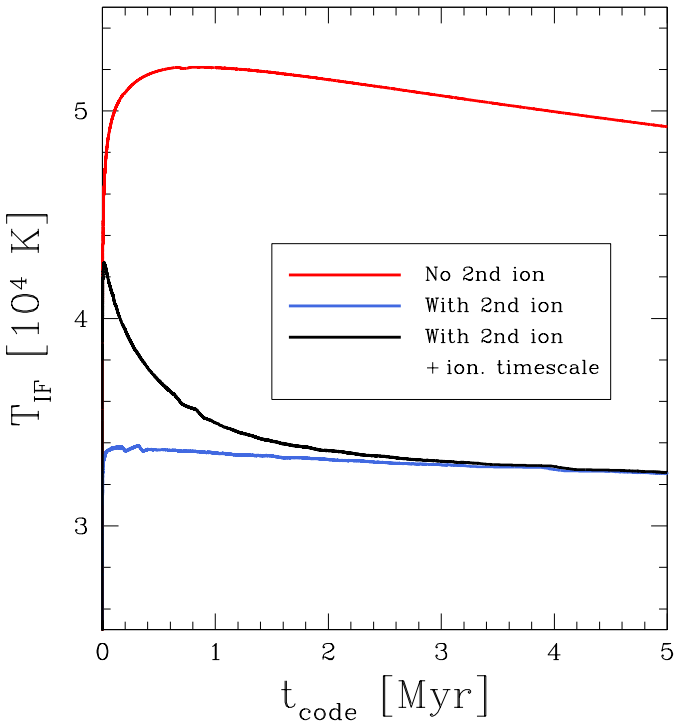

Figure 5.4: IF temperature as a function of time for models without secondary ionizations (red curve), with secondary ionizations (blue curve), and with secondary ionizations plus an ionization timescale correction (black curve) using the fiducial uniform model of Figure 5.1.

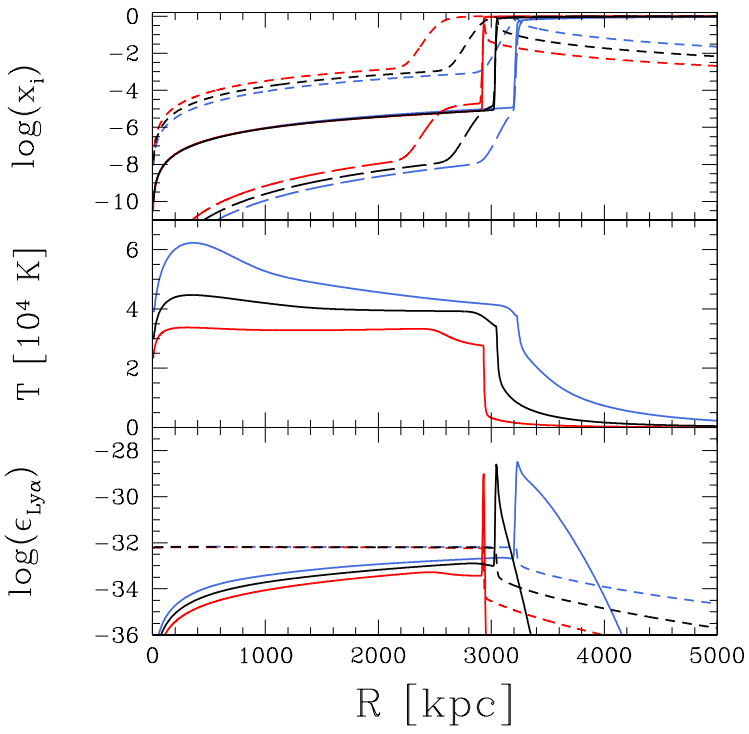

Figure 5.5: IF ionization structure (top), temperature (middle), and Lyα emissivity of the fiducial uniform model (see Figure 5.1) with varying quasar spectral index $\alpha_{\rm Q} = 1.0, 1.5, 2.0$ (blue, black, red, respectively). In the top panel, the solid, long-dashed, and short-dashed curves are the species fractions $x_{\rm H\,I}$, $x_{\rm He\,I}$, and $x_{\rm He\,II}$, respectively. In the bottom panel, the solid curves are the Lyα emissivity due to collisional excitation and the short-dashed curves are the Lyα emissivity from recombinations.

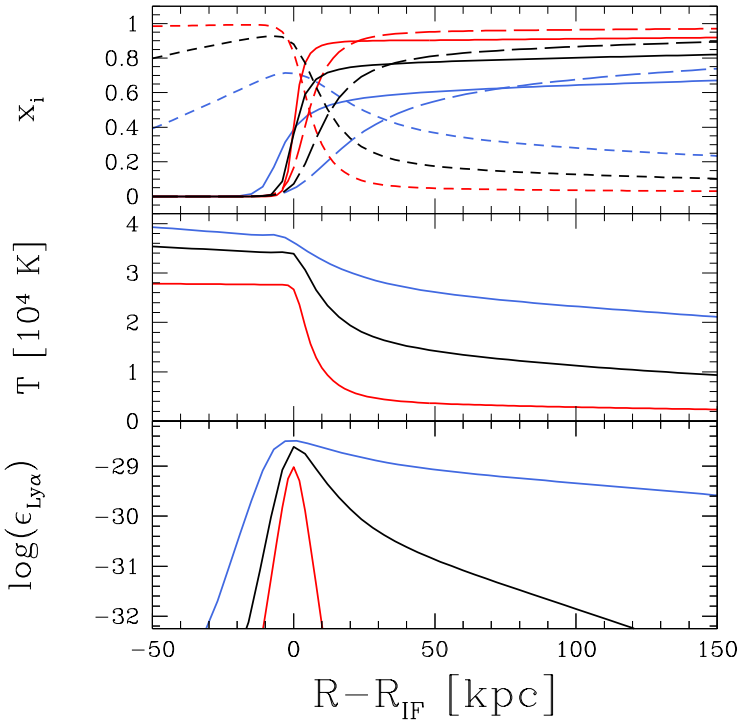

Figure 5.6: IF ionization structure (top), temperature (middle), and Lyα emissivity (bottom) of the fiducial uniform model (see Figure 5.1) with varying quasar spectral index $\alpha_{\rm Q} = 1.0, 1.5, 2.0$ (blue, black, red, respectively). The line styles are the same as Figure 5.5. Each curve has been shifted to $R - R_{\rm IF}$ for ease of comparison.

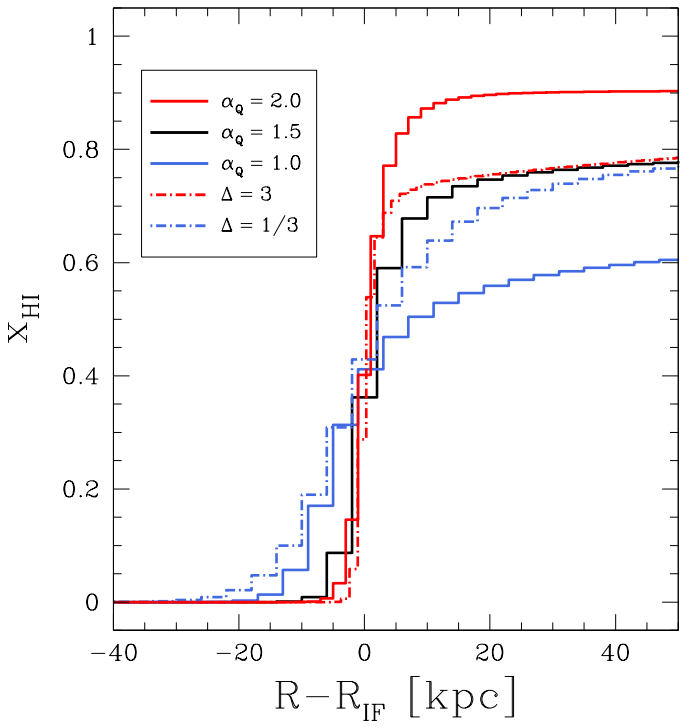

Figure 5.7: IF neutral hydrogen structure when the density (dot-dashed) and spectral index (solid) are varied to higher (red) and lower (blue) values compared to the fiducial uniform model of Figure 5.1 (black).

known luminous $z \gtrsim 6$ quasars (Bolton & Haehnelt, 2007a; Mortlock et al., 2011), emitting into a uniform IGM with density equal to the cosmic mean at $z = 7$ and an initial temperature of 10 K for $t_{\rm code} = 10$ Myr.

In Figure 5.1 we show the resulting ionized and neutral fractions for hydrogen and helium as well as the temperature structure. At large radii, hard UV/X-ray photons significantly "preheat" the medium up to $\sim 2\times10^4$ K and introduce a low level of ionization to the initially neutral medium ($x_{\rm H\,II} \sim 0.05$). Figure 5.2 zooms in on the region close to the IF and shows that just beyond the IF lies a "pre-ionization" region where secondary ionizations from high energy photons ionize $\sim 10\%$ of the H I in a long tail outside of the IF. Within the IF itself, despite ongoing H I and He I photoheating, the temperature stops increasing once $x_{\rm H\,I} \sim 0.5$ – this is when the cooling rate due to collisional excitation is strongest and the ionizations are predominantly due to the lowest energy ionizing photons. Within the H I/He I ionized region lies the relatively broad He II IF which increases the gas temperature by another $\sim 10^4$ K. The bottom panel of Figure 5.2 shows that the Lyα emission is strongly peaked at the center of the IF, as expected, with a weak tail within the pre-ionization region. Assuming a (somewhat unrealistic) spherical shell morphology, the total integrated Lyα luminosity from collisions within the IF is orders of magnitude larger than the recombination emission within the ionized bubble, assuming a uniform medium.

5.4.1.1 Secondary Ionizations

The inclusion of secondary ionizations has a substantial impact on the ionization and temperature structure of our radiative transfer model. Figure 5.3 shows the effect of our secondary ionization prescription on the temperature profile. A significant amount of energy that would otherwise go into heating the IGM instead goes into ionizations, causing a tradeoff between the size of the ionized bubble and the post-IF temperature. Our rough correction for the timescale of secondary ionizations causes the temperature profile to follow the no-secondaries model at early times, but Figure 5.4 shows that the temperature within the IF is largely unaffected after ~ 2 Myr. The IF is somewhat broadened by secondary ionizations because

they increase the number of ionizations from higher energy photons that can penetrate farther into the neutral medium. Despite the broader IF, the substantially lower temperature results in a factor of a few less Lyα emission.

5.4.1.2 Variation of input parameters

Figure 5.5 shows the effect of changing the input quasar spectrum while leaving the total number of ionizing photons constant. The average energy of the ionizing photons regulates the enhanced ionization rate due to secondary ionizations, the heating of the IGM, and the width of the IF. The combination of the latter two effects causes the Lyα emission to vary strongly with the assumed quasar spectrum. Figure 5.6 shows a zoom-in on the IF for $\alpha = 1.0, 1.5, 2.0$. The enhanced secondary ionizations of the $\alpha = 1.0$ model lead to an extended pre-ionization region. This pre-ionization is clear in Figure 5.7 where we show a zoom-in of $x_{\rm H\,I}$ around the IF for varying density and spectral index. The profile has an obvious "knee" feature with more gradual increase in $x_{\rm H\,I}$ at further distances. Because the IF Lyα emission is $\propto x_{\rm H\,I}(1 - x_{\rm H\,I})$, the stronger pre-ionization by hard ionizing spectra greatly increases the total emission. Note that the models with the same spectral index have a similar level of pre-ionization, suggesting that the effect is not limited by recombinations.

5.4.2 Inhomogeneous IGM

5.4.2.1 Cosmological simulation

To generate an inhomogeneous IGM density field, we ran a GADGET-3 simulation (Springel, 2005b) with a volume 12.5 Mpc/h on a side with 512^3 dark matter and gas particles to $z = 7.1$, the redshift of the most distant quasar published to date (Mortlock et al., 2011). The cosmological parameters were the same as assumed in the radiative transfer simulations: $\Omega_m = 0.3$, $\Omega_\Lambda = 0.7$, $\Omega_b = 0.048$, $h = 0.68$, and $\sigma_8 = 0.82$. To maximize clumping in the IGM so as to emphasize the effect of inhomogeneities on IF Lyα emission, the simulation was run without photoheating by a uniform ionizing background. For computational efficiency a temperature floor of 500 K was applied, which is compatible with some models for early

heating of the neutral IGM by X-ray sources (e.g. Furlanetto 2006, but see Fialkov et al. 2014). We then drew 100 sightlines in random directions from the most massive halo in the box with $M_h \sim 10^{11} M_\odot$. While this is likely at least an order of magnitude smaller than estimated halo masses for luminous high-redshift quasars ($M_h \sim 10^{12-13} M_\odot$; Walter et al. 2004; Fan et al. 2004; Willott et al. 2005; Fanidakis et al. 2013), the scale of the local overdensity due to such a halo is very small compared to the size scales of the ionized region after just a few Myr and thus should not significantly impact our results. In any case, we regard properly resolving the IGM structure at the small scales relevant to the IF as more important than starting from a properly-matched massive halo.

The sightlines we use were drawn at a single redshift and thus do not include dynamical evolution during radiative transfer, similar to the approach of past works (e.g. Bolton & Haehnelt 2007a). The timescale of dynamical effects due to photoheating by the quasar can be approximated as the Jeans length of the gas L_J at its initial temperature $T_{\rm cold}$ divided by the sound speed of the gas c_s at its final temperature $T_{\rm hot}$. Approximating L_J as $c_s H^{-1}$ for cold gas at the cosmic mean density, we have

$$\begin{aligned} t_{\rm dyn} &\sim \frac{L_J}{c_s} \sim \Delta^{-1/2} H^{-1} \left(\frac{T_{\rm cold}}{T_{\rm hot}} \right)^{1/2} \\ &\sim 100 \text{ Myr} \times \Delta^{-1/2} \left(\frac{T_{\rm cold}}{500 \text{K}} \right)^{1/2} \left(\frac{T_{\rm hot}}{3 \times 10^4 \text{K}} \right)^{-1/2}, \end{aligned} \tag{5.29}$$

at $z = 7.1$. This timescale is much longer than the ionization timescale of the gas inside the IF, so dynamical evolution will not significantly affect the progress of the IF through the IGM or the resulting IF Lyα emission.

We estimate the clumping factor of the simulation by computing $\langle n_{\rm H}^2 \rangle / \langle n_{\rm H} \rangle^2$ for all the sightlines combined, masking out the region within 1 Mpc of the host halo to avoid overestimating the global clumping, and find $C \sim 350$. This high clumping factor is not representative of most of the volume the IF probes in our simulations. Instead, it is dominated by rare collapsed systems with $\Delta \gg 100$. Considered individually, most of the sightlines have a clumping factor an order of magnitude smaller, closer to the $C = 35$ assumed by C08. We show later in Section 5.6 that the clumping factor is not especially relevant to the IF Lyα emission.

The results presented in the rest of the paper assume that the resolution of the simulation is sufficient to characterize density fluctuations on the (density-dependent) scale of the IF emission region. This is not a trivial assumption – the presence of significant "sub-grid" gas clumping could negate the arguments in Section 5.2 against the use of a clumping factor. Fortunately, in Section 5.6.2 we find that the following results are robust to the mass resolution and temperature floor of the simulation.

5.4.2.2 Results for individual sightlines

Figure 5.8 shows the ionization, temperature, and density for three typical density sightlines with $\dot{N}_{\rm ion} = 10^{57}$ s^{-1} and $\alpha_{\rm Q} = 1.5$ (typical of bright high-z quasars) at $t_{\rm code} = 25$ Myr. The resulting structure is not surprising – it largely resembles the uniform case described above. In detail, regions with higher density are somewhat cooler and have a higher equilibrium neutral fraction. The former is due to the effect of line cooling within the IF, as mentioned in Section 2.

A handful of sightlines encounter much higher overdensities and behave in a qualitatively different manner. The black curves in Figure 5.9 show a sightline with a $\Delta \sim 200$ overdensity that remains a substantial absorber of ionizing photons with optical depth at the H I ionizing edge $\tau_{\rm H\,I} \lesssim 1$ after the IF passes through it (a "partial" Lyman limit system; pLLS), demonstrating the effect of spectral hardening on the resulting temperature. The red curves show a sightline with a $\Delta \sim 3000$ overdensity that is optically thick and halts the IF (a Lyman limit system; LLS). Within $t_{\rm code} = 25$ Myr (corresponding to $t_{\rm LC} \sim 50$ Myr for $\theta = \pi$), we find five sightlines each encountering pLLS and LLS, suggesting that $\lesssim 10\%$ of all quasar sightlines are affected by such systems. The frequency of pLLS and LLS increases with time as the quasar radiation field is diluted, so the majority of the atypical effects occur later than $t_{\rm LC} \sim 40$ Myr.

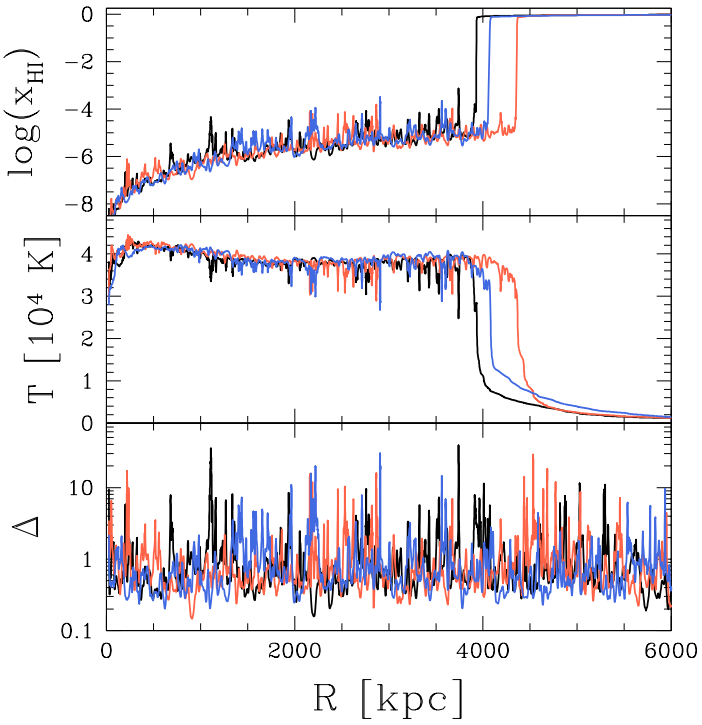

Figure 5.8: Output from the inhomogeneous RT model with $\alpha_{\rm Q} = 1.5$ and $t_{\rm code} = 25$ Myr showing neutral fraction $x_{\rm H\,I}$ (top panel), temperature T (middle panel), and density relative to the cosmic mean Δ (bottom panel). Colors indicate the three different sightlines included in this figure, which represent typical sightlines through the IGM.

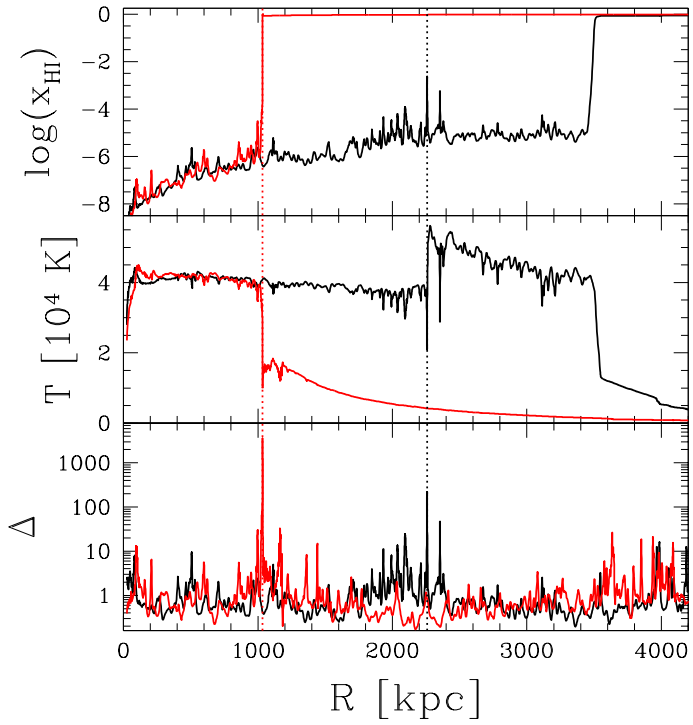

Figure 5.9: Output from the inhomogeneous RT model (see Figure 5.8) for atypical sightlines. The black curves show a sightline that encounters a overdensity which leaves behind a partially neutral absorber system with continuum optical depth at the hydrogen ionizing edge of ~ 1, located at the vertical dotted black line, while the red curves show a sightline that is halted by a LLS, located at the vertical dotted red line.

5.5 Analytic Method

The numerical method presented in the previous sections, including the full "causal correction" from Section 5.3.2, is too computationally intensive to explore the average properties of a large ensemble of sightlines with varying source parameters or to construct three-dimensional maps of Lyα emission properties in a simulation, motivating a more computationally efficient method to calculate the Lyα emission from the IF. Moreover, the input physics is straightforward enough that one should hope for a deeper physical understanding by constructing a simplified model. In this section, we describe an "analytic" model based on the discussion in Section 2 that reproduces the IF Lyα emission from the radiative transfer model to $\sim 20\%$ accuracy.

5.5.1 Basic model

As demonstrated in Section 2, the properties of the IF can be described by a handful of simple analytic expressions. First, disregarding recombinations, the propagation of an IF into a neutral homogeneous medium can be described by balancing the number of ionizing photons and neutral atoms:

$$n_{\rm H\,I} dV = \dot{N}_{\rm ion} dt, \tag{5.30}$$

which can be restated as

$$\frac{dR}{dt} = \frac{\dot{N}_{\rm ion}}{4\pi R^2 n_{\rm H\,I}}. \tag{5.31}$$

Following this expression, it is then possible to step the IF in time along a sightline with grid cells i (and corresponding physical quantities $n_{{\rm H\,I},i}, R_i, dR_i$):

$$dt_i = \frac{4\pi R_i^2 dR_i n_{{\rm H\,I},i}}{\dot{N}_{\rm ion}}. \tag{5.32}$$

This method largely reproduces the IF radius as a function of time from the full numerical model, albeit with subtle differences due to secondary ionizations that will be discussed later.

The next step is to determine the Lyα emission from the IF. To do this we follow the discussion in Section 2 and assume a simple physical picture for the IF where it is a structure

of fixed hydrogen column density $N_{\rm IF}$, $x_{\rm H\,I} = 0.5$, and effective emission temperature $T_{\rm IF}$ that is a function of the IF velocity $v_{\rm IF}$ and density. The implied Lyα surface brightness is then

$$SB_{\rm Ly\alpha} \sim \frac{1}{\pi}(1+z)^{-4}\langle\epsilon_{\rm Ly\alpha}\rangle_{\rm IF} dR_{\rm IF}, \tag{5.33}$$

where $\langle\epsilon_{\rm Ly\alpha}\rangle_{\rm IF}$, the average emissivity of Lyα photons, is

$$\langle\epsilon_{\rm Ly\alpha}\rangle_{\rm IF} \sim \frac{1}{4}\langle n_{\rm H}^2\rangle_{\rm IF} E_{\rm Ly\alpha} q_{\rm eff}(T_{\rm IF}), \tag{5.34}$$

$\langle\rangle_{\rm IF}$ denotes a spatial average within the IF, and $E_{\rm Ly\alpha} = h\nu_\alpha$ is the energy of a Lyα photon. The $1/\pi$ in the surface brightness equation comes from the Lyα emission being directed towards the observer as it escapes the optically thick IF (Gould & Weinberg, 1996), and the 1/4 in the equation for the IF emissivity comes from $x_{\rm H\,I}(1 - x_{\rm H\,I})$ assuming $x_{\rm H\,I} = 0.5$.

The simplest model for the temperature within the IF would be to assume a fixed value. In the absence of significant line cooling within the front, that would be a good approximation. However, that is in general not the case, and instead, to first order as in Section 5.2, the IF temperature can be approximated as

$$T_{\rm IF} = T_{\rm max} - \frac{2}{3}\frac{\epsilon_{\rm Ly\alpha}}{n_{\rm H} k_B} t_{\rm IF}, \tag{5.35}$$

where $T_{\rm max}$ is the maximum temperature to which the gas can be heated while the IF passes through it, which depends only on the ionizing spectrum, and $t_{\rm IF}$ is the time that a parcel of gas spends inside the IF. However, due to the highly non-linear dependence of $\epsilon_{\rm Ly\alpha}$ on temperature, this approximation breaks down quickly above overdensities of a few.

This model for the Lyα emission largely reproduces our radiative transfer results within a factor of a few and contains the most important physics for understanding the IF. However, it is possible to instead reproduce the radiative transfer results to within $\sim 20\%$ by including additional physics.

5.5.2 Advanced model

5.5.2.1 Secondary ionizations

The propagation of the IF as a function of time is not fully described by equation (5.31) above, in part due to secondary ionizations by photoelectrons. There are two dominant aspects to this. First, the effective number of ionizing photons from the source is increased due to the presence of extra ionizations close to the IF. This is evident in Figure 5.3, where the model neglecting secondary ionizations has not propagated as far (the IF is located at the steep decline near $R \sim 3$ Mpc). Second, high-energy photons "pre-ionize" the surrounding medium, decreasing the effective neutral fraction and thus letting the IF travel faster. We have found that these two effects can be modeled by writing the effective number of ionizing photons as

$$\dot{N}_{\rm ion,eff} = \dot{N}_{\rm ion,0}(1 + Xt), \tag{5.36}$$

where $\dot{N}_{\rm ion,0}$ is several percent larger than the actual value for the input source and X is a free parameter of order a few percent per 10 Myr for $\alpha_{\rm Q} = 1.5$. This simple model reproduces the size of the ionized region to nearly the spatial resolution of the input density field in most cases, once the new parameters are properly calibrated.

5.5.2.2 IF temperature

While the first order IF temperature approximation of equation (5.35) is reasonable for small R and Δ, it completely breaks down when the IF slows as it passes through $\Delta \gtrsim 10$ regions. This is because the cooling rate is a strong function of temperature (see Figure 1 of C08), so the gas within the IF will not cool indefinitely at its initial rate. Further intuition can be gained by approximating the excitation cooling rate coefficient $q_{\rm eff}$ as a power law in temperature over the relevant range and then writing down a simple form for the temperature evolution:

$$\frac{dT}{dt} \sim -\frac{2}{3}\frac{\epsilon_{\rm Ly\alpha}}{n_{\rm H} k_B} \sim -\frac{1}{6}\frac{n_{\rm H} E_{\rm Ly\alpha}}{k_B} q_{\rm eff}(T)$$

$$\sim \quad -\frac{1}{6}\frac{n_{\rm H}E_{{\rm Ly}\alpha}}{k_B}q_{\rm eff,0}\left(\frac{T}{T_{\rm max}}\right)^{\alpha_T}. \tag{5.37}$$

The resulting temperature of the IF can then be approximated by analytically integrating dT/dt over the time a parcel of gas spends within the IF, $t_{\rm IF} = dR_{\rm IF}/v_{\rm IF}$. Assuming an initial temperature $T_{\rm max}$, the solution is

$$T_{\rm IF} \approx T_{\rm max}\left(\frac{T_{\rm max}}{(\alpha_T - 1)E_{{\rm Ly}\alpha}q_{\rm eff,0}n_{\rm H}t_{\rm IF}/6k_B + T_{\rm max}}\right)^{\frac{1}{\alpha_T - 1}}. \tag{5.38}$$

For our fiducial set of simulations with $\alpha_{\rm Q} = 1.5$, we find $T_{\rm max} \sim 3.6\times10^4$ K, $q_{\rm eff,0} \sim 6\times10^{-10}$ cm^3 s^{-1}, and $\alpha_T \sim 8.6$. This best-fit power law cooling rate function is very similar in character to the input cooling rate in the radiative transfer model, suggesting that this simplified approach to cooling within the IF is a reasonable one.

5.5.2.3 Recombinations

The model described above does not account for loss of ionizing photons to recombinations within the ionized region. In most cases this will not be important because $t_{\rm rec} \gg t_{\rm LC}$. However, sufficiently dense regions ($\Delta \gtrsim 100$) can remain substantially neutral and have residual optical depths at the hydrogen ionizing edge of order unity or higher (see Section 5.4.2.2). The IF beyond these regions will then proceed more slowly. We include this effect by reducing the number of ionizing photons available to expand the ionized region by the number of recombinations along the sightline,

$$\dot{N}_{\rm rec} = \int_0^{R_{\rm IF}} \alpha^A_{\rm H\,II} n_{\rm H}^2 4\pi r^2 dr, \tag{5.39}$$

where $\alpha^A_{\rm H\,II}$ is the case A recombination coefficient and we assume the ionized region has $x_{\rm H\,II} \approx 1$. The temperature of the ionized gas is assumed to be $T_{\rm final} = T_{\rm IF} + T_{\rm He\,III}$ where $T_{\rm He\,III} = 7000 \times (1.5/\alpha_{\rm Q})$ K is an approximation of the additional heating due to the second ionization of helium based on the results of the radiative transfer model. This approximation for the IGM temperature is very rough, however, as the gas in the full simulation does not remain at a fixed temperature but instead cools due to adiabatic and inverse Compton cooling. Fortunately, the recombination rate is not an especially strong function of temperature,

Table 5.1: List of best-fit analytic model parameters for different quasar spectrum power law indices $\alpha_{\rm Q}$.

$\alpha_{\rm Q}$	$N_{\rm IF}{}^a$	$\dot{N}_{\rm ion,0}/\dot{N}_{\rm input}$	X	$T_{\rm max}{}^b$	$q_{\rm eff,0}{}^c$	α_T
1.3	8.06	1.115	0.052	4.22	13.39	7.92
1.4	6.20	1.086	0.040	3.88	8.91	8.13
1.5	4.96	1.056	0.033	3.57	6.24	8.59
1.6	3.96	1.030	0.027	3.34	4.60	9.05
1.7	3.29	1.004	0.024	3.10	2.63	9.00
1.8	2.87	0.983	0.017	2.92	1.68	9.04

[a] 10^{18} cm^{-2}

[b] 10^4 K

[c] 10^{-10} cm^3 s^{-1}

so the approximation is not a particularly bad one. Some of the systematic error in the recombination rate correction to the propagation of the IF is corrected by calibrating the X factor described in Section 5.5.2.1.

5.5.3 Calibrating fit parameters

The final analytic model has six free parameters, $\{N_{\rm IF}, \dot{N}_{\rm ion,0}, X, q_{\rm eff,0}, T_{\rm max}, \alpha_T\}$, and we find the best fit set of parameters by minimizing the squared residuals of $SB_{\rm Ly\alpha}(t)$ compared to the radiative transfer model over a set of ten sightlines which represent typical density field structure in the IGM. In Table 5.1 we list the best fit parameters for radiative transfer models with varying quasar spectrum, where the $\alpha_{\rm Q} = 1.5$ model is our fiducial one.

5.5.4 Comparison to radiative transfer results

Figure 5.10 compares the analytic model to the radiative transfer model for a representative sightline. $T_{\rm IF}$ is the temperature of the gas in the center of the IF, where $x_{\rm H\,I} \sim 0.5$, while $dR_{\rm IF}$ is its width. In the radiative transfer simulations, we define $T_{\rm IF}$ as the temperature of the first grid cell from the origin with $x_{\rm H\,I} > 0.5$ and $dR_{\rm IF}$ as the distance between cells

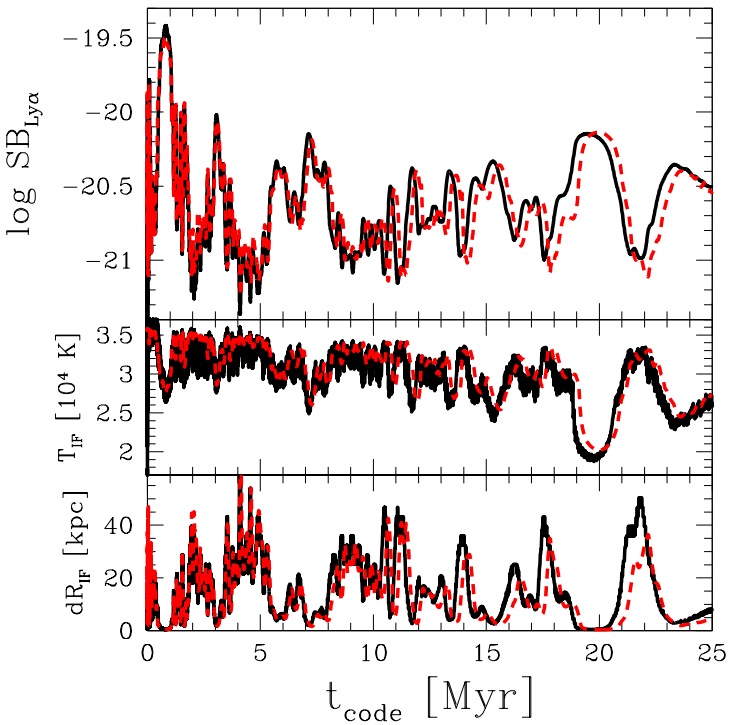

Figure 5.10: Comparison between the radiative transfer model (solid black) and analytic model (dashed red) with no causal correction applied. Upper panel: plane-parallel Lyα surface brightness. Middle panel: temperature within the IF. Bottom panel: width of the IF.

with $x_{\rm HI} = 0.05$ and $x_{\rm HI} = 0.75$. These simple definitions were chosen to act as rough approximations to the general properties of the IF and they are not meant to be exact. The analytic model simultaneously matches the surface brightness, IF temperature, and IF width very well. However, some slight deviations remain, such as a slight inaccuracy in $R_{\rm IF}(t)$ and the dip in $SB_{\rm Ly\alpha}$ at $t_{\rm code} \sim 19$ Myr. This dip is due to the pre-ionization region (Section 5.4.1.1) extending into relatively high density gas, which causes a small excess of Lyα emission relative to the analytic model.

The analytic model was calibrated to $t_{\rm code} = 25$ Myr output from the radiative transfer model (corresponding to $t_{\rm LC} \sim 40$ Myr), and thus it does not match as well at later times. Specifically, by comparing to a 100 Myr radiative transfer simulation, equation (5.36) becomes a poor approximation to the effective number of ionizing photons after $t_{\rm code} \sim 40$ Myr.

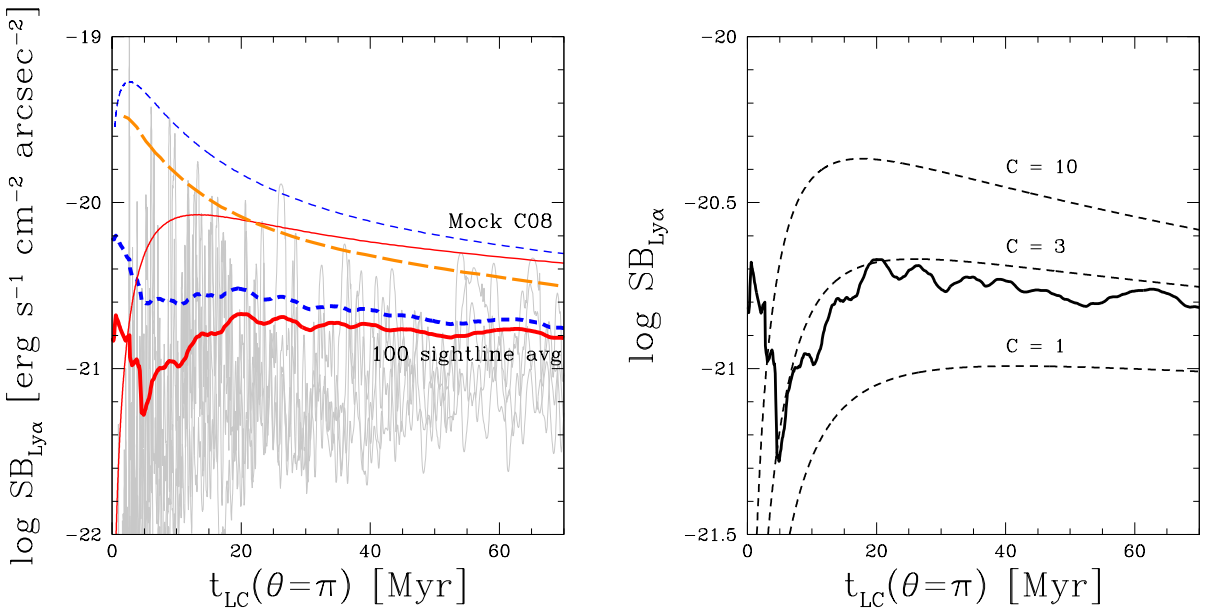

Figure 5.11: *Left*: Plane-parallel Lyα surface brightness for 10 individual sightlines (thin gray curves) and a 4 Myr top-hat smoothed average of all 100 sightlines (thick curves) with or without the causal intensity correction (solid and short-dashed, respectively) compared to the model prediction from C08 scaled to $z = 7.1$ (long-dashed curve) and our calculation using the C08 input parameters (upper thin curves). *Right*: Dashed curves show the predicted Lyα surface brightness for the uniform model calculation assuming different values of the clumping factor ($C = 1, 3, 10$ from bottom to top) compared to the inhomogeneous IGM average (solid curve). Note the different scale on the vertical axis from the left panel.

Similarly, the recombination rate assumes a constant IGM temperature, but in the radiative transfer model the gas continues to cool after the ionization of He II, slowly increasing the true recombination rate relative to the approximation in Section 5.5.2.3.

Another limitation involves the effect of secondary ionizations on the IF with a hard source spectrum. For relatively hard source spectra, the pre-ionization region ahead of the IF becomes an important source of Lyα photons. Additionally, the assumption of a constant density within the IF becomes less valid because the wider IF will encompass a range of densities. Finally, the analytic model assumes a single power law for the effective cooling rate as a function of temperature, which is not a good assumption at the higher temperatures inside the IF of a hard spectrum source. We find that the analytic model no longer provides a reasonable approximation to the surface brightness for $\alpha_{\rm Q} \lesssim 1.3$.

The analytic model ignores the gradual hardening of the spectrum reaching the IF due to absorption of ionizing photons by residual neutral atoms within the ionized region. This hardening broadens the IF slightly over time and change the balance of heating and cooling, causing the analytic model to drift from the radiative transfer model increasingly over time. However, this deviation is only at the few percent level after $t_{\rm code} \sim 50$ Myr ($t_{\rm LC} \sim 90$ Myr), so it may be unimportant if the extremely luminous quasar phase is limited to a few tens of Myr (e.g. Trainor & Steidel 2013).

We find that the analytic model is a reasonable approximation to the RT model for $\alpha_{\rm Q} \gtrsim 1.3$ and $t_{\rm LC} \lesssim 75$ Myr, and for the "typical" 90% of sightlines that do not encounter optically thick absorbers as described in Section 5.4.2.2. For the remaining $\sim 10\%$ of sightlines, the analytic model fails to accurately reproduce the Lyα emission. For sightlines that encounter a pLLS, this amounts to a systematic underestimate of the IF emission inside and beyond the absorbing system by a factor $\lesssim 2$. We find that this bias does not have a significant effect on the time-averaged IF emission of the entire ensemble of sightlines because of the relative rarity of such systems. Sightlines that encounter a LLS, despite being much brighter than the average IF signal, likely do not contribute much to the IF emission because the emission is rapidly displaced in velocity space from the rest of the IF on a timescale of a few Myr.

5.5.5 Causal correction in the analytic model

After calibrating the analytic model to reproduce the infinite speed of light radiative transfer results, we applied the causal correction described in Section 5.3.2 by transforming each dt_i in equation (5.32) to its counterpart $dt_{\mathrm{LC},i}$ observed on the light cone with

$$dt_{\mathrm{LC},i} = dt_i(1 + \frac{dR/dt}{c}(1 - \cos\theta)), \tag{5.40}$$

as in equation (5.20), and correcting the output surface brightness following equation (5.24),

$$SB_{\mathrm{Ly}\alpha} \rightarrow SB_{\mathrm{Ly}\alpha}\left(1 + \frac{dR/dt}{c}(1 - \cos\theta)\right)^{-1}. \tag{5.41}$$

As discussed in Section 5.3.2, for our main results we do not apply the causal correction directly to the output of the radiative transfer model due to its much more stringent requirements on spatial and temporal resolution. We have confirmed with small scale tests that the above corrections to the time steps and surface brightness are equivalent to applying the coordinate transformation in equation (5.19) directly to the radiative transfer model, albeit at much smaller computational expense.

5.6 Lyα Surface Brightness

An accurate determination of the observable properties of the IF Lyα emission will depend sensitively on the detailed Lyα radiative transfer both out of the IF and within the ionized region close to the quasar. However, these processes only serve to disperse Lyα photons out of the line of sight, so a robust upper limit on the Lyα surface brightness can be found by assuming a plane-parallel geometry. That is, assuming that the IF behind the quasar is an optically thick slab, the emergent intensity is (Gould & Weinberg 1996, C08)

$$I_{\mathrm{Ly}\alpha} \approx \frac{1}{\pi}\int_{\mathrm{IF}} \epsilon_{\mathrm{Ly}\alpha} dR, \tag{5.42}$$

corresponding to an observed surface brightness $SB_{\mathrm{Ly}\alpha} = I_{\mathrm{Ly}\alpha}(1+z)^{-4}$. The overall redshift dependence of the surface brightness will be substantially weaker than $(1+z)^{-4}$ because of the dependence of $I_{\mathrm{Ly}\alpha}$ on physical density and temperature inside the IF. Ignoring the temperature dependence of the emission, we have $\epsilon_{\mathrm{Ly}\alpha} \propto n_{\mathrm{H}}^2$ and $dR_{\mathrm{IF}} \propto n_{\mathrm{H}}^{-1}$, so $I_{\mathrm{Ly}\alpha} \propto (1+z)^3$,

leading to a surface brightness that scales as $\propto (1+z)^{-1}$. In detail, the redshift dependence depends on the evolving structure of the density field and the physical density dependence of the cooling that strongly regulates the IF emission and is not trivial to determine. In the case of a uniform medium with clumping factor $C = 35$, C08 found that $SB_{\mathrm{Ly}\alpha} \propto (1+z)^{-2}$, and we find a similar scaling applies to our calculations as well.

There are several effects that this simple plane-parallel picture ignores. We have assumed that, because of the neutral hydrogen gradient within the IF, Lyα photons will preferentially escape towards the source with zero photons escaping in the IF propagation direction (Gould & Weinberg, 1996). The emission may be emitted more isotropically when the IF is moving at relativistic speeds and scattered by residual neutral hydrogen in the ionized region, leading to suppression by up to a factor of four (C08). Also, the effective area of a given IF shell segment will depend on the angle from the line of sight through projection of the emitting surface, which is non-trivial in the clumpy IGM. Finally, Lyα photons emitted from the IF may be scattered by the foreground neutral IGM if they have not had a long enough path length to redshift out of line center (Miralda-Escudé, 1998b). For a photon emitted from the IF behind the quasar, the path length will be given by the sum of the causally corrected IF radius and the uncorrected IF radius. We find that the IGM damping wing absorption could suppress the Lyα emission by $\sim$ 15–35% for $5 < t_{\mathrm{LC}} < 30$ Myr, significantly larger than suggested by C08[6] but still not especially severe.

We ignore these effects in the following discussion and focus on the plane-parallel estimate of the surface brightness which is almost certainly an *overestimate* of the true emission. In the next section we will find that even this optimistic overestimate is significantly fainter than previously predicted and is likely inaccessible to current telescopes, making further modeling less interesting.

[6]It appears Cantalupo et al. (2008) "double-counted" the light-travel distance from the far side of the ionized region to the near side; the causality-corrected shape of the ionized region already reflects the light-travel distance by definition (Yu, 2005).

5.6.1 Results

In the left panel of Figure 5.11 we compare our plane-parallel surface brightness calculation to the similar model from C08 for Lyα emission from behind the quasar ($\theta = \pi$). The rapidly varying thin curves show the effective $SB_{\mathrm{Ly}\alpha}$ as a function of time for ten of the 100 sightlines. However, those $SB_{\mathrm{Ly}\alpha}(t)$ are not representative of the emission averaged on large scales, as one would hope to measure. To approximate an observation that would average over the density field structure in 3D, the thick curves in Figure 5.11 show a 4 Myr top-hat smoothed average of all 100 sightlines, with (solid) and without (dashed) the causal correction to the IF Lyα intensity from equation (5.24). Our resulting Lyα surface brightness is substantially lower than the C08 model (long-dashed curve) scaled to $z = 7.1$ by $SB_{\mathrm{Ly}\alpha} \propto (1+z)^{-2}$ (C08). The short-dashed curves in the right panel of Figure 5.11 show uniform density models with varying clumping factor. By comparing the uniform density models to the inhomogeneous model, we find the "effective" clumping factor of the inhomogeneous IGM, as probed by the Lyα emission, to be $C_{\mathrm{eff}} \sim 2.5$, compared to $C \sim 350$ for the density field. The enhancement in the Lyα emission at $t \lesssim 5$ Myr is due to the local overdensity of the host halo and has been broadened by the smoothing. The timescale over which the emission is enhanced by the host halo is ~ 2 Myr, corresponding to a local overdensity scale of ~ 300 kpc.

The low effective clumping factor relative to the density field is the result of a combination of several effects acting to increase and decrease the n_{H}^2 boost from a clumpy IGM. As discussed previously, the thinness of the IF relative to the scale of density fluctuations causes the Lyα emission to vary proportionally to n_{H} instead of n_{H}^2. The extra cooling in dense regions further weakens the dependence on n_{H}. However, ignoring causal effects, the IF will typically spend more time inside of dense regions because they take longer to ionize. On the other hand, the causal correction reduces the IF velocity more strongly within underdense regions, which increases their contribution relative to dense regions where v_{IF} is smaller relative to c.

We have also computed $SB_{\mathrm{Ly}\alpha}$ using the same input parameters as C08 ($\alpha_{\mathrm{Q}} = 1.7$, $C = 35$, no secondary ionizations) to directly compare the differences between our methods,

shown by the thin curves at the top of Figure 5.11 where the solid and dashed curves are with and without the causal correction, respectively. The dashed curve is directly comparable to the long-dashed curve from C08, while the solid curve shows the additional effect of the causal correction on $SB_{\mathrm{Ly}\alpha}$ that we have highlighted. Interestingly, our (intensity uncorrected) model predicts Lyα emission enhanced by a constant factor of ~ 2 relative to C08. C08 did not include soft X-ray radiation in their simulations, which may cause their IF to be narrower and reduce the heat input into the IGM, especially in the regions beyond the IF (compare Figure 5 of C08 to Figure 5.1 in this work). Because the collisional excitation rate is such a strong function of temperature (see Figure 1 of C08), only a modest $\sim 10\%$ difference in IF temperature is enough to fully account for the discrepancy.

In Figure 5.12, we compare the predicted plane-parallel surface brightness for a range of input quasar spectra with varying power law index and fixed $\dot{N}_{\mathrm{ion}}$. Like C08, we find that the surface brightness is sensitive to the quasar ionizing spectrum. This sensitivity is due to a combination of changes in the IF width and the IF temperature, which act together to increase or decrease the Lyα emission. While the analytic model is not applicable to quasar spectra with $\alpha_{\mathrm{Q}} \lesssim 1.3$, we can still estimate the effect of a harder spectrum with the radiative transfer code. We find that for $\alpha_{\mathrm{Q}} = 1.0$ (0.5) the total Lyα emission is roughly 6 (20) times brighter than our fiducial $\alpha_{\mathrm{Q}} = 1.5$ case.

By computing the Lyα emission from cosmological simulation sightlines at higher redshifts, we find that, in agreement with C08, the surface brightness scales as $(1+z)^{-2}$. However, due to the causal correction factor dependence on IF velocity, the relationship between surface brightness and $\dot{N}_{\mathrm{ion}}$ is no longer one-to-one. Without this velocity dependent correction, the dominant effect of $\dot{N}_{\mathrm{ion}}$ is on the cooling within the IF: larger $\dot{N}_{\mathrm{ion}}$ means less time spent within the IF which means less cooling, and vice versa. In our model this effect is largely neutralized by the causal correction factor. When $\dot{N}_{\mathrm{ion}}$ is larger the IF is somewhat hotter and thus more luminous, but it is also moving faster relative to c so the Lyα intensity is diminished. Figure 5.13 demonstrates this effect over the range 10^{56} s^{-1} $< \dot{N}_{\mathrm{ion}} <$ 10^{58} s^{-1}. Note, however, that while a fainter source may be somewhat brighter at quasar-relevant timescales ($t_{\mathrm{LC}} \sim 10$ Myr), the emission will cover a smaller region on the sky and experience

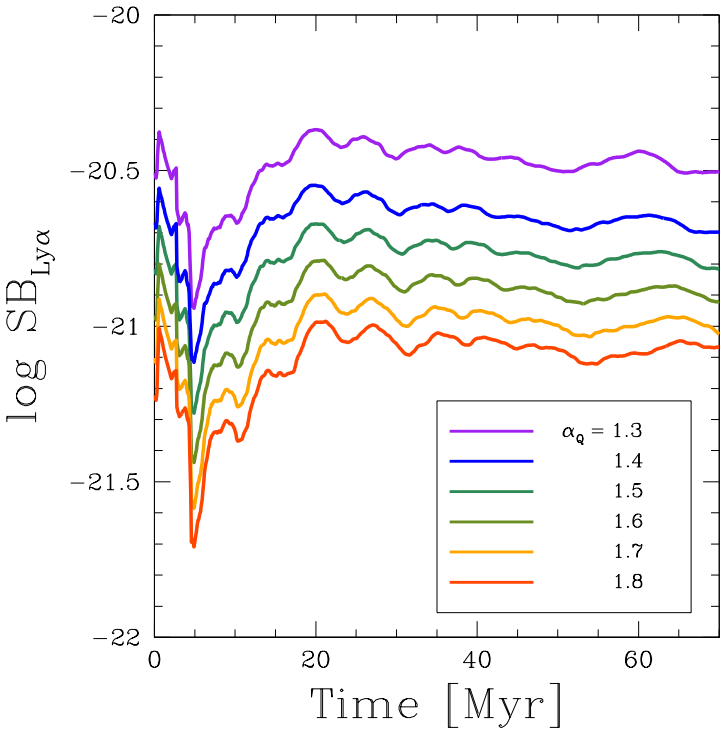

Figure 5.12: Plane-parallel Lyα surface brightness for a 4 Myr top-hat smoothed average of all 100 sightlines for a range of different quasar spectra with power law indices of $\alpha_{\rm Q} = 1.3, 1.4, 1.5, 1.6, 1.7, 1.8$ from top to bottom with fixed $\dot{N}_{\rm ion}$.

enhanced IGM damping wing absorption due to the smaller size of its ionized region, so they may not provide a more promising target for observations.

While our model does not include Lyα radiative transfer and thus cannot make specific predictions about the velocity structure of the emission, one possible contributor is the distribution of Hubble flow velocities across the IF Lyα -emitting surface. That is, the "lumpiness" of the IF due to inhomogeneities influencing the IF velocity could broaden the IF emission in velocity space. The solid and short-dashed curves in Figure 5.14 show the 16-84% and 2.5-97.5% widths of the Lyα emission profile in velocity space due to the Hubble flow relative to the Lyα brightness-weighted mean velocity, ignoring the intrinsic line width and without any temporal smoothing. By $t_{\rm LC} \sim$ 10–20 Myr, the lumpy nature of the IF can broaden the emission profile by $\gtrsim 100$ km/s, similar to the expected intrinsic line width (C08). Observations of a small field behind the quasar would likely see a smaller velocity width due to correlations in the density field.

Another contributor to the line width is the shift in central velocity due to curvature of the IF across the field of view of a hypothetical observation. Because the IF Lyα emission is quite weak, detection would likely require integration over $\gtrsim 1$ arcmin^2. The long-dashed curve in Figure 5.14 shows the Hubble flow velocity difference between the IF directly behind the quasar and the IF 50 arcseconds away, approximating the shape of the ionized region as spherical.[7] At $z \sim 7$, 50 arcseconds corresponds to ~ 0.25 Mpc. At $t_{\rm LC} \sim 10$ Myr, the radius of the ionized region along the light cone behind the source is typically ~ 1.5 Mpc, so this represents a small but not negligible fraction of the IF surface. As demonstrated in Figure 5.14, the curvature of the IF is likely to be unimportant compared to the lumpy structure except at early times ($t_{\rm LC} \lesssim 10$ Myr) or for observations covering a larger field of view.

5.6.2 Is sub-grid clumping important?

The analysis above assumes that our cosmological simulation provides an accurate representation of neutral gas clumping in the IGM on the scale of the IF. With a gas particle

[7]Observation of the IF along the light cone flattens the apparent shape of the ionized region behind the source (Yu, 2005), so a spherical approximation mildly overestimates the velocity shift.

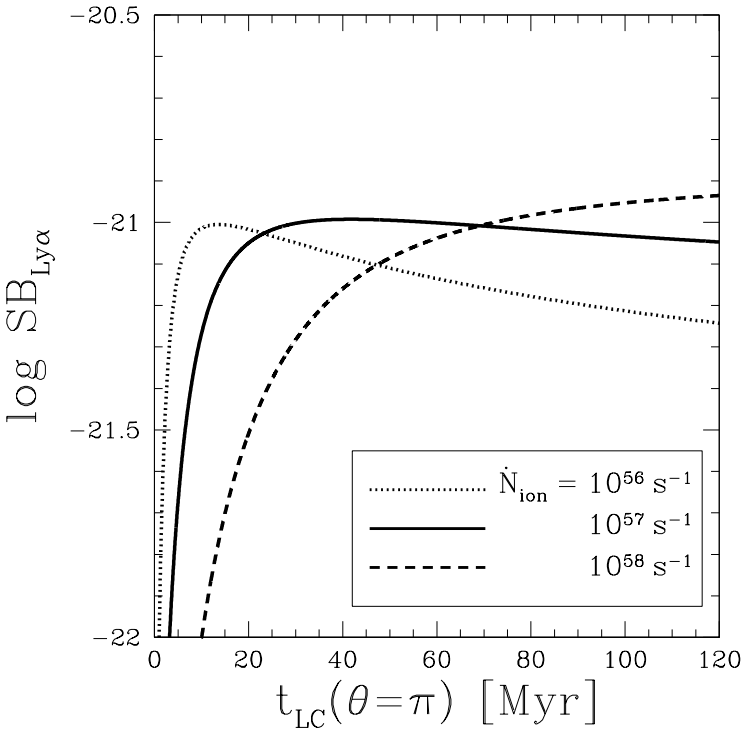

Figure 5.13: Lyα surface brightness in the uniform model (with $C = 1$) for varying quasar ionizing luminosities. The higher luminosity source is brighter at late times, but suffers from an enhanced causal correction at early times.

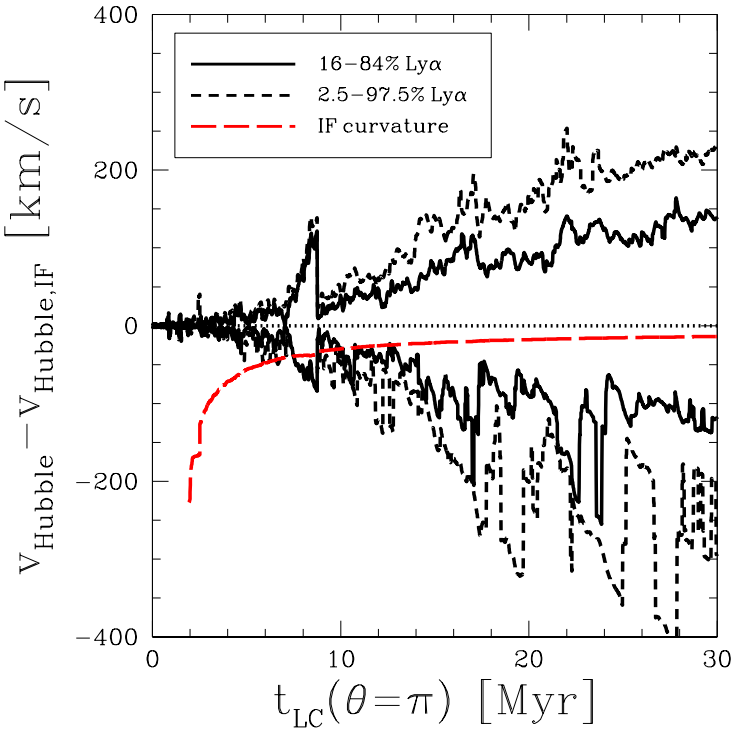

Figure 5.14: Velocity width of IF Lyα emission due to the spread in Hubble flow velocities of the IF. Solid and short-dashed curves show the width of the central 16-84% and 2.5-97.5% of the total Lyα emission, respectively, neglecting the intrinsic line width. The long-dashed curve shows the velocity shift due to curvature of the IF at 50 arcseconds away from the quasar on the sky. The zero-point is set by the Hubble flow velocity of the IF.

mass of $\sim 10^6$ $M_\odot$, our simulation should resolve the Jeans mass of 500 K neutral gas at the mean density, $M_J \sim 5 \times 10^7$ $M_\odot$. Although 500 K is a very reasonable temperature estimate for the IGM at $z \sim 7$ and is below several models (e.g., Furlanetto 2006; Pritchard & Loeb 2010), the lack of constraints on IGM heating at very high redshifts may mean that it is an overestimate, which would allow for clumping on even smaller scales. If substantial clumping existed on scales much smaller than the IF, the arguments in Section 5.2 against the use of the clumping factor would no longer hold, and the expected Lyα emission could increase.

To investigate the potential effect of enhanced clumping on our results, we ran an additional cosmological simulation (with the same cosmology) in a volume 3 Mpc/h on a side with a minimum temperature of 50 K, compared to 12.5 Mpc/h and 500 K, respectively, for the fiducial simulation. We then drew 50 randomly-placed sightlines through the density field and performed the same analysis as described in the previous section to calculate the expected Lyα surface brightness. Despite the significantly enhanced clumping compared to the fiducial simulation, the time-averaged Lyα surface brightness is nearly identical to Figure 5.11.

While the IF in the second simulation is larger than the Jeans length of $\Delta = 1$ gas, most of the time-averaged Lyα emission comes from modestly overdense regions with $\Delta \gtrsim 5$. Because the IF width scales more strongly with density than the Jeans length, $dR_{\rm IF} \propto \Delta^{-1}$ versus $L_J \propto \Delta^{-1/2}$, it is relatively easy for the IF to resolve density fluctuations in overdense regions. The Jeans length of 50 K (500 K) neutral gas at $z \sim 7$ is roughly equal to the IF width for $\Delta \sim 6$ (2), so fluctuations in the density field above this threshold will be resolved by the IF. More quantitatively, one can estimate the relevant sub-IF-scale clumping factor,

$$C_{\rm IF} = \frac{\frac{1}{dR_{\rm IF}} \int_{\rm IF} n_{\rm H}^2 dR}{\left(\frac{1}{dR_{\rm IF}} \int_{\rm IF} n_{\rm H} dR\right)^2}, \tag{5.43}$$

along a sightline through the density field, where the integration over the IF (and $dR_{\rm IF}$) is defined by a region with column density $N_{\rm IF}$ as in the analytic model of Section 5.5. Averaged over the sightlines, we find $C_{\rm IF} \sim 1.1$ and ~ 1.4 for the fiducial 500 K simulation and 50 K simulation, respectively, showing that clumping below the IF *column density* scale is unimportant even in an IGM significantly colder than expected. The highest $C_{\rm IF}$ values in

the 50 K simulation are found at the edges of dense regions where there is a strong gradient in the density field. $C_{\rm IF} \approx 1$ inside the dense regions that contribute most of the Lyα emission, so the effect of the spatially averaged value on the total emission is small.

5.6.3 Discussion

The Lyα emission predicted by our model, even in the absence of Lyα radiative transfer, is a factor of 3–15 weaker than that predicted by C08 for quasar ages $\lesssim 30$ Myr. This difference comes about due to two effects that were not considered in C08. First, the global clumping factor of a simulation does not describe the enhancement of Lyα emission from density fluctuations, as described in Section 5.2. Second, while they included a causal correction factor to propagate the IF at the correct speed, they did not consider the effect of this causal correction on the intensity of the Lyα emission (Section 5.3.2). As discussed in Miralda-Escudé & Rees (1994), relativistic IFs are narrower than their non-relativistic counterparts, with a width of roughly the speed of light times the ionization timescale $t_{\rm ion} \sim \Gamma^{-1}$ instead of the typical optical depth criterion. This further decreases the emission at early times.

Our less optimistic prediction for IF Lyα emission calls its detectability with current and future instruments into question. The results in the previous section ignored Lyα radiative transfer effects which decrease the observable emission by scattering Lyα photons out of the line of sight. C08 found that these effects amounted to a factor of 0.58 correction to the plane-parallel calculation, predominantly due to scattering by residual neutral hydrogen inside the ionized region. They also found that the relativistic motion of the IF could reduce the emission by another factor of ~ 2. Thus, our simplified calculation likely overestimates the Lyα surface brightness by a factor of ~ 2–4. Keeping this limitation in mind, our fiducial value for the observable Lyα surface brightness is 10^{-21} erg s^{-1} cm^{-2} arcsec^{-2}. The expected signal-to-noise ratio (S/N) for an observation of a $z = 7.1$ quasar field is

$$\begin{aligned} \mathrm{S/N} \;\sim\; & 0.35\, C_f SB_{-21} \left(\frac{D}{10\ \mathrm{m}}\right) \left(\frac{\zeta}{1.0}\right) \left(\frac{f}{0.25}\right)^{\frac{1}{2}} \left(\frac{\Delta\lambda}{3\ \text{Å}}\right)^{-\frac{1}{2}} \\ & \times \left(\frac{t_{\rm obs}}{40\ \mathrm{hr}}\right)^{\frac{1}{2}} \left(\frac{\Delta\Omega}{600\ \mathrm{arcsec}^2}\right)^{\frac{1}{2}}, \end{aligned} \tag{5.44}$$

where C_f is the covering factor of neutral IGM within the field of view, SB_{-21} is the Lyα surface brightness in units of 10^{-21} erg s^{-1} cm^{-2} arcsec^{-2}, D is the diameter of the telescope, ζ is the atmospheric transmission, f is the system efficiency, $\Delta\lambda$ is the spectral bin (3 Å $\sim$ 100 km/s), $t_{\rm obs}$ is the integration time, and $\Delta\Omega$ is the observed area of the sky. The various parameters have been chosen to mimic an observation with the upcoming Keck Cosmic Web Imager (KCWI; Martin et al. 2010) assuming perfect sky subtraction and noise dominated by shot noise of the typical sky background between sky lines on Mauna Kea[8]. This low S/N is in spite of the cold, clumpy IGM from the hydrodynamic simulations which should overestimate the emission. Similar observations with a future ground-based large aperture instrument such as the Thirty Meter Telescope (TMT) could only achieve S/N $\sim$ 1.

An alternative observing approach would be to attempt a narrowband photometric detection over a wider area. The potential scale of the Lyα emission on the sky is a few arcmin^2, so the relevant $\Delta\Omega$ can in principle be much larger than the field of view of KCWI or similar spectrographic instruments. In that case, for $\Delta\lambda = 75$ Å, $f = 0.5$, and $\Delta\Omega = 4$ arcmin^2 in equation (5.44), we find S/N $\sim 0.5\ C_f$, which is only a marginal improvement if C_f is comparable between the two cases.

The sky background at 1 μm from the ground is dominated by atmospheric emission (e.g. Sullivan & Simcoe 2012), so improved S/N could potentially be achieved by observing from space. Above the Earth's atmosphere, the background is dominated by zodiacal light which can be minimized by observing a target at high ecliptic latitude. For example, the zodiacal light at 1 μm near the north ecliptic pole is roughly a factor of 20 smaller than the sky background assumed in equation (5.44) (Giavalisco et al., 2002). This means that a space-based observation could potentially gain a factor of $\sim$ 4.5 in S/N, though almost certainly at the expense of telescope diameter.

If quasar IF Lyα emission were detected by future instruments, the brightness would provide a joint constraint on the temperature of the IF (i.e. the shape of the quasar ionizing spectrum) and neutral fraction of the IGM. Additionally, the redshift of the Lyα line would

[8]http://www.gemini.edu/sciops/telescopes-and-sites/observing-condition-constraints/ir-background-spectra

indicate the current size of the quasar ionized region, placing a constraint on the total number of ionizing photons emitted by the quasar. Maps of this emission would allow study of the tomography of reionization – regions that were initially neutral will light up, while previously ionized regions will remain dark (C08). However, given the low expected S/N, this seems unlikely to be achieved in the near future. Based on our calculations, a detection of this faint Lyα emission would require a high degree of IGM clumping on scales smaller than the IF, a hard quasar ionizing spectrum, or some combination of the two. Our investigation of enhanced clumping with a simulation of a colder IGM in the previous section suggests that the former is unlikely. As for the latter, for a S/N $\gtrsim 5$ detection with a thirty-meter-class telescope in 40 hours the target quasar must have $\alpha_{\rm Q} \lesssim 1$, ignoring any additional Lyα radiative transfer effects due to the much wider IFs.

Five of the 100 sightlines we considered encountered optically thick absorbers, LLS, within $t_{\rm LC} \lesssim 40$ Myr. Once the IF reaches the LLS overdensity ($\Delta \gtrsim 1000$), the Lyα surface brightness plateaus as the IF becomes a stationary ionized "skin" on the surface. The Lyα surface brightness varies with LLS distance from the quasar as $R_{\rm LLS}^{-2}$, as one would expect for the "reflection" of a fixed fraction of the incoming ionizing radiation towards the observer (Gould & Weinberg, 1996). While the surface brightness of the LLSs is much higher than expected for the IF as a whole ($SB_{\rm LLS} \sim 10^{-19}[R_{\rm LLS}/1.4\ {\rm Mpc}]^{-2}$ erg s^{-1} cm^{-2} arcsec^{-2}), the physical size of the associated density peak is only a few kpc across corresponding to $\lesssim 1$ arcsec^{-2}. This could provide a modest boost to the integrated IF emission, but as static features they will be separated in velocity space from the rest of the IF fairly quickly. We stress that this is unlikely to be a very accurate description of the emission from optically thick systems because we do not consider the hydrodynamical effects of photoionization heating (e.g. evaporation). These systems are analogous to fluorescent Lyα emission at lower redshift when the universe is fully ionized (e.g. Cantalupo et al. 2012; Trainor & Steidel 2013), and thus do not seem to be a compelling probe of the reionization process. However, detection of such systems may allow an independent constraint on the number of optically thick absorbers at high redshift and thus the mean free path of ionizing photons.

In Section 5.3.1 we mentioned that the contribution to the Lyα emission directly from

energetic photoelectrons was usually sub-dominant to the IF emission. Photoelectron excitation of H I atoms is largely confined to neutral gas beyond the IF, corresponding to the region between $R_{\rm IF}$ and $R = ct_{\rm LC}$, requiring a high-resolution fully causal-corrected model (via equation 5.19) in order to make accurate predictions of its intensity. We discuss the results of a small number of such models in the following. At early times this region is small enough to mimic the narrow velocity Lyα emission from the IF, but that narrowing also leads to a faint surface brightness on the sky. Additionally, the loss timescale effect mentioned in Section 5.3.1 plays a critical role in suppressing the emission at early times – the time between the gas illumination by X-rays and when it is ionized can be very short. At later times, the Lyα emission comes from a very broad shell outside of the ionized region, and we find that it is weaker than the IF Lyα emission by a factor of a few. In contrast to the IF emission, the emission by secondary electrons is proportional only to Δ instead of Δ^2, and thus it is unaffected by clumping of gas.

Due to the computational speed of the analytic model, one may envision a method to generate maps of the IF Lyα emission by drawing rays through a three-dimensional cosmological density field. Such a technique would undoubtedly be faster than performing the relativistic ionizing radiative transfer that would otherwise be necessary. We neglected to pursue this further because the expected signal is too weak.

5.7 Conclusion

In this work we have explored the physics of Lyα emission from quasar ionization fronts in an inhomogeneous IGM. Our radiative transfer modeling includes much of the relevant physics and resolves the heating, cooling, and ionization structure of the IF as it passes through a varying density field. In an improvement over past work, we include the effect of secondary ionizations by high-energy photoelectrons and properly account for causality in our infinite speed-of-light simulations. We have developed a relatively simple analytic framework that allows for rapid computation of Lyα emission along a sightline through the IGM, and we applied this model to a ensemble of 100 sightlines through a hydrodynamic

simulation. The resulting average surface brightness is a factor of 3–15 fainter than the prediction by C08, reflecting both the smaller effective clumping factor of the Lyα emission and causal suppression due to the near-relativistic expansion at quasar relevant timescales ($5 \lesssim t_{\rm LC} \lesssim 30$ Myr).

Our analysis assumes that the light from the quasar reaches a completely neutral region of the IGM within its lifetime. This may be unlikely during reionization because the presence of a luminous quasar indicates a biased region of the Universe which will likely be ionized early (Alvarez & Abel, 2007; Lidz et al., 2007). In a more realistic scenario where the quasar light does not reach neutral gas for $\gtrsim 5$ Mpc, the Lyα emission would not "switch on" until the neutral gas is illuminated along the light cone ($t_{\rm LC} \gtrsim 30$ Myr). Additionally, the lack of pre-heating by hard ionizing photons could reduce the emission somewhat. Thus, our results should be seen as optimistic.

There may be other significant sources of line photons at the very faint level of our prediction for the IF Lyα signal. For example, scattering of non-ionizing quasar photons from the damping wing of the neutral IGM (Loeb & Rybicki, 1999) could be brighter than the IF Lyα signal. In that case, a narrowband detection of extended emission would not necessarily indicate the presence of an IF, although one could still infer the presence of the neutral IGM. The Loeb-Rybicki halo emission would be much broader in velocity space ($\Delta v \gtrsim 1000$ km/s), so a spectral observation could in principle disentangle the two.

Analogous to the H I IFs considered here, one might also expect He II Lyα emission from He II IFs during helium reionization at $z \sim 3$. He II IFs are relatively broad ($dR_{\rm IF} \sim 1$ pMpc; Furlanetto & Oh 2008) so in principle the IF emission could be brighter. However, He II resonance lines require four times as much energy to excite relative to H I, so the temperature within the IF is not high enough to produce any significant emission.

The detection of Lyα emission from a quasar ionization front would be "smoking gun" evidence of the reionization process (and potentially a useful diagnostic of quasar properties). Unfortunately, we have found that the largest existing telescopes fall far short of detecting our predicted signal. Even the next generation of thirty-meter class near-infrared telescopes

will struggle mightily to detect these ionization fronts at any reasonable significance; measurements will require quasars with very hard spectra in relatively neutral environments and extremely long integrations. The smaller background in space makes a satellite observation easier, but collecting area will likely be a major problem. Nevertheless, should the proper target quasar appear, this is an extremely powerful probe of the reionization epoch.

CHAPTER 6

Conclusion

In summary, I have constructed new models of the ionizing background that include, for the first time, the effect of fluctuations in the mean free path of ionizing photons. These models compare quite favorably to observations of the hydrogen and helium Lyα forests at $z \sim 5.6$ and $z \sim 3$ respectively, where the standard uniform background (and uniform mean free path) models fail. Both models serve as the groundwork for future studies of the properties of ionizing sources, such as quasar lifetimes and the bias of ionizing radiation. I have also re-investigated the potential of quasar ionization front Lyα emission as a probe of the topology of ionized regions during the epoch of reionization. My numerical and analytic models suggest that, after properly taking into account the inhomogeneous density field of the IGM, such emission is probably too faint to observe with current and near-future instruments.

Calibration of physically-motivated semi-analytic models of the coupled fluctuations in the ionizing background and mean free path will allow future cosmological simulations to include a self-consistent inhomogeneous ionizing radiation field across cosmic time. A fluctuating ionizing background naturally leads to fluctuations in the ionization heating rate due to the frequency-dependence of the mean free path. Because attenuation is strongest at the ionization frequency, regions with a weaker overall background will typically experience a harder ionizing spectrum that results in a higher heating rate per atom, and these fluctuations may have observable consequences in the Lyα forest (e.g. Greig et al. 2015) and influence the formation of dwarf galaxies at early times (e.g. Oñorbe et al. 2015).

The mean free path also plays a key role in models of reionization by suppressing the formation of large ionized regions (e.g. Furlanetto & Oh 2005), but its implementation to

date has been very crude (although see Sobacchi & Mesinger 2014). The "shielding" of void regions by neutral absorbers due to the locally weak ionizing background may extend the final stages of the reionization process that were originally thought to occur extremely rapidly. Such effects are missed in state-of-the-art radiative transfer models of reionization because they either lack the required volume to have large enough voids (i.e. several mean free paths on a side; Pawlik et al. 2015; Chardin et al. 2015) or the required resolution to resolve dense neutral gas inside of ionized regions (Iliev et al., 2014). My ionizing background models are currently unable to describe the progress of reionization, but a hybrid approach built on top of semi-analytic reionization models (e.g. Mesinger & Furlanetto 2007; Dixon et al. 2014) should be possible in the near future.

Bibliography

Abel, T., & Haehnelt, M. G. 1999, ApJ, 520, L13

Aguirre, A., Schaye, J., Kim, T.-S., et al. 2004, ApJ, 602, 38

Altay, G., Croft, R. A. C., & Pelupessy, I. 2008, MNRAS, 386, 1931

Alvarez, M. A., & Abel, T. 2007, MNRAS, 380, L30

Baltz, E. A., Gnedin, N. Y., & Silk, J. 1998, ApJ, 493, L1

Becker, G. D., & Bolton, J. S. 2013, MNRAS, 436, 1023

Becker, G. D., Bolton, J. S., Madau, P., et al. 2015, MNRAS, 447, 3402

Becker, G. D., Hewett, P. C., Worseck, G., & Prochaska, J. X. 2013, MNRAS, 430, 2067

Bolton, J., Meiksin, A., & White, M. 2004, MNRAS, 348, L43

Bolton, J. S., & Becker, G. D. 2009, MNRAS, 398, L26

Bolton, J. S., & Haehnelt, M. G. 2007a, MNRAS, 374, 493

—. 2007b, MNRAS, 382, 325

Bolton, J. S., & Haehnelt, M. G. 2013, MNRAS, 429, 1695

Bolton, J. S., Haehnelt, M. G., Viel, M., & Carswell, R. F. 2006, MNRAS, 366, 1378

Bolton, J. S., Haehnelt, M. G., Viel, M., & Springel, V. 2005, MNRAS, 357, 1178

Bolton, J. S., Oh, S. P., & Furlanetto, S. R. 2009, MNRAS, 395, 736

Bolton, J. S., & Viel, M. 2011, MNRAS, 414, 241

Bosman, S. E. I., & Becker, G. D. 2015, ArXiv e-prints, arXiv:1505.06880

Bouwens, R. J., Illingworth, G. D., Oesch, P. A., et al. 2015a, ArXiv e-prints, arXiv:1503.08228

—. 2015b, ApJ, 803, 34

Brown, T. M., Tumlinson, J., Geha, M., et al. 2014, ApJ, 796, 91

Calverley, A. P., Becker, G. D., Haehnelt, M. G., & Bolton, J. S. 2011, MNRAS, 412, 2543

Cantalupo, S., Lilly, S. J., & Haehnelt, M. G. 2012, MNRAS, 425, 1992

Cantalupo, S., & Porciani, C. 2011, MNRAS, 411, 1678

Cantalupo, S., Porciani, C., & Lilly, S. J. 2008, ApJ, 672, 48

Cen, R. 1992, ApJS, 78, 341

Chardin, J., Haehnelt, M. G., Aubert, D., & Puchwein, E. 2015, ArXiv e-prints, arXiv:1505.01853

Choudhury, T. R., Puchwein, E., Haehnelt, M. G., & Bolton, J. S. 2014, ArXiv e-prints, arXiv:1412.4790

Compostella, M., Cantalupo, S., & Porciani, C. 2013, MNRAS, 435, 3169

—. 2014, MNRAS, 445, 4186

Cowie, L. L., Barger, A. J., & Trouille, L. 2009, ApJ, 692, 1476

Croft, R. A. C. 2004, ApJ, 610, 642

Croft, R. A. C., Weinberg, D. H., Katz, N., & Hernquist, L. 1997, ApJ, 488, 532

Dall'Aglio, A., Wisotzki, L., & Worseck, G. 2008, A&A, 491, 465

Davé, R., Hernquist, L., Katz, N., & Weinberg, D. H. 1999, ApJ, 511, 521

Davidsen, A. F., Kriss, G. A., & Zheng, W. 1996, Nature, 380, 47

Davies, F. B., & Furlanetto, S. R. 2014, MNRAS, 437, 1141

Desjacques, V., Dizgah, A. M., & Biagetti, M. 2014, MNRAS, 444, 2793

Dijkstra, M., Mesinger, A., & Wyithe, J. S. B. 2011, MNRAS, 414, 2139

Dixon, K. L., & Furlanetto, S. R. 2009, ApJ, 706, 970

Dixon, K. L., Furlanetto, S. R., & Mesinger, A. 2014, MNRAS, 440, 987

Dunkley, J., Komatsu, E., Nolta, M. R., et al. 2009, ApJS, 180, 306

Efstathiou, G., Davis, M., White, S. D. M., & Frenk, C. S. 1985, ApJS, 57, 241

Ellis, R. S., McLure, R. J., Dunlop, J. S., et al. 2013, ApJ, 763, L7

Fan, X., Narayanan, V. K., Strauss, M. A., et al. 2002, AJ, 123, 1247

Fan, X., Narayanan, V. K., Lupton, R. H., et al. 2001, AJ, 122, 2833

Fan, X., Hennawi, J. F., Richards, G. T., et al. 2004, AJ, 128, 515

Fan, X., Strauss, M. A., Becker, R. H., et al. 2006, AJ, 132, 117

Fanidakis, N., Macciò, A. V., Baugh, C. M., Lacey, C. G., & Frenk, C. S. 2013, MNRAS, 436, 315

Fardal, M. A., Giroux, M. L., & Shull, J. M. 1998, AJ, 115, 2206

Faucher-Giguère, C.-A., Lidz, A., Hernquist, L., & Zaldarriaga, M. 2008a, ApJ, 682, L9

Faucher-Giguère, C.-A., Lidz, A., Zaldarriaga, M., & Hernquist, L. 2009, ApJ, 703, 1416

Faucher-Giguère, C.-A., Prochaska, J. X., Lidz, A., Hernquist, L., & Zaldarriaga, M. 2008b, ApJ, 681, 831

Fechner, C., Reimers, D., Kriss, G. A., et al. 2006, A&A, 455, 91

Fialkov, A., Barkana, R., & Visbal, E. 2014, Nature, 506, 197

Friedrich, M. M., Mellema, G., Iliev, I. T., & Shapiro, P. R. 2012, MNRAS, 421, 2232

Furlanetto, S. R. 2006, MNRAS, 371, 867

Furlanetto, S. R. 2009, ApJ, 703, 702

Furlanetto, S. R., & Dixon, K. L. 2010, ApJ, 714, 355

Furlanetto, S. R., & Johnson Stoever, S. 2010, MNRAS, 404, 1869

Furlanetto, S. R., & Lidz, A. 2011, ApJ, 735, 117

Furlanetto, S. R., & Mesinger, A. 2009, MNRAS, 394, 1667

Furlanetto, S. R., & Oh, S. P. 2005, MNRAS, 363, 1031

—. 2008a, ApJ, 681, 1

—. 2008b, ApJ, 681, 1

Furlanetto, S. R., & Oh, S. P. 2008, ApJ, 681, 1

Furlanetto, S. R., Oh, S. P., & Briggs, F. H. 2006, Physics Reports, 433, 181

Furlanetto, S. R., Zaldarriaga, M., & Hernquist, L. 2004, ApJ, 613, 1

Giavalisco, M., Sahu, K., & Bohlin, R. C. 2002, New Estimates of the Sky Background for the HST Exposure Time Calculator, Tech. rep.

Giovanardi, C., Natta, A., & Palla, F. 1987, Astronomy and Astrophysics Supplement Series (ISSN 0365-0138), 70, 269

Giovanardi, C., & Palla, F. 1989, Astronomy and Astrophysics Supplement Series (ISSN 0365-0138), 77, 157

Gontcho, S. G. A., Miralda-Escudé, J., & Busca, N. G. 2014, ArXiv e-prints, arXiv:1404.7425

Gould, A., & Weinberg, D. H. 1996, Astrophysical Journal v.468, 468, 462

Greig, B., Bolton, J. S., & Wyithe, J. S. B. 2015, MNRAS, 447, 2503

Gunn, J. E., & Peterson, B. A. 1965, ApJ, 142, 1633

Haardt, F., & Madau, P. 1996, ApJ, 461, 20

—. 2012, ApJ, 746, 125

Heap, S. R., Williger, G. M., Smette, A., et al. 2000, ApJ, 534, 69

Hinshaw, G., Larson, D., Komatsu, E., et al. 2013, The Astrophysical Journal Supplement, 208, 19

Hopkins, P. F., & Hernquist, L. 2009, ApJ, 698, 1550

Hopkins, P. F., Richards, G. T., & Hernquist, L. 2007, ApJ, 654, 731

Hui, L., & Gnedin, N. Y. 1997, MNRAS, 292, 27

Hui, L., & Haiman, Z. 2003, ApJ, 596, 9

Hui, L., & Rutledge, R. E. 1999, ApJ, 517, 541

Iliev, I. T., Mellema, G., Ahn, K., et al. 2014, MNRAS, 439, 725

Kim, T.-S., Carswell, R. F., Cristiani, S., D'Odorico, S., & Giallongo, E. 2002a, MNRAS, 335, 555

Kim, T.-S., Cristiani, S., & D'Odorico, S. 2001, A&A, 373, 757

—. 2002b, A&A, 383, 747

Kim, T.-S., Partl, A. M., Carswell, R. F., & Müller, V. 2013, A&A, 552, A77

Kriss, G. A., Shull, J. M., Oegerle, W., et al. 2001, Science, 293, 1112

Lidz, A., McQuinn, M., Zaldarriaga, M., Hernquist, L., & Dutta, S. 2007, ApJ, 670, 39

Loeb, A., & Furlanetto, S. R. 2013, The First Galaxies in the Universe (Princeton, NJ: Princeton University Press)

Loeb, A., & Rybicki, G. B. 1999, ApJ, 524, 527

Lusso, E., Worseck, G., Hennawi, J. F., et al. 2015, MNRAS, 449, 4204

Madau, P., Haardt, F., & Rees, M. J. 1999, ApJ, 514, 648

Martin, C., Moore, A., Morrissey, P., et al. 2010, in Society of Photo-Optical Instrumentation Engineers (SPIE) Conference Series, Vol. 7735, Society of Photo-Optical Instrumentation Engineers (SPIE) Conference Series

McDonald, P., & Miralda-Escudé, J. 2001, ApJ, 549, L11

McDonald, P., Seljak, U., Cen, R., Bode, P., & Ostriker, J. P. 2005, MNRAS, 360, 1471

McGreer, I. D., Mesinger, A., & D'Odorico, V. 2015, MNRAS, 447, 499

McGreer, I. D., Mesinger, A., & Fan, X. 2011, MNRAS, 415, 3237

McGreer, I. D., Jiang, L., Fan, X., et al. 2013, ApJ, 768, 105

McQuinn, M., Hernquist, L., Zaldarriaga, M., & Dutta, S. 2007a, MNRAS, 381, 75

—. 2007b, MNRAS, 381, 75

McQuinn, M., Lidz, A., Zaldarriaga, M., et al. 2009, ApJ, 694, 842

McQuinn, M., Oh, S. P., & Faucher-Giguère, C.-A. 2011, ApJ, 743, 82

McQuinn, M., & Worseck, G. 2014, MNRAS, 440, 2406

Meiksin, A. 2009, Rev. Mod. Phys., 81, 1405

Meiksin, A., & White, M. 2003, MNRAS, 342, 1205

—. 2004, MNRAS, 350, 1107

Mesinger, A. 2010, MNRAS, 407, 1328

Mesinger, A., Aykutalp, A., Vanzella, E., et al. 2015, MNRAS, 446, 566

Mesinger, A., & Furlanetto, S. 2007, ApJ, 669, 663

Mesinger, A., & Furlanetto, S. 2009, MNRAS, 400, 1461

Mesinger, A., & Furlanetto, S. R. 2008a, MNRAS, 385, 1348

—. 2008b, MNRAS, 386, 1990

Mesinger, A., & Haiman, Z. 2007, ApJ, 660, 923

Mesinger, A., McQuinn, M., & Spergel, D. N. 2012, MNRAS, 422, 1403

Miralda-Escude, J. 1993, MNRAS, 262, 273

Miralda-Escudé, J. 1998a, ApJ, 501, 15

—. 1998b, ApJ, 501, 15

Miralda-Escudé, J., Cen, R., Ostriker, J. P., & Rauch, M. 1996, ApJ, 471, 582

Miralda-Escudé, J., Haehnelt, M., & Rees, M. J. 2000, ApJ, 530, 1

Miralda-Escudé, J., Haehnelt, M., & Rees, M. J. 2000, ApJ, 530, 1

Miralda-Escudé, J., & Rees, M. J. 1994, MNRAS, 266, 343

Mirocha, J., Skory, S., Burns, J. O., & Wise, J. H. 2012, ApJ, 756, 94

Monaghan, J. J. 1992, ARAA, 30, 543

Mortlock, D. J., Warren, S. J., Venemans, B. P., et al. 2011, Nature, 474, 616

Muñoz, J. A., Oh, S. P., Davies, F. B., & Furlanetto, S. R. 2014, ArXiv e-prints, arXiv:1410.2249

Muzahid, S., Srianand, R., & Petitjean, P. 2011, MNRAS, 410, 2193

Oñorbe, J., Boylan-Kolchin, M., Bullock, J. S., et al. 2015, ArXiv e-prints, arXiv:1502.02036

Oesch, P. A., Bouwens, R. J., Illingworth, G. D., et al. 2013, ApJ, 773, 75

O'Meara, J. M., Prochaska, J. X., Burles, S., et al. 2007, ApJ, 656, 666

O'Meara, J. M., Prochaska, J. X., Worseck, G., Chen, H.-W., & Madau, P. 2013, ApJ, 765, 137

Ono, Y., Ouchi, M., Mobasher, B., et al. 2012, ApJ, 744, 83

Ono, Y., Ouchi, M., Mobasher, B., et al. 2012, ApJ, 744, 83

Paresce, F., McKee, C. F., & Bowyer, S. 1980, ApJ, 240, 387

Parsons, A. R., Liu, A., Aguirre, J. E., et al. 2014, ApJ, 788, 106

Paschos, P., Norman, M. L., Bordner, J. O., & Harkness, R. 2007, ArXiv e-prints, arXiv:0711.1904

Pawlik, A. H., Schaye, J., & Dalla Vecchia, C. 2015, ArXiv e-prints, arXiv:1501.01980

Pentericci, L., Fontana, A., Vanzella, E., et al. 2011, ApJ, 743, 132

Pentericci, L., Vanzella, E., Fontana, A., et al. 2014, ApJ, 793, 113

Pontzen, A. 2014, PRD, 89, 083010

Pontzen, A., Bird, S., Peiris, H., & Verde, L. 2014, ApJ, 792, L34

Pritchard, J. R., & Furlanetto, S. R. 2006, MNRAS, 367, 1057

Pritchard, J. R., & Loeb, A. 2010, PRD, 82, 023006

Prochaska, J. X., Madau, P., O'meara, J. M., & Fumagalli, M. 2014, MNRAS, 438, 476

Prochaska, J. X., O'meara, J. M., & Worseck, G. 2010, ApJ, 718, 392

Prochaska, J. X., Worseck, G., & O'meara, J. M. 2009, ApJL, 705, L113

Puchwein, E., Bolton, J. S., Haehnelt, M. G., et al. 2015, MNRAS, 450, 4081

Rahmati, A., Pawlik, A. H., Raičevič, M., & Schaye, J. 2013, MNRAS, 430, 2427

Rao, S. M., Turnshek, D. A., & Nestor, D. B. 2006, ApJ, 636, 610

Rauch, M. 1998, ARAA, 36, 267

Rauch, M., Miralda-Escude, J., Sargent, W. L. W., et al. 1997, ApJ, 489, 7

Reimers, D., Kohler, S., Wisotzki, L., et al. 1997, A&A, 327, 890

Robertson, B. E., Ellis, R. S., Furlanetto, S. R., & Dunlop, J. S. 2015, ApJ, 802, L19

Robertson, B. E., Furlanetto, S. R., Schneider, E., et al. 2013, ApJ, 768, 71

Rudie, G. C., Steidel, C. C., Shapley, A. E., & Pettini, M. 2013, ApJ, 769, 146

Rudie, G. C., Steidel, C. C., Trainor, R. F., et al. 2012, ApJ, 750, 67

Schaye, J. 2001, ApJ, 559, 507

Schenker, M. A., Ellis, R. S., Konidaris, N. P., & Stark, D. P. 2014, ApJ, 795, 20

Schroeder, J., Mesinger, A., & Haiman, Z. 2013, MNRAS, 428, 3058

Scott, J., Bechtold, J., Dobrzycki, A., & Kulkarni, V. P. 2000, ApJS, 130, 67

Scott, J. E., Kriss, G. A., Brotherton, M., et al. 2004, ApJ, 615, 135

Shapiro, P. R., Iliev, I. T., Alvarez, M. A., & Scannapieco, E. 2006, ApJ, 648, 922

Sheth, R. K., & Tormen, G. 1999, MNRAS, 308, 119

Shull, J. M., France, K., Danforth, C. W., Smith, B., & Tumlinson, J. 2010, ApJ, 722, 1312

Shull, J. M., Stevans, M., & Danforth, C. W. 2012, ApJ, 752, 162

Shull, J. M., Tumlinson, J., Giroux, M. L., Kriss, G. A., & Reimers, D. 2004, ApJ, 600, 570

Shull, J. M., & van Steenberg, M. E. 1985, ApJ, 298, 268

Sobacchi, E., & Mesinger, A. 2014, MNRAS, 440, 1662

Sokasian, A., Abel, T., & Hernquist, L. 2002, MNRAS, 332, 601

—. 2003, MNRAS, 340, 473

Songaila, A. 1998, AJ, 115, 2184

—. 2005, AJ, 130, 1996

Songaila, A., & Cowie, L. L. 2010, ApJ, 721, 1448

Springel, V. 2005a, MNRAS, 364, 1105

—. 2005b, MNRAS, 364, 1105

Springel, V., & Hernquist, L. 2003, MNRAS, 339, 312

Stark, D. P., Ellis, R. S., Chiu, K., Ouchi, M., & Bunker, A. 2010, MNRAS, 408, 1628

Stark, D. P., Ellis, R. S., Chiu, K., Ouchi, M., & Bunker, A. 2010, MNRAS, 408, 1628

Sullivan, P. W., & Simcoe, R. A. 2012, PASP, 124, 1336

Syphers, D., Anderson, S. F., Zheng, W., et al. 2011, ApJ, 726, 111

—. 2012, AJ, 143, 100

Syphers, D., & Shull, J. M. 2013, ApJ, 765, 119

Syphers, D., & Shull, J. M. 2013, ApJ, 765, 119

—. 2014, ApJ, 784, 42

Telfer, R. C., Zheng, W., Kriss, G. A., & Davidsen, A. F. 2002, ApJ, 565, 773

Tepper-García, T. 2006, MNRAS, 369, 2025

Theuns, T., Leonard, A., Efstathiou, G., Pearce, F. R., & Thomas, P. A. 1998, MNRAS, 301, 478

Theuns, T., Schaye, J., Zaroubi, S., et al. 2002, ApJ, 567, L103

Tilvi, V., Papovich, C., Finkelstein, S. L., et al. 2014, ApJ, 794, 5

Tittley, E. R., & Meiksin, A. 2007, MNRAS, 380, 1369

Trainor, R., & Steidel, C. C. 2013, ApJL, 775, L3

Treu, T., Trenti, M., Stiavelli, M., Auger, M. W., & Bradley, L. D. 2012, ApJ, 747, 27

Tytler, D. 1987, ApJ, 321, 49

Vanden Berk, D. E., Richards, G. T., Bauer, A., et al. 2001, AJ, 122, 549

Venkatesan, A., & Benson, A. 2011, MNRAS, 417, 2264

Verner, D. A., Ferland, G. J., Korista, K. T., & Yakovlev, D. G. 1996, ApJ, 465, 487

Vogelsberger, M., Genel, S., Springel, V., et al. 2014, MNRAS, 444, 1518

Walter, F., Carilli, C., Bertoldi, F., et al. 2004, ApJ, 615, L17

Weinberg, D. H., Hernsquit, L., Katz, N., Croft, R., & Miralda-Escudé, J. 1997, in Structure and Evolution of the Intergalactic Medium from QSO Absorption Line System, ed. P. Petitjean & S. Charlot, 133

White, R. L., Becker, R. H., Fan, X., & Strauss, M. A. 2003, AJ, 126, 1

Willott, C. J., Percival, W. J., McLure, R. J., et al. 2005, ApJ, 626, 657

Wise, J. H., Demchenko, V. G., Halicek, M. T., et al. 2014, MNRAS, 442, 2560

Worseck, G., Fechner, C., Wisotzki, L., & Dall'Aglio, A. 2007, A&A, 473, 805

Worseck, G., & Prochaska, J. X. 2011, ApJ, 728, 23

Worseck, G., Prochaska, J. X., Hennawi, J. F., & McQuinn, M. 2014a, arXiv, 7405

Worseck, G., & Wisotzki, L. 2006, A&A, 450, 495

Worseck, G., Prochaska, J. X., McQuinn, M., et al. 2011, ApJL, 733, L24

Worseck, G., Prochaska, J. X., O'meara, J. M., et al. 2014b, MNRAS, 445, 1745

—. 2014c, MNRAS, 445, 1745

Wyithe, J. S. B., & Bolton, J. S. 2011, MNRAS, 412, 1926

Wyithe, J. S. B., & Loeb, A. 2003, ApJ, 586, 693

Yu, Q. 2005, ApJ, 623, 683

Zahn, O., Reichardt, C. L., Shaw, L., et al. 2012, ApJ, 756, 65

Zel'dovich, Y. B. 1970, A&A, 5, 84

Zheng, W., Kriss, G. A., Deharveng, J.-M., et al. 2004, ApJ, 605, 631

Zuo, L. 1992, MNRAS, 258, 36

Zuo, L. 1993, A&A, 278, 343